ADDITIVE MANUFACTURING OF MARAGING 250 STEELS FOR THE REJUVENATION AND REPURPOSING OF DIE CASTING TOOLING

by

MICHAEL ANDREW KOTTMAN

Submitted in partial fulfillment of the requirements
for the degree of Master of Science

Thesis Advisor: Prof. David Schwam

Department of Materials Science and Engineering
CASE WESTERN RESERVE UNIVERSITY

January, 2015

CASE WESTERN RESERVE UNIVERSITY

SCHOOL OF GRADUATE STUDIES

We hereby approve the thesis of

Michael Andrew Kottman

Candidate for the degree of Master of Science*.

Dr. David Schwam
Committee Chair, Advisor

Dr. John J. Lewandowski
Committee Member

Dr. Gerhard Welsch
Committee Member

Date of Defense
November 7, 2014

*We also certify that written approval has been obtained
for any proprietary material contained therein.

Dedicated to my wife and parents
for their steadfast love and support.

Table of Contents

List of Figures

List of Tables

Acknowledgements

This research was supported by America Makes, the National Additive Manufacturing Innovation Insititute, under the project "Qualification of Additive Manufacturing Processes and Procedures for Repurposing and Rejuvenation of Tooling." Additional thanks are extended to Dr. Xuejun Zhu, Dr. Bishal Silwal, and Mr. Richard Tomazin for sharing their assistance and knowledge throughout this project, as well as the many industrial partners who graciously accommodated our research, giving us access to their facilities and sharing their expertise.

Lastly, many thanks are due to Dr. David Schwam for his support, advice, and expertise which made this project possible.

Additive Manufacturing of Maraging 250 Steels for the Rejuvenation and Repurposing of Die Casting Tooling

by

MICHAEL KOTTMAN

Abstract

In this study, a number of established additive manufacturing processes were evaluated for their suitability repairing high-pressure die cast tooling. The processes included in this study are laser hot wire (LHW), electron beam freeform fabrication (EBF3), gas metal arc welding (GMAW), Laser Engineered Net Shaping (LENS®), and direct metal deposition (DMD). To determine each process' suitability, blocks of maraging 250 steel were deposited on H-13 base metal. The results show that the maraging deposits are capable of providing good strength (>160 ksi), toughness (>15 ft-lbs), and hardness (45 HRC) for die tooling applications, but care must be taken to limit the occurrence of defects, particularly porosity. Of the processes tested, the LHW, DMD, and LENS® processes had the best balance of deposit properties. However, additional work will be required to optimize the processing parameters for each process.

Chapter 1: Introduction

1.1. Die casting and die casting dies

High pressure die casting is a secondary manufacturing process in which molten metal is formed into a desired shape by allowing it to flow into a mold under externally applied pressure. The resulting part is usually near net-shape, requiring only minor finishing. Some castings can be made net shape, with no additional finishing required. Castings can have very complex geometries and include both external and internal features. Die casting is most useful for high-volume production of complex parts, which would be more difficult and expensive to produce via machining or other forming methods.

Die casting is capable of producing parts from a number of alloy systems. Aluminum and zinc alloys are the most common, though casting of magnesium, zinc-aluminum (ZA) alloys, copper and tin are also industrially significant. Casting does have drawbacks, such as susceptibility to porosity, deterioration of surface finish and dimensional accuracy over time, and safety hazards to humans when processing hot metals and environmental problems (Groover, 2010). Castings may also have lower mechanical properties than machined or forged products depending on the cooling rates, chemical segregation, die design, etc. since there is no work hardening involved in the process and the grain growth

will tend to be equiaxial, initiating on the surface of the die and growing inward (Groover, 2010).

Dies used in die casting are commonly manufactured out of hot tool steels such as H13 and H11. Improved version of these hot tool steels have been produced in recent years and are making inroads into the die casting industry (NADCA, 2012)(Zhu, 2004).

1.2. Modes of failure of die cast tooling

Die failure is mostly caused by thermal cracks, washout, and soldering on its surfaces when contacted with the liquid molten metals (Chen, 1999)(Gopal, 2000).

The occurrence of thermal cracking in die cast tooling is attributed to non-uniform thermal fatigue which leads to surface stresses that cause cracking in materials of sufficiently low material strength or which contain surface defects (Mellouli, 2014). As the die is subjected to repeated injection of molten metal and subsequent cooling, the dies tooling is undergoing thermal cycling. These thermal stresses are non-uniform in the die, dependent on the die geometry (die thickness, proximity to coolant channels, etc.) and material; eventually, these stresses can become sufficiently high to initiate cracks in the die, leading to failure (Zhu, 2004).

Washout in die casting tooling is attributed to the interaction of the flowing, injected molten metal with the surface of the die (Zhu, 2004), especially in high-pressure die casting. The injected metal causes erosion and/or dissolution of the surface of the die as

it passes across the die cavity, removing material and changing internal surface finish and dimension of the tooling.

Soldering is the adhesion of the casting to the die or core, causing a buildup of casting alloy on the surface (Zhu, 2004). Soldering can cause problems when casting is ejected because it will make separation from the die more difficult, and can also cause abrasions on the cast part once separated. Soldering takes place during solidification as a result of chemical and mechanical reactions at the interface between the casting liquid and the die tooling (Gulizia, 2001)(Zhu, 2004).

1.3. Tool steels

The three most common materials for manufacturing die casting tooling are AISI grade H13, H11, or H21 steels (Zhu, 2004), which are a class of hot-working tool steels developed for strength and hardness that contain medium-carbon content along with strong carbide formers such as chromium, vanadium, and tungsten (Roberts, 1998). The microstructure of tooling made with these grades of steel is tempered martensite with dispersed carbides to promote high-temperature strength and hot hardness (Roberts, 1998).

AISI Grade	C	Cr	V	W	Mo
H11	0.35	5.00	0.40	-	1.50
H13	0.35	5.00	1.00	-	1.50
H21	0.35	3.50	-	9.00	-

Table 1. Nominal alloying elements (in weight percent) of common AISI hot work tool steels used for high-pressure dies (adapted from Roberts, 1998).

Maraging steels were introduced in the early 1960s, and quickly gained interest as an alternative to medium- and high-carbon tool steels because they don't rely on carbon as a strengthener which reduces the occurrence of quench cracking while the high nickel content provides corrosion resistance (Stanford, 2008). Maraging steels have found lasting applications in nuclear and aerospace parts, casting dies, drill chucks, and punching, injection, and extrusion dies (Hall, 1968) due to their good toughness, high strength, and ease of fabrication (Decker, 1962).

Maraging steels are a family of low carbon iron-nickel alloys with additional, lower levels of hardening alloys such as Cr, Co, Mo, Ti, and Al (Sadowski, 1965). The amount of alloying in four common maraging alloys for welding (grades 200, 250, 300, 350) can be found in Table 2 (Lang, 1971).

Maraging Steel Grade	Ni	Co	Mo	Ti
200	18.0	8.5	3.2	0.2
250	18.0	8.0	4.8	0.4
300	18.5	8.7	5.0	0.6
350	18.0	11.8	4.6	1.3

Table 2. Nominal alloy composition of four common maraging steels (adapted from Lang, 1971).

These alloys are martensitic and undergo precipitation strengthening during aging. Initially, the martensite is relatively soft (roughly HRC 30) initially, but hardens after aging around ºC (900ºF) due to precipitation hardening. These alloys have also shown to more than double in strength after aging (Floreen, 1962).

Eighteen percent nickel maraging steels have an austenizing temperature of approximately 732° C (1350° F). The steel takes on a low-carbon BCC martensitic microstructure upon cooling, around 154°C (310°F) by a diffusionless shear process. Unlike other iron-based alloys, maraging steels will undergo the martensitic transformation regardless of cooling rate (Lang, 1971). After aging, the 18% nickel maraging steels are strengthened through precipitation of intermetallics such as Ni_3Mo and Ni_3Ti (Baker, 1964). The microstructure of the aged maraging welds consist of pools of austenite in a martensitic matrix. The austenite pools form in regions of lowered reversion temperatures due to segregation of alloying elements (Lang, 1971).

The superior mechanical properties of maraging steel have attracted the attention of tool makers for aluminum die casting tooling. Gehrike (1993) attributes the superior performance of maraging steels in demanding die casting applications to the high toughness at higher strength, low dimensional changes during heat treatment, and resistance to heat checking and thermal shock. The premium cost over tool steels with less nickel has prevented maraging steels from taking over a larger segment of the tool and mold making alloys. However, when applied as a cladded layer, the required volume of maraging steel is much lower, making the higher cost easier to justify in view of the improved performance.

Chapter 2: Processes

2.1. Gas Metal Arc Welding (GMAW)

The gas metal arc welding (GMAW) process when used for additive manufacturing is sometimes called rapid pulsed arc (RPA) or, more generically, wire and arc additive manufacturing (WAAM). For consistency, this paper will refer to the process as GMAW. In GMAW, an electric arc is established between a continuously-fed consumable wire electrode and the work-piece. The process requires the use of a shielding gas which can be either inert or active (Nadzam, 1995).

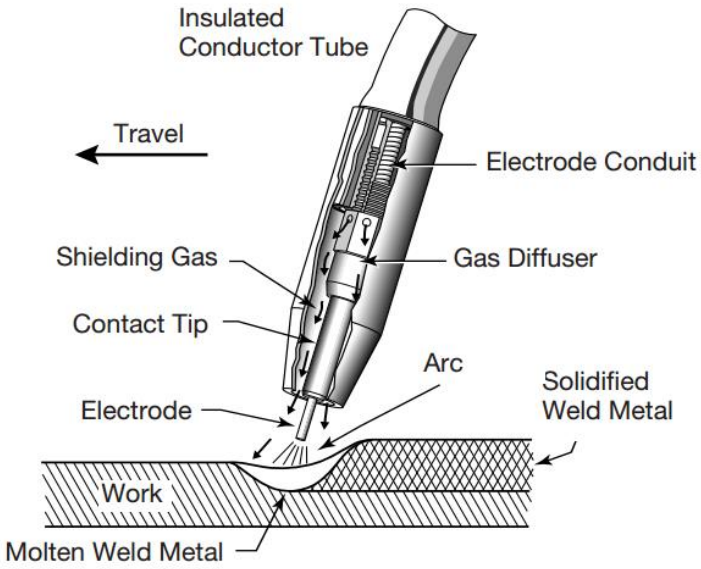

Figure 1. Schematic of the GMAW process (courtesy Company A).

GMAW is a well-developed and widely adopted joining technology with numerous advantages. It is capable of welding most metallic materials, and can deposit metal in all positions. The process is economical because it has high deposition rates and travel

speeds, as well as less maintenance downtime due to the use of wires electrodes which can be purchased in continuous rods in weights between 5 and 500 pounds. The GMAW process is well suited for automated/robotic deposition since the wire provides consistent consumable feeding (Nadzam, 1995).

Free-form additive manufacturing of parts using GMAW is not a widely adopted commercially, but it has been used for resurfacing and repair of parts for a number of years (Sutter, 1993). There have been studies on additive manufacturing using GMAW for carbon steel (Cao, 2011) and Ti-6Al-4V (Sequeira, 2010) and it has been the subject of modelling efforts for additive manufacturing (Ding, 2015)(Cao, 2011).

GMAW deposits can have a number of defects, including porosity, lack of fusion or incomplete penetration, excessive melt-through, undercutting, or cracking and can deteriorate in quality from insufficient shielding gas, irregular wire feeding, burn-back and unstable arc (Nadzam, 1995).

2.1.1. GMAW Equipment

The equipment required for GMAW additive manufacturing is the same as automatic GMAW welding systems: a power source, electrode/wire feeder, shielding gas regulator, and welding torch, and robotic control system (Nadzam, 1995).

In the last thirty years, GMAW power sources have largely moved to constant-voltage, inverter-based systems from the more conventional transformer-rectifier systems. The inverter technology provides the option of more advanced waveforms, such as pulsed current with variable pulse shapes (i.e. square or sine) and frequencies

(Nadzam, 1995), which are often used when applying the GMAW process to additive manufacturing to better control the deposition process (Sequeira, 2010).

The wire feeder (or electrode feeder) is attached near the electrode spool or bulk package (i.e. drum or box) and pulls it from the package into a conduit that feeds out to the welding torch. Typically, the wire feeder has two pairs of rolls with pressure-adjusting screws to straighten the electrode as it comes out of the package. The rolls are driven by a direct-current motor and gear box; this is how the wire feed speed is controlled. The rolls may either be smooth or knurled, depending on the electrode hardness. If the conduit is long or the material is too soft, a push-pull torch may be used which not only uses the wire feeder to push the wire through the conduit, but also uses an additional unit at the torch which pulls the wire (Nadzam, 1995).

Generally, the wire feed unit also controls the shielding gas and, through synergic control with the power source, also controls current. Modern, synergic wire feeder/power source systems allow independent programming of gas pre-flow and post-flow, and specific start and stop procedures (i.e. burn-back, crater filling) (Nadzam, 1995).

The main parts of the torch are the contact tip where current is transmitted to the electrode and the nozzle controls the flow of the shielding gas. Robotic torches use emergency-stop systems to prevent damage to the arm and torch in the event of a collision, and also tend to have an automatic torch cleaning system that uses pressurized air to blow spatter out of the nozzle and a reamer that cleans the contact tip and nozzle (Nadzam, 1995).

2.1.2. GMAW Parameters

2.1.2.1. Current and Voltage

The most common waveform for GMAW welding is DCEP (DC+), in which the electrode is connected to positive terminal and the work piece is grounded to the negative terminal. An increase in the voltage will tend to increase the arc length as well as widen and flatten the deposit, but these effects will change with shielding gas, contact-tip-to-work distance, and welding position (Nadzam, 1995).

The transfer mechanism for droplets through the arc is voltage and current dependent. At low power, the electrode undergoes short-circuit transfer where the metal transfers by bridging from the electrode to the work piece (creating a short) usually over 100 Hz. Short-circuit transfer is a low heat input process that is typically used on thin materials and out of position welding, and can provide less base metal dilution than other transfer modes (Norrish, 2014).

At higher voltage and current the arc moves into the globular transfer regime. In addition to current and voltage, the transition point into globular is also dependent on the shielding gas and electrode. The transfer of metal is no longer from shorts; instead droplets form on the end of the electrode that are the diameter of the electrode or larger and which pass through the arc at a lower frequency than short-circuit transfer. This transfer method works best in flat or horizontal positions because gravity plays a large role in the transfer of the drop through the arc (Nadzam, 1995).

At even higher current and voltage the process transitions into the spray transfer mode. This transition current into spray transfer depends on the shielding gas (argon-rich blends), electrode type and electrode size. Since the current and voltage is high to enter this transfer mode, the heat input is also higher. Unlike the large droplets in globular transfer, spray transfer projects many smaller droplets at high frequencies (up to 350 Hz). Most applications for spray transfer are in flat or horizontal positions due to the influence of gravity on the droplet transfer (Nadzam, 1995).

Using advanced waveforms that are possible due to inverter-based power sources, it is possible to have transfer modes that do not meet any of the above classifications as well. For instance, pulsed waveforms can enable lower heat input spray-transfer that improves out-of-position deposition, decreases dilution, and creates finer bead dimensions (Nadzam, 1995) (Ghosh, 2009). Such waveforms are of great interest for additive manufacturing applications since they can provide more precise heat input and metal transfer.

2.1.2.2. Shielding Gas

For GMAW, the choice of shielding gas has a large influence on the deposition mode, stability and rate as well as bead shape and penetration. Both inert (argon, helium) and active (carbon dioxide, oxygen) gasses are used, as well as blends of two or more gasses. For carbon steel applications, it is common to use 80-95% argon/balance CO_2 while stainless and higher-alloy metals may use 95-98% argon/balance O_2. The active gas

addition in these blends modifies the bead shape and stabilizes the arc. Certain non-ferrous metals may use argon/helium blends as well (Nadzam, 1995).

2.1.2.3. Travel speed

The linear rate at which the electrode travels across the work piece will be inversely dependent to both the heat input per unit length and the deposition rate per unit length. Penetration has a non-linear correlation to travel speed, where it increases initially with increasing travel speed, but at even higher travel speeds the deposition rate becomes too low to fill the cavity being produced by the arc and the deposit will experience undercut. For additive manufacturing applications, finer dimensional control can be obtained with smaller linear deposition rates so appropriately high travel speeds paired with fine electrode diameters are commonly used for additive manufacturing with the GMAW process (Nadzam, 1995).

2.2. Laser Hot Wire (LHW)

Since as early as 1981, hybrid laser-arc welding (HLAW) has been investigated (Steen, 1981). While primarily focused on gas metal arc welding (GMAW), gas tungsten arc welding (GTAW) and plasma combinations have also been investigated periodically (Diebold, 1984) (Walduck, 1995). Early work showed that the incorporation of an arc source had the benefit of increasing deposition rates, improved fit up, ability to modify the deposit composition, and overcoming the power limitation of pure laser welding. However, despite its early development, laser hybrid processing was not readily accepted

for many years due to limitations of early technology, such as poor beam focus control and the space requirements for early laser systems. The first large commercial application was in 2000 when the Meyer Werft Shipbuilding company opened a new panel line for welding deck and bulkhead panels with stiffeners using HLAW with CO_2 lasers. This major adoption of the technology led organizations such as DNV and Lloyds Register to develop new specifications for laser welding processes (Denney, 2011).

Improvements in diode technology that allowed greater power, better beam quality, and lower costs led to lasers spreading to a much wider audience. The flexibility of laser welding processes increased greatly when lasers capable of fiber delivery were developed, compared to the hard optics required for CO_2 lasers. Fiber lasers were also much easier to operate and maintain, provided greater robustness, and were available at a relatively low cost per kilowatt (Denney, 2011).

There are now alternatives to HLAW which do not require an active arc, and are referred to as laser hot wire (LHW) processes. In these processes the laser is used as a precision heating source and the filler wire is resistively heated between the contact tip and work part, allowing the laser to operate at a lower power.

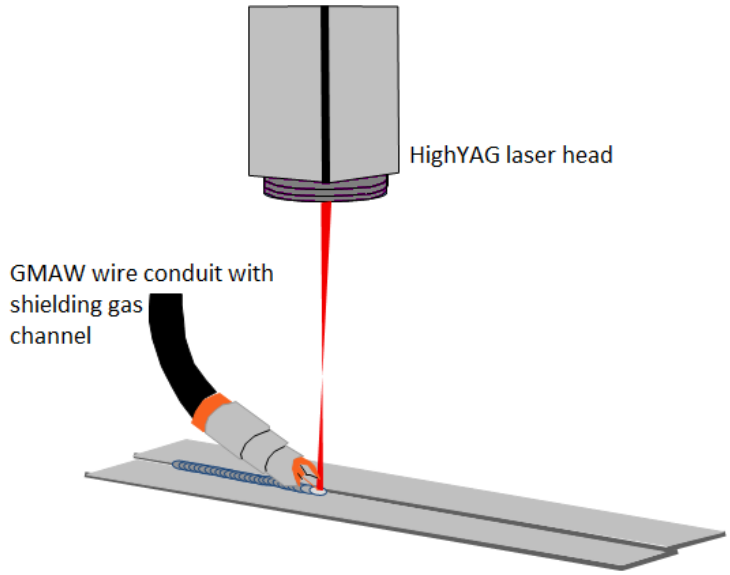

Figure 2. Schematic of the laser hot wire process (Denney, 2011).

In welding and cladding processes with a non-electrode filler wire, the heat from the molten pool conducts into the wire to melt it, contributing to the deposition rate and productivity. The limitation of this process in a cold wire system is that if the wire is fed too quickly into the pool and there is not enough heat in the pool to melt the wire, then the wire stubs into the bottom of the weld pool. A study on cold-wire laser cladding with simultaneous powder feeding experienced the difficulty with process control when using a cold-wire feed (Wang, 2007). Preheating the wire in a hot wire process increases the rate at which the wire is capable of being fed into the weld pool before encountering these issues.

The laser hot wire process is able to build upon the well-developed wire consumables used in welding processes, which are widely available for a number of alloy systems and sizes.

2.2.1. LHW Equipment

A typical LHW system will consist of a laser power source fed into fiber optic system with focusing controls mounted on a 5-axis programmable robotic arm. The consumable wire is fed from a drum or spool of wire outside of the build envelope and through a modified GMAW torch attached to a power source that is hot wire capable. Depending on the application, shielding gas may or may not be used; if it is required, it is fed through the torch head as in GMAW. Glove box systems may also be used, but are generally an unnecessary expense and reduces the productivity and build envelope.

Conventionally, hot wire systems used a constant current power source to resistively heat the wire between the contact tip and the puddle. Early hot wire systems used a Shielded Metal Arc Welding (SMAW or stick) or Gas Tungsten Arc Welding (GTAW) power supply to regulate the heating current in the wire. The problem with traditional power supplies, however, was that they were unable to actively prevent arcing from the wire. When an unwanted arc is formed, the heat input to the puddle is increased drastically (up to 4 times the hot wire heat input), so the earlier versions were limited in how much power could be used to heat the wire. If an unwanted arc forms, it can require extensive repairs or scrapping of parts, depending on the application. Some hot wire units feature very low open-circuit voltage (OCV) AC power sources to reduce unwanted arc events and extend the amount of power used in heating the wire. The low OCV aspect of the power source is designed to resist arc initiation and the zero cross of the AC polarity rapidly extinguishes arcs that do form.

However, using waveform controls in modern inverter power sources, arcs can be suppressed in even less time than the low OCV method (50-300 ms). These arcs still cause disturbances in the weld pool, but do not add significant amounts of heat to pool. This active suppression system from waveform control allows for the largest amount of pre-heat for the wire with minimal risk of unwanted arc events that are harmful to the weld or clad. These methods are used in the laser hot wire process at Company A, for instance. The increase in deposition rate saves both time and money, and the fine heat control from the laser is able to produce optimal properties in the deposited metal while minimizing the heat-affected zone (HAZ) (Peters, 2012).

2.2.2. LHW Process Control

2.2.2.1. Laser Power

In the LHW process, the laser is used a point heating source to finish the melting of the resistively heated wire consumable and is typically reported as laser beam irradiance for this process. The laser power required to create a fully molten pool is dependent on the alloy system, travel speed, wire feed rate, and wire temperature entering the molten pool. The input power affects the temperature gradient, cooling rate, and mode of solidification, influencing the microstructure and mechanical properties of the deposit and HAZ. The thermal gradient and cooling is generally described by the Rosenthal solutions for heat transfer.

Influence of the laser power (between 1.2 kW and to 2.6 kW) for a Ti-6Al-4V alloy system has been studied (Mok, 2008); the authors found that the bead width was largely

controlled by the laser power, though the bead height was more dependent on travel speed. In the same study, an increase in laser power was correlated to larger grain size and lower hardness, which would be expected from conventional cooling-rate dependency of these properties, for a slower cooling rate occurring at higher laser power.

2.2.2.2. Wire Feed Speed and Travel Speed

The travel and wire feed speed in the LHW process will influence the amount of material deposited per length of cladding, the cooling rate, bead shape, and mechanical properties. In the study on Ti-6Al-4V (Mok, 2008) the travel speed was linearly correlated to hardness and inversely correlated to bead height, but had little influence on bead width. The wire can be either front-fed (against the direction of travel) or back-fed (in the direction of travel) into the molten pool (Syed, 2005).

2.2.2.3. Shielding Gas

The molten pool in the laser hot wire process can be susceptible to oxidation from the atmosphere, which may lead to inclusions, decreased alloy recovery, and additional surface preparation between layers. However, unlike traditional welding processes the LHW process can deposit the filler wire without through-the-air droplet transfer, instead relying on surface tension transfer which reduces the amount of surface area exposed to the atmosphere, subsequently reducing the potential for oxidation. Additionally, LHW can have significantly faster solidification rates than arc processes by limiting superheating above the melting point of the alloy through maximizing the pre-heating of the wire and minimizing laser power, which reduces the amount of time the molten pool

is liquid, decreasing oxidation. As a result, the LHW process is less dependent on atmospheric control than other processes.

2.3. Direct Metal Deposition (DMD) and Laser Engineered Net Shaping (LENS®)

Both the LENS® and DMD processes are laser based additive technologies that utilize powder consumables. The LENS® process was developed by Sandia National Laboratories in 1996 as a freeform fabrication process for metallic materials (Keicher, 1996) and was commercialized by Optomec.

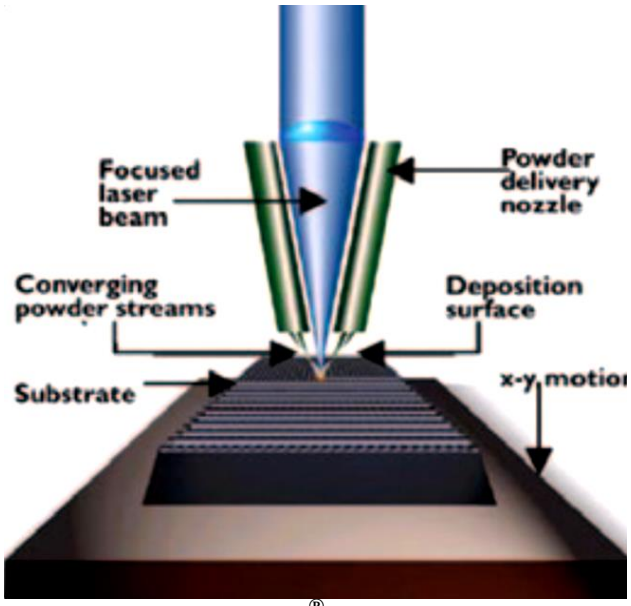

Figure 3. Schematic of the LENS® process (courtesy Optomec).

The DMD process was developed at the University of Michigan (Mazumder, 1997) commercialized by POM Group, which is now a part of Company E Technology, among others.

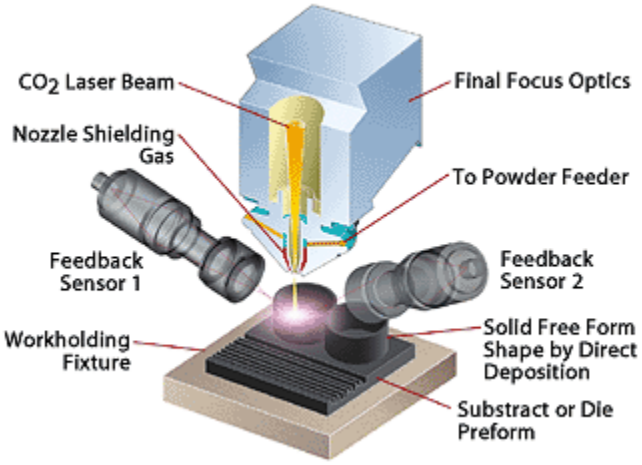

Figure 4. Schematic of the DMD process (courtesy Company E).

Both processes are extremely similar, falling under the definition of Directed Energy Deposition in ASTM F2792 – 12a (ASTM, 2012). A number of alloy systems have been studied in these systems including tool steels (Griffith,1999)(Mazumder, 1997), titanium alloys (Mazumder, 1997), stainless steels (Griffith, 1999)(Krishna, 2009)(Lin, 2006)(Mahmood, 2013)(Ganesh, 2012)(Alimardani, 2012), and Cu-30Ni (Bhattcharya, 2011).

2.3.1. Equipment

A typical LENS® station consists of an Nd:YAG laser and powder feed assembly attached to a 3-axis or 5-axis positioning system inside of a controlled atmosphere glove box which is vacated and then backfilled with an inert gas (i.e. argon). A typical DMD process also has a laser (CO_2 or fiber-delivered diode) attached to a 5-axis positional

system; but unlike LENS®, DMD® depositions are done outside of a glove box environment and use local shielding gas that is pumped through the powder nozzle to provide atmospheric protection. Both processes use machines which are outfitted with a number of sensors to monitor melt pool conditions and have computer-guided controls. Both also have a reservoir for the powder consumable, which feeds through the nozzle and deposits the powder through the laser into the melt pool.

2.3.2. LENS® and DMD Parameters

Deposits made using the LENS® and DMD processes can have wide variance in structural integrity unless care is taken in choosing deposition parameters. The three main variables for the LENS® and DMD processes are laser input power, powder flow rate, and travel speed which all strongly affect the heat transfer, thermal history, solidification, and deposit resolution.

2.3.2.1. Laser Input Power

The laser input power parameter is often reported as one of two terms: laser beam irradiance and laser beam intensity. Laser beam irradiance is the power density (output power per unit area) determined by dividing laser output power by its focus spot area. Laser beam intensity is the ratio of the laser output power to the focused laser spot diameter. Changes in the input power will affect the temperature gradient, cooling rate, and mode of solidification, changing the microstructure and consequently mechanical properties. The thermal gradient and cooling is described by the Rosenthal solutions for both 2-D and 3-D heat transfer depending on the deposit geometry.

At high levels of irradiance, lasers will produce keyhole welds, where the base material is heated past its vaporization temperature forming a cavity in the work piece with a high depth-to-width ratio. This effect is counterproductive to the LENS® process, since it is damaging to the previous levels of deposition; instead, lower levels of irradiance that are just sufficient for melting the powder feed and maintaining the molten weld pool are preferred.

The laser will have some energy transfer efficiency factor less than unity as a result of inefficiency in transfer from the laser to the work piece resulting from the optical reflectivity of the base material in conjunction with the angle of incidence, wavelength, and irradiance of the laser. As a result, the power output by the laser is not equivalent to the power transferred to the work piece.

In a LENS® or DMD process, the angle of incidence is fixed at 90° (perpendicular) to the x-y plane of the work piece. However, the effective angle of incidence can vary as a result of surface roughness and contours left by previous deposition layers, resulting in variable effective angle of incidence at the scale of the laser beam width. Surface roughness can be characterized when needed by use of a profilometer, and generally the surface is considered optically smooth when the surface roughness is less than the wavelength of the laser beam.

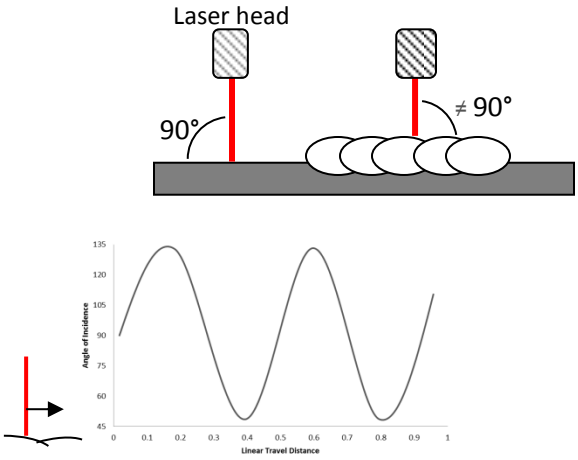

Figure 5. Change in local angle of incidence as a result of surface roughness

The wavelength of LENS® and DMD systems is typically 1064nm as a result of Nd:YAG being the dominant choice of laser (though there are other available energy levels as well). Higher wavelength lasers, such as CO_2 which typically emits at 10600nm, are up to ten times greater than Nd:YAG. By using the Nd:YAG laser at lower wavelengths, the photons have higher energy as described by the Planck-Einstein relation (Eq. 1) increasing absorption of the photons, which increases the laser power transfer efficiency.

$$E=hc/\lambda \qquad \text{Eq. 1}$$

2.3.2.2. Travel Speed

The linear rate at which the laser head travels across the work piece will be inversely related to the heat input per linear travel distance, deposition rate per linear travel distance, and deposit resolution.

2.3.2.3. Powder Feed Rate

The powder feed rate (also called powder mass flow rate) is analogous to wire feed speed in conventional welding processes. The higher the powder flow rate is, the higher the quench effect will be on the puddle; if the powder flow rate is too high with respect to the laser power, some of the powder particles may not melt (or may only melt partially) resulting in inclusions in the deposit.

2.4. Electron Beam Freeform Fabrication (EBF3)

Electron beam welding (EBW) is a high-energy beam fusion process used for high quality precision welds in aerospace and transportation (Schultz, 1993). It was adapted for additive manufacturing by NASA Langley Research Center and Company D, among others, under the name Electron Beam Freeform Fabrication (EBF3) (Dave, 1995)(Taminger, 2002)(Brice, 2002).

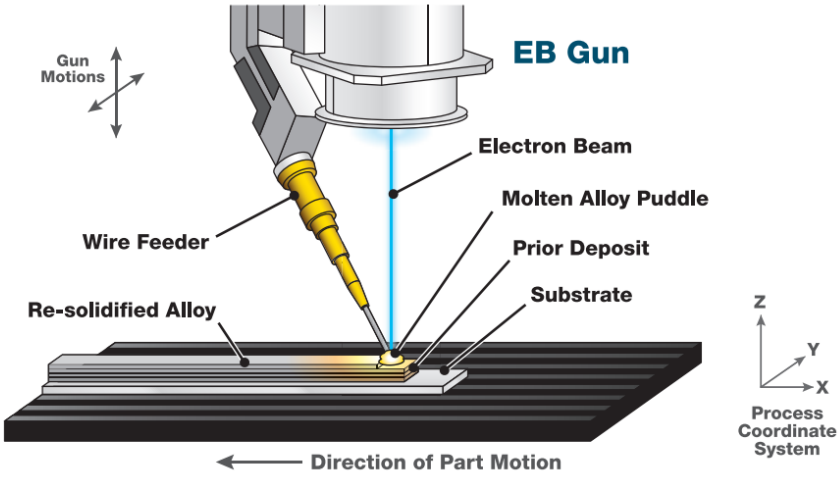

Figure 6. Schematic of electron beam freeform fabrication (courtesy Company D).

EBF3, similar to laser hot wire, has the benefit of using the well-established wire products used in welding processes, including EBW. There are variations that use a powder bed, referred to as Electron Beam Melting, but powder beds are not well-suited for repair or repurposing of die casting tooling.

2.4.1. EBF3 Equipment

The EBF3 process depends on the emission of electrons from a tungsten filament which has a low current passing through it to excite electrons, and is attached to the negative (cathode) end of a high-voltage power supply, with the positive (anode) side facing towards the workpiece and accelerating the electrons in that direction. A magnetic focusing system is used to channel the accelerated electrons into a beam with sufficiently small spot on the workpiece to fuse the wire consumable with the base material. Since electrons will readily interact with any atmosphere, the process is conducted in a high vacuum to limit interference with the beam. To use this process for additive manufacturing instead of welding, very little needs to change; the process is simply conducted on top of a substrate instead of between disjoined pieces. Typically the work piece moves beneath a stationary electron beam on an x-y coordinate table, but the process can also use deflection of the electron beam via a magnetic field to create more complex deposition geometries or introduce oscillations.

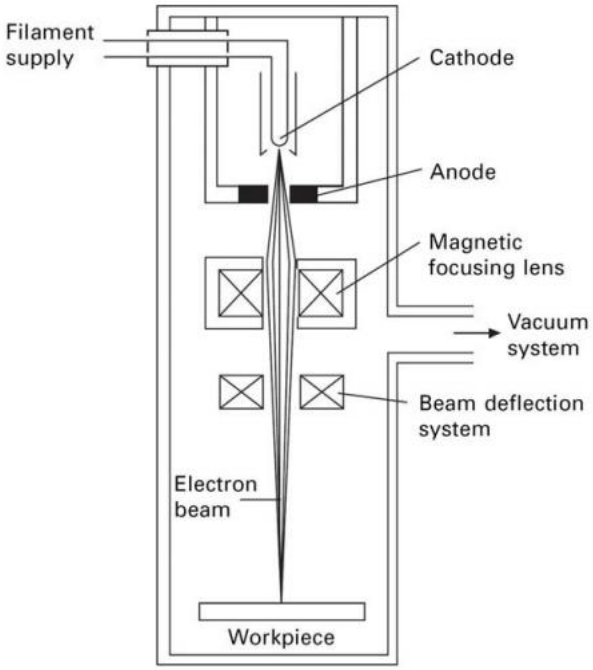

Figure 7. Principle of electron beam welding apparatus (Norris, 2006).

The kinetic energy carried by the accelerated electrons is transferred to the workpiece and consumable upon their collision, which provides the energy required to melt the consumable and base material in the melt pool. At higher energies, the metal can even be evaporated as a result of the vacuum pressure and high energy from the electron beam, but this would obviously be counterproductive to additive manufacturing.

2.4.2. EBF3 Parameters

2.4.2.1. Accelerating Voltage and Beam Current

The accelerating voltage exerted by the high-voltage power supply determines the kinetic energy of the electrons in the beam and, consequently, the power density of the beam. Likewise, increasing beam current will also increase the power density of the beam by freeing more electrons per unit time; for a fixed accelerating voltage, an increase

in beam current will increase the penetration depth. In practice, it is found that the easier and more flexible method of managing power density in EBF3 is to maintain a fixed accelerating voltage of 60 or 150 kV and vary the beam current (Schultz, 1993). Typically, for smaller focus diameters a high accelerating voltage and low beam current is preferred.

2.4.2.2. Travel Speed

The travel speed of the beam across the workpiece is a key factor in calculating heat input, since slower travel speeds will increase the dwell time of the beam on a unit length of the deposit. As a result, the travel speed can be correlated to the heating and cooling rate, fusion zone size, and penetration depth. An increase in the travel speed will result in a narrower bead with shallower penetration, as well as finer microstructure and increased hardness as a result of the increased cooling rate (compared to a slower travel speed).

2.4.2.3. Focus Current

The focus current passes through annual coils which control the magnetic field that guides the electron beam and determines the focal position. Varying the focal plane of the beam to be above (overfocused) or below (underfocused) the surface of the workpiece will increase the spot size of the beam, decreasing the power density (Schultz, 1993). Additionally, this control allows for layer-based additive manufacturing by re-adjusting the focal plane after each layer to create the next deposition without having to adjust the workpiece in the vertical direction.

Chapter 3: Experimental Methods

The testing for this study was conducted using H13 base metal blocks, machined to 155x114x19 mm (6.12”x4.50”x0.75”). For distortion measurements, the H13 base metal was used in both an annealed (15 HRC) and quenched and tempered (44-46 HRC) state; for all other tests the deposits were only conducted on tempered H13.

To get suitable testing specimens each process was used to deposit a block measuring at least 102x89x51 mm (4.0”x3.5”x2.0”). The deposition patterns varied, either 0°-0° or 0°-90° patterns, for the distortion measurements. For the tensile and impact testing, the deposits were created in the 0-90° pattern.

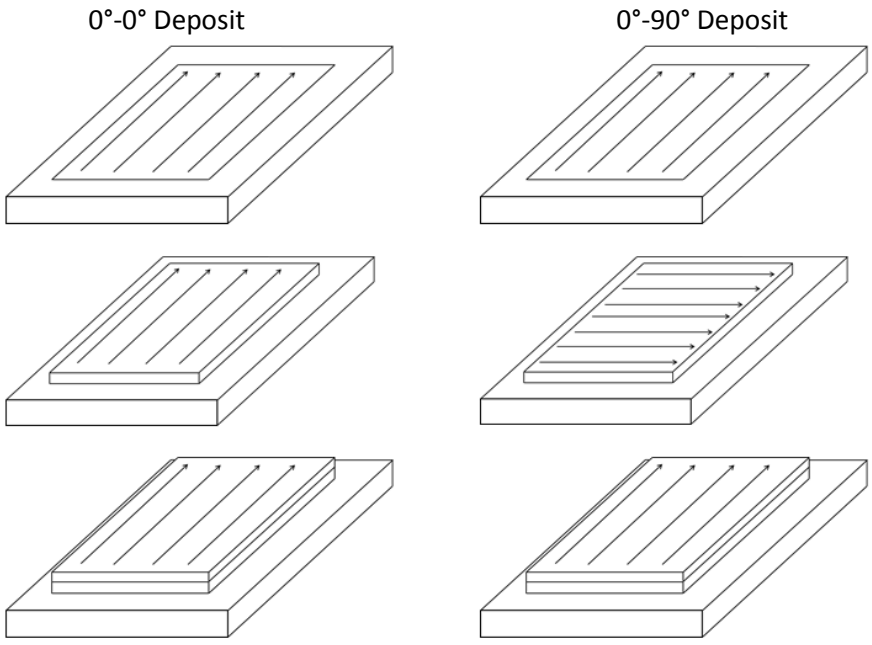

Figure 8. Deposition patterns of 0°-0° (left) and 0°-90° (right).

3.1. Testing Methods and specimens

Tensile, Charpy V-notch, and unnotched specimens were machined from the deposits, as well as sections for metallography and radiographic inspection. All mechanical testing specimens were machined and tested at third-party mechanical testing lab in Cleveland, Ohio.

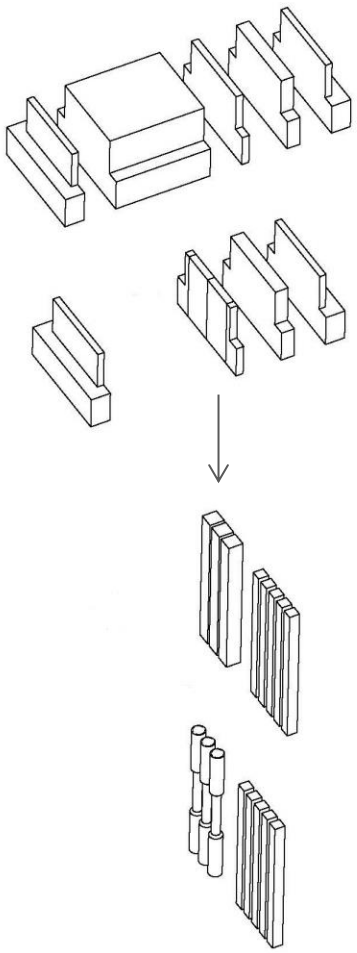

Figure 9. Procedure for machining specimens from the bulk deposit.

3.1.1. Tensile Testing

The tensile specimens were sub-sized specimen per ASTM A370-12a. They were machined out of a cross-section, as shown in Figure 9, incorporating the deposit and base metal to reduce the number of layers required for the deposit, while maintaining an all-deposit gage length.

3.1.2. Charpy V-notch and sub-sized unnotched Testing

The impact toughness of the deposits were tested according to full-sized Charpy V-notch and ½ sized unnotched specimens, both per ASTM E23-12c. The samples were machined from the vertical sections of the deposit, ensuring the inclusion of the notch in the deposit, sufficiently above the base metal interface.

3.1.3. Hardness Testing

Rockwell C hardness testing was conducted per ASTM E18 using 150 kg force and a 120° diamond cone indenter on flat specimen surfaces.

3.1.4. X-ray radiography

The radiography of the specimen cross-sections was conducted according to ASTM E-94 using reference radiographs ASTM E446/E186.

3.1.5. Metallography

The specimens for metallography were prepared using standard methods, using SiC abrasive pads and then a diamond suspension to polish to 1μm. The samples were

subsequently etched with 5% nital for 3-5 minutes for the maraging deposit and 5-10 seconds for the H-13 base plate to reveal the microstructure.

Chapter 4: Results

3.1. Laser Hot Wire – Company A

3.1.1. Description of the method and parameters

Cladding at Company A was done with a 10kW IPG Photonics laser with a HighYAG hybrid welding head on a Fanuc robot arm. The laser was operated at 6 kW power for all samples. The wire was preheated using a proprietary waveform capable of suppressing arc formation between the wire and the baseplate while maximizing Joule heating. Cladding was done with both maraging and H13 wire consumables fed at 15 cm/sec (350 ipm). Commercially pure argon shielding gas was fed through the wire head during deposition. The travel speed was 1.5 cm/sec (35 ipm).

Two different H13 steel plates were used as substrates, one annealed (15 HRC) and another air quenched and tempered (46.5 HRC), for distortion measurements. The deposition was done in either a 0°-90° pattern (each layer has alternating longitudinal and transverse passes) for distortion and mechanical testing, or a 0°-0° pattern (all layers' passes were done in the longitudinal direction) for distortion experiments. Between each layer deposition, the surface of the previous layer was cleaned with a wire wheel in order to reduce the occurrence of inclusions.

3.1.2. Experimental Results

With a travel speed of 1.5 cm/sec (35 ipm) the longitudinal 10.75 cm (4.25") passes took 8 seconds, while 9 cm (3.5") transverse deposits required 6 seconds. The total time

per layer was 3 minutes and 10 seconds to 3 minutes and 40 seconds. The total time per block varied depending on cleaning and reprogramming time, but averaged 4 hours and 38 minutes.

Block	Total Time
0-0° H13 Annealed Base Plate	4:12
0-90° H13 Tempered Base Plate	5:12
0-90° Maraging Tempered Base Plate	4:58
0-90° Maraging Annealed Base Plate	4:11

Table 3. Total deposition times for the four blocks from laser hot wire at Company A.

After cladding, the base plates were analyzed in a coordinate measuring machine (CMM) in order to determine the residual distortion for each process. Using the resulting coordinates, surface and centerline maps were used to compare the magnitude of distortion as shown in Figure 10 and Figure 11.

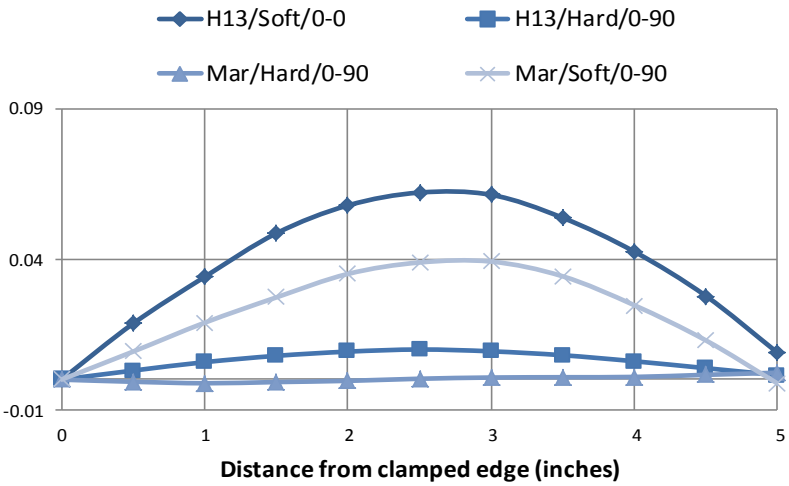

Figure 10. Centerline plots showing two-dimensional residual distortion.

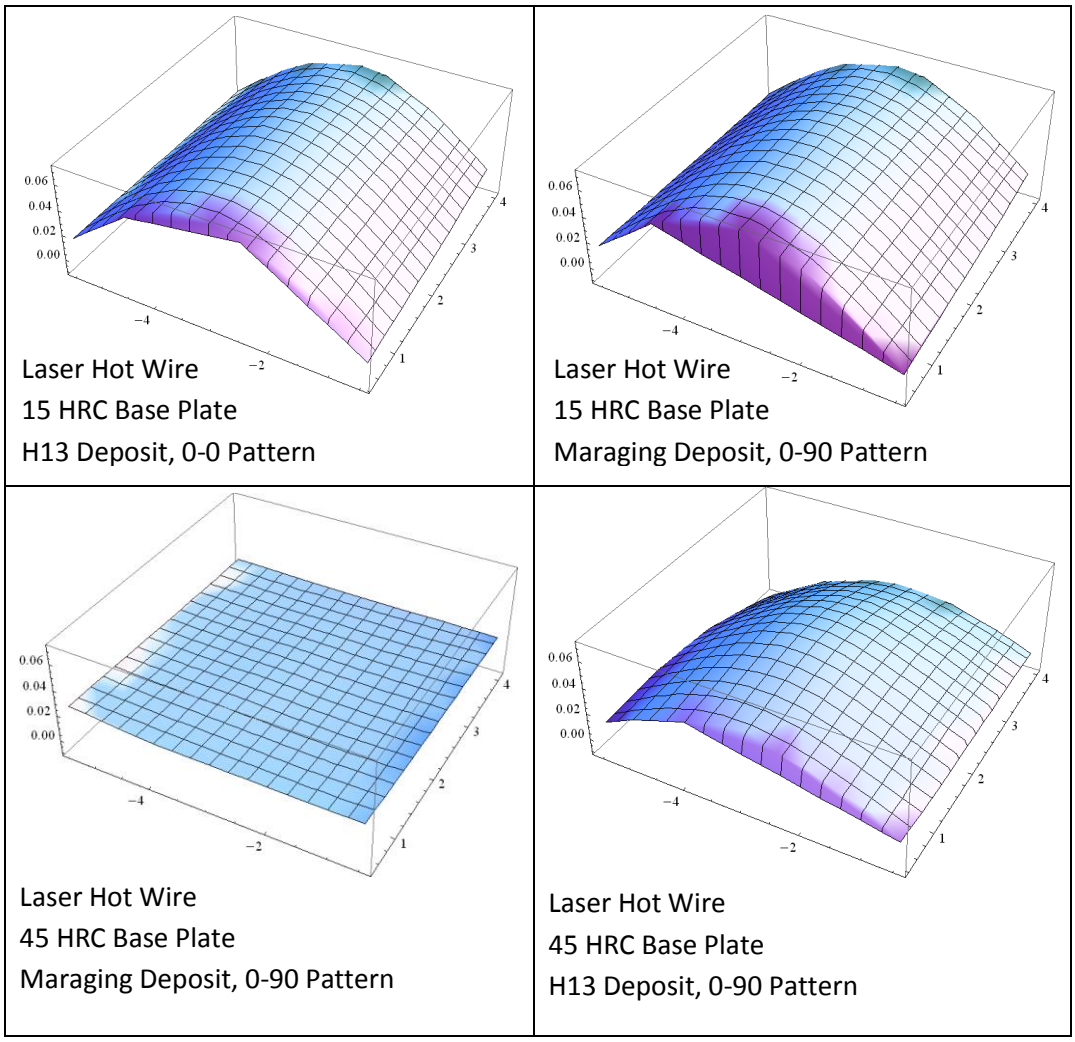

Figure 11. Surface plots for each plate showing three-dimensional residual distortion.

A number of hardness measurements were taken spanning the interface between the base metal and the deposition from the maraging steel deposition on tempered H13 base metal. From these, it was found that the deposited material was a very close match to the tempered H13 base material in hardness (44.7 - 46.9 HRC in the deposit vs. 46.5 HRC for base). There were also signs of over-tempering (or temper softening) in the base material as the hardness dropped by up to 8 HRC in the heat affected zone.

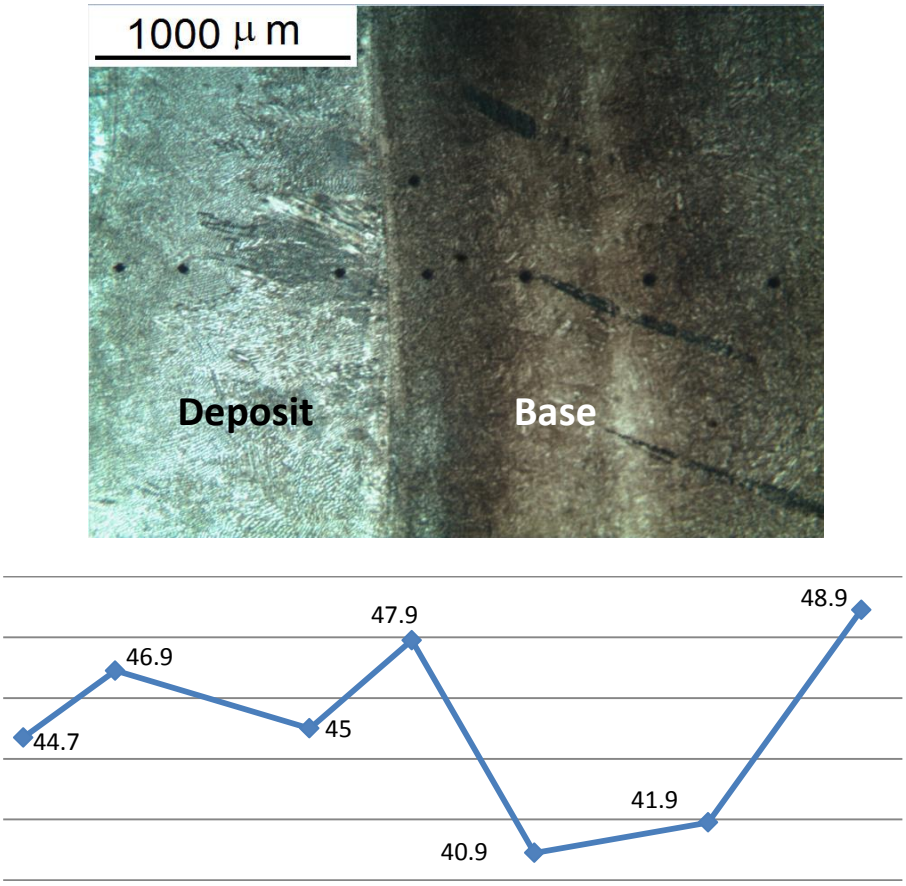

Figure 12. Hardness scan across the interface between the maraging deposit (left) and base metal (right).

Optical microscopy was also conducted on the base metal-deposit interface. As shown in Figure 13, there is a distinct heat affected zone (HAZ) in the base metal as expected. Adjacent to the deposit fusion line there is a partially re-hardened and re-tempered region which resulted in an increase in hardness initially before softening as a result of over-tempering as distance increases (the microstructure is still tempered martensite, however). The total measured HAZ extends approximately 1.2 mm from the interface.

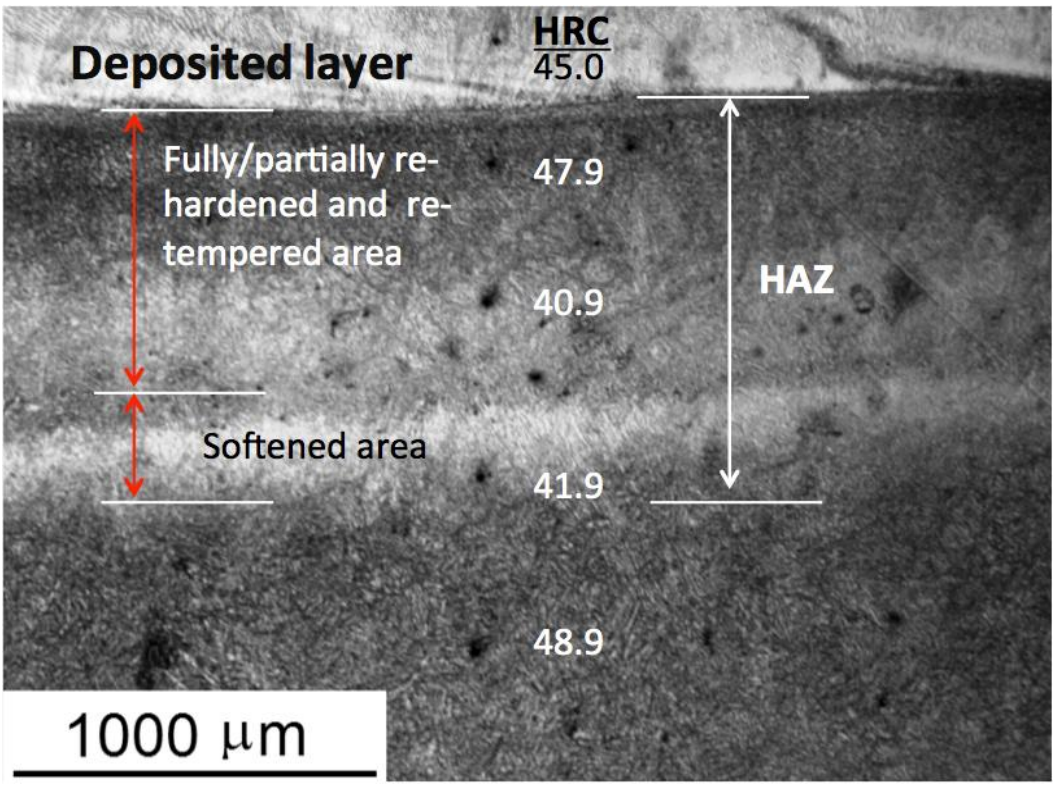

Figure 13. Optical micrograph of 1.2 mm deep HAZ from maraging deposit on tempered H13 base plate. The regions of the HAZ and hardness measurements are indicated.

Further microscopy was done on a scanning electron microscope (SEM) to investigate the microstructure further. Inspection of the deposited layers, as shown in Figure 14, indicated the prevalence of a martensitic matrix within the prior-austenite dendritic structure, and pools of austenite in the prior-interdendritic space. The dendrite spacing is measured to be 6 µm. Some micrographs also indicated the presence of some porosity, as shown in Figure 15**.**

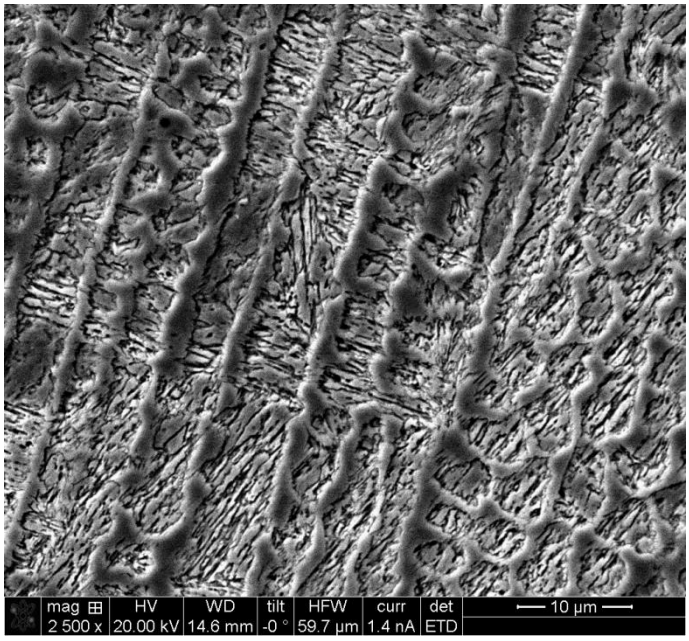

Figure 14. SEM image of prior-austenite dendrites with a martensitic microstructure in the deposit.

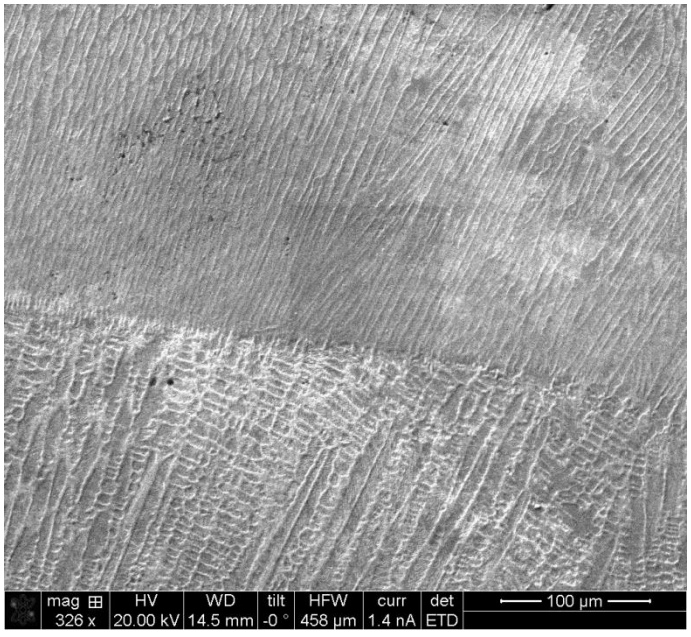

Figure 15. SEM image of the interface between two deposited layers with porosity highlighted.

SEM fractography was also conducted on maraging deposit Charpy V-notch fracture surfaces. There was a prevalence of ductile fracture in the sample, with shear fracture near defects as noted in Figures 9-11. EDX performed on the defect indicated Ti-Al oxides as the culprit phase (TiO2:Al2O3).

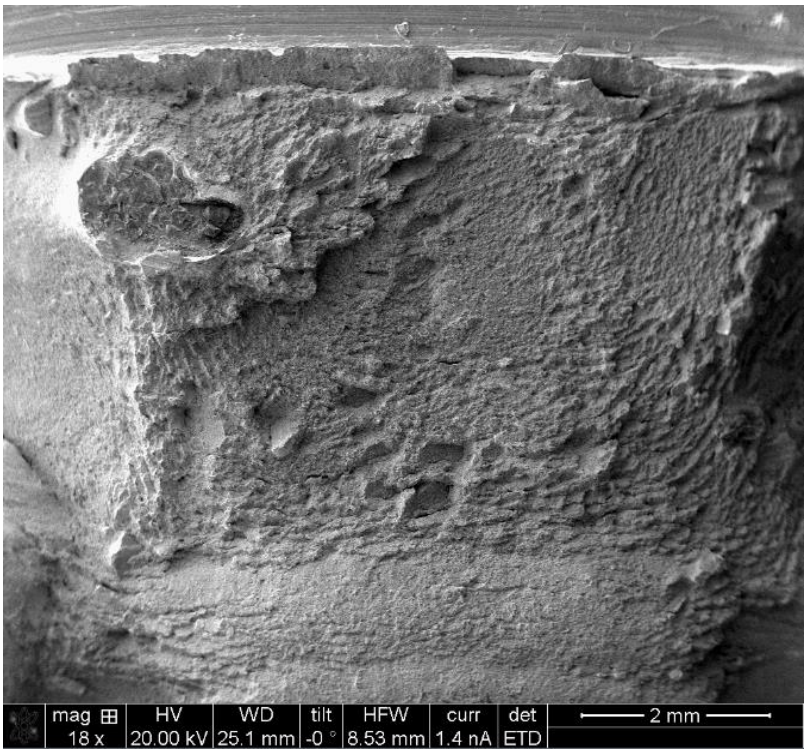

Figure 16. SEM image of the Charpy fracture surface.

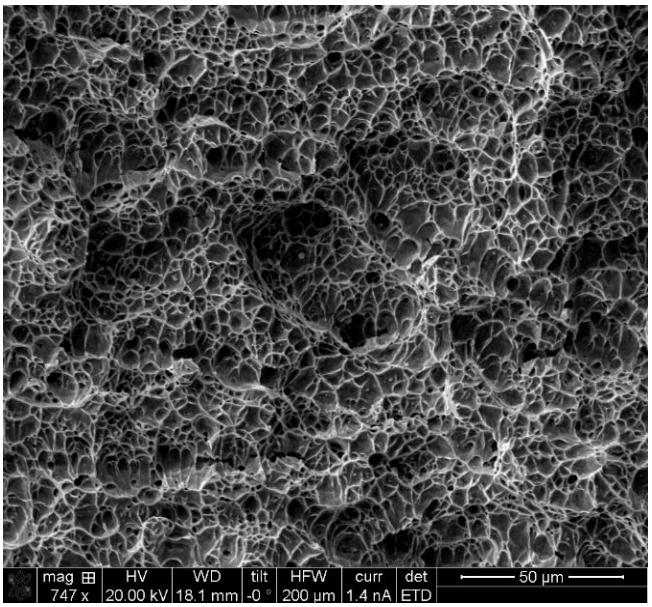

Figure 17. Dimpled CVN fracture surface, characteristic of ductile fracture.

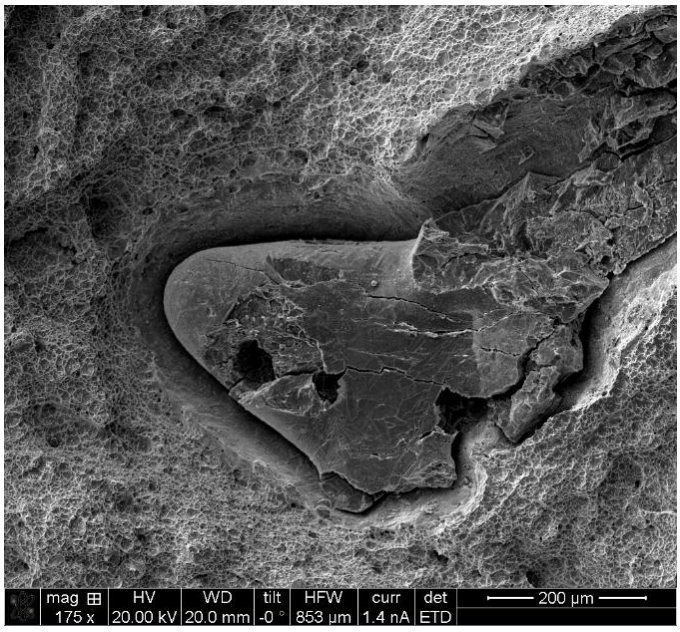

Figure 18. Oxide inclusion defect in fracture surface matching the stoichiometry of TiO_2:Al_2O_3.

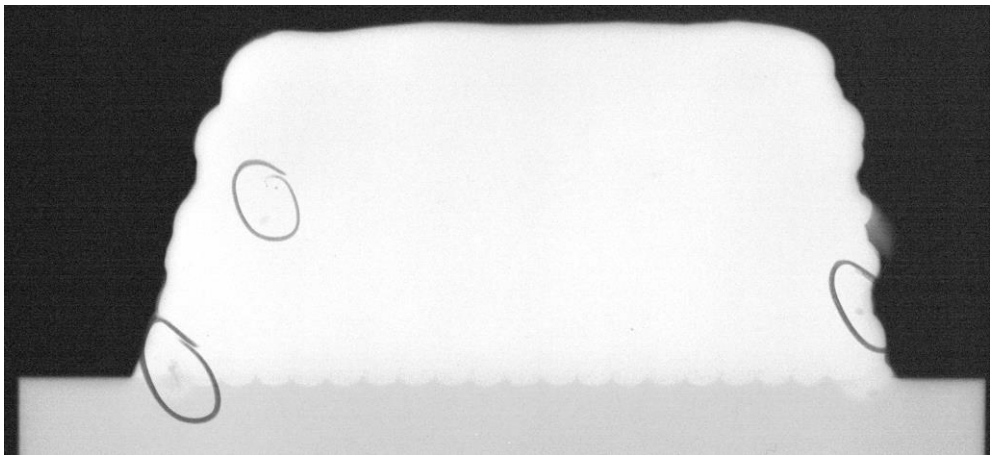

Figure 19. X-ray image of the LHW deposit from Company A (indications are circled).

The x-ray image in Figure 19 show three assorted round indications (circled) near the sidewall of the deposit. The indications appear to be low density and spherical, which are indicative of voids. Additionally, the penetration into the base metal is visible along the fusion line.

The Charpy and unnotched impact results are shown in Figure 20. The maraging deposit had an average toughness of 26 J (19 ft-lbs). The tempered H13 base plate had an average of 16 J (10 ft-lbs), almost half the toughness as the deposit. The amount of spread in individual test results was slightly lower for the maraging deposit than the base plate as well, which shows promise for consistent microstructure.

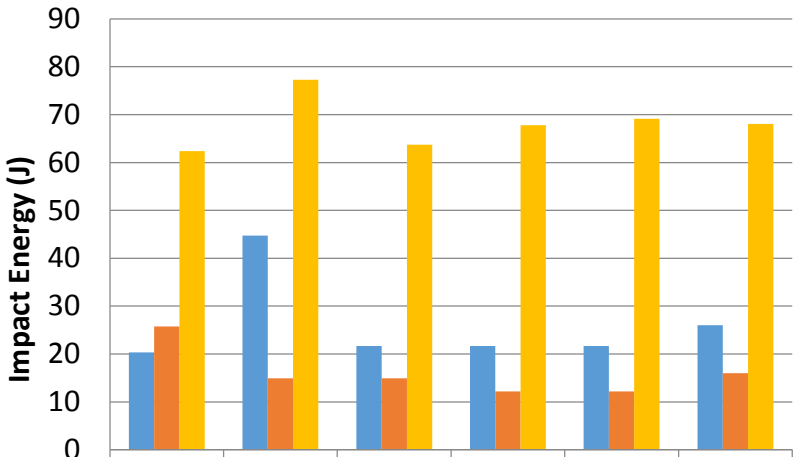

	1	2	3	4	5	Avg.
Maraging Charpy V-Notch (70°F)	20	45	22	22	22	26
H13 Base Plate CVN (70°)	26	15	15	12	12	16
Maraging Unnotched (70°F)	62	77	64	68	69	68

Figure 20. Charpy and unnotched impact toughness for the 0-90° maraging deposit and tempered H13 base plate at +70°F.

3.1.3. Discussion

The test blocks required 4-5 hours each to complete on the equipment at Company A. During the deposition on these test plates, the programming of the robot was done manually on-the-fly, which contributed to the deposition time and was a source of variance due to programmer skill and efficiency. Operator variance is not likely to be overcome in the long-run, because most repairs will be unique to their geometries and will require custom programming. The deposition time for this method compares favorably to other deposition alternatives; however, it is likely that all methods will be highly operator dependent.

The data collected from the laser and CMM showed that there was little residual distortion in the plates after deposition. The most extreme case of distortion was 0.06" out-of-plane at its maximum, which is two orders of magnitude lower than the dimensions of the plate when depositing H13 on the annealed H13 base plate. When the same wire was used on the tempered H13 plate, which is the condition dies are used in, the distortion dropped to 0.01" at its maximum. These are promising results that demonstrate the repair process will not result in considerable distortion or residual stresses. Some tool geometries may be more susceptible to distortion or more negatively affected by even small amounts of residual stresses, such as these, so it should not be disregarded.

The differences in distortion seen between the H13 and maraging deposits on annealed (soft) plate, shown in Figure 11. Surface plots for each plate showing three-dimensional residual distortion. , highlights the effect of directionality on residual stresses. On the stronger quenched and tempered plates, it can be seen that the deposit composition does not have a pronounced effect on distortion. On the annealed plates, however, the H13 was deposited solely in the longitudinal direction (0°-0° pattern), while the maraging was deposited in a 0°-90° pattern, switching between longitudinal and transverse deposition directions between each layer. The distortion was strongly reduced in the maraging sample as a result, so the 0°-90° deposition pattern is strongly preferred for distortion reduction.

The hardness achieved in the maraging deposit, which matched the tempered base metal, was a key achievement for material selection. However, the temper softening seen in the base metal near the interface may be a significant factor for the design of the geometries to be repaired. Though softening below the deposit is unlikely to be a significant issue (because it is 'protected' by the harder overlay), softening of the base metal on the die surface near the edges of the deposit may shorten the life of the repaired die.

Optical and scanning electron microscopy showed the expected martensite. The ductile fracture surface is a good indication of high deposit quality. The inclusions and porosity that were identified will need to be further examined to determine the origin of these defects. It's possible that different consumable manufacturers could produce cleaner welds through additions of surface tensions modifiers and arc stabilizers, which could more evenly distribute the liquid in the pool. The voids seen near the sidewall in the x-ray image are process-dependent and may be reduced or eliminated by increasing shielding gas or heat input.

The Charpy V-notch results indicate that the maraging deposit provides sufficient toughness at 19 ft-lbs, compared to the 10 ft-lb average from the tempered H13 base plate. The maraging deposit also has a lower standard deviation (2.91 vs. 4.22 in the base plate).

3.2. Laser Hot Wire – Company B

3.2.1. Description of the method and parameters

Cladding at Company B was done with a Nd:YAG laser and GMAW power source operating in hot wire mode. The laser was operated at 6 kW power for all samples and the wire was preheated using a hot wire waveform.

The experiments conducted at Company B were done on H13 base plates machined to 6.12”x4.50”x0.75”. The base plates were in the tempered (46.5 HRC) condition. The deposition was done in the 0°-90° pattern (each layer has alternating longitudinal and transverse passes) and was subsequently sent sectioned for sub-sized tensile (0.250”), full-sized Charpy V-notch, and sub-sized unnotched impact specimens. Between each layer deposition, the surface of the previous layer was cleaned to reduce the occurrence of inclusions.

3.2.2. Experimental Results

Optical microscopy was conducted on the maraging deposit and base metal-deposit interface. Inspection of the deposited layers as shown in Figure 21 and Figure 22 indicated the prevalence of epitaxial growth with cellular and dendritic morphology. The interdendritic spacing is measured to be 10 μm.

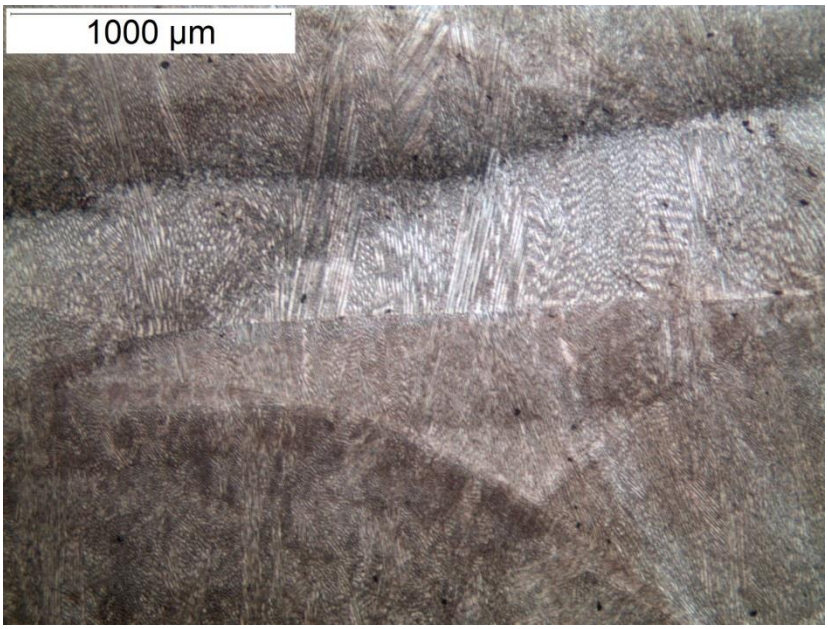

Figure 21. Micrograph of the LHW clad maraging from Company B.

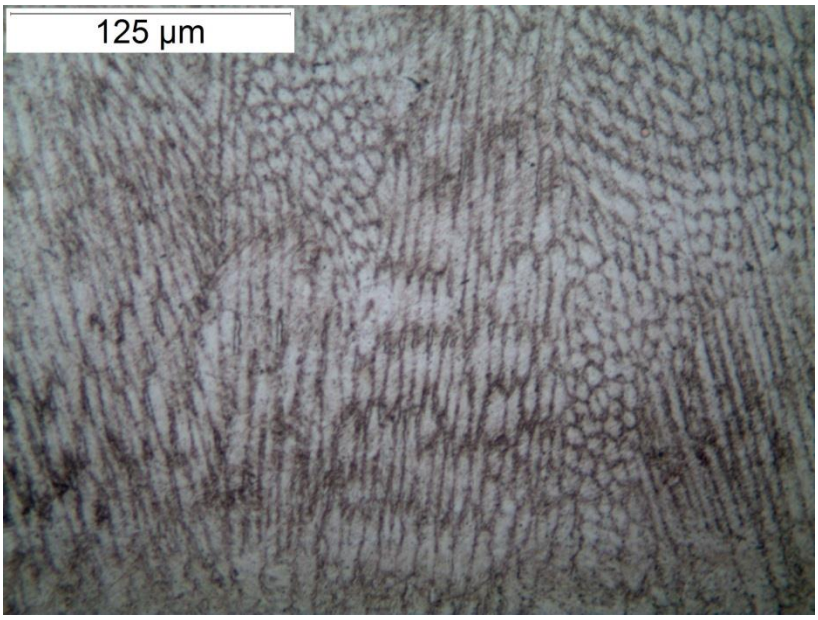

Figure 22. Micrograph of the LHW clad maraging from Company B.

As shown in Figure 23, there is a heat affected zone (HAZ) in the base metal. The total measured HAZ extends approximately 0.4 mm into the base metal from the

fusion line. Microhardness measurements taken across the interface on the maraging deposit show a decrease in hardness in the HAZ near the fusion line, with a minimum at 35.4 HRC. The base plate after cladding stayed within its original hardness range, near 45 HRC. The LHW-clad maraging deposit was over hardened compared to the base metal temper, peaking at 55 HRC and averaging 51 HRC for the 2mm nearest to the fusion line.

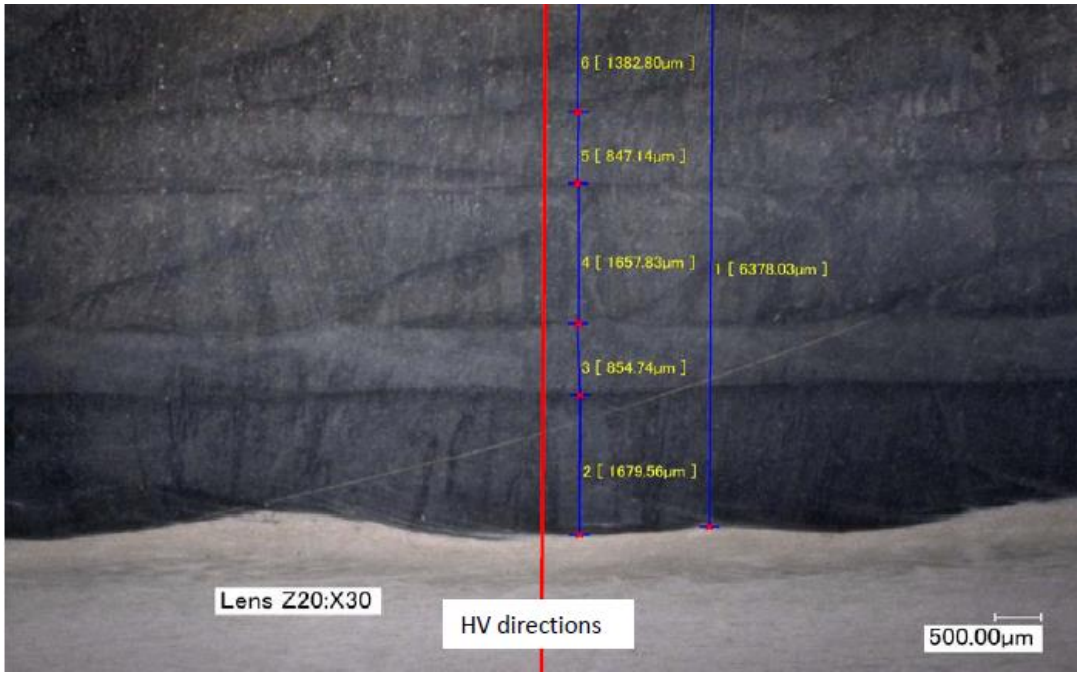

Figure 23. Micrograph of the LHW clad maraging deposit including base metal fusion line and HAZ from Company B.

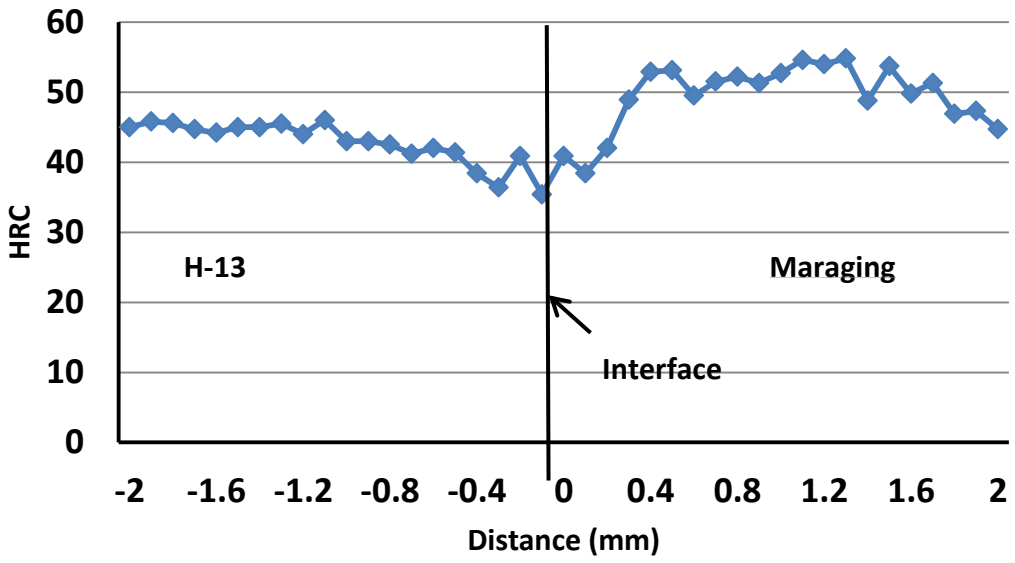

Figure 24. Microhardness measurements spanning the base metal-deposit interface from the LHW maraging steel at Company B.

The x-ray image in Figure 25 shows large indications in the top right corner of the deposit. The majority of the cladded block, however, is a sound deposit which is reinforced by the consistent tensile and Charpy V-notch results in Figure 26 and Figure 28.

The sub-sized tensile (0.250") results in Figure 26 show good tensile and yield strength (160 and 158 ksi, respectively) with adequate elongation (11%). The consistency between specimens is very high for strength and elongation, which is indicative of a consistent structure in the deposit, supported by the x-ray. The tensile specimens are shown in Figure 27, and all three exhibited cup-cone fracture.

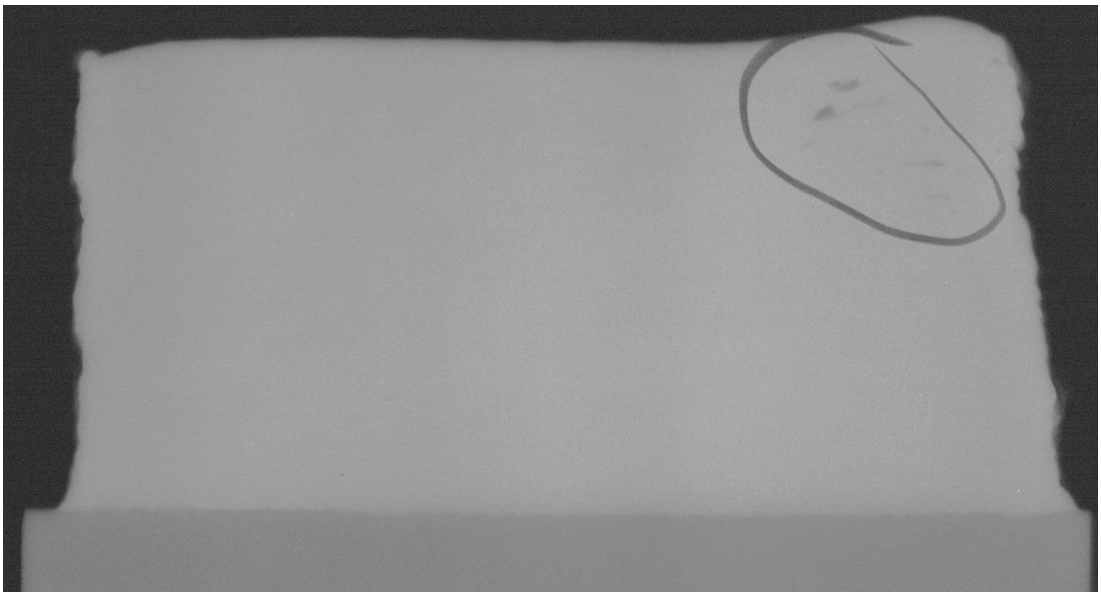

Figure 25. X-ray image of the LHW clad maraging deposit from Company B. A dense region of large indications is circled in the top right.

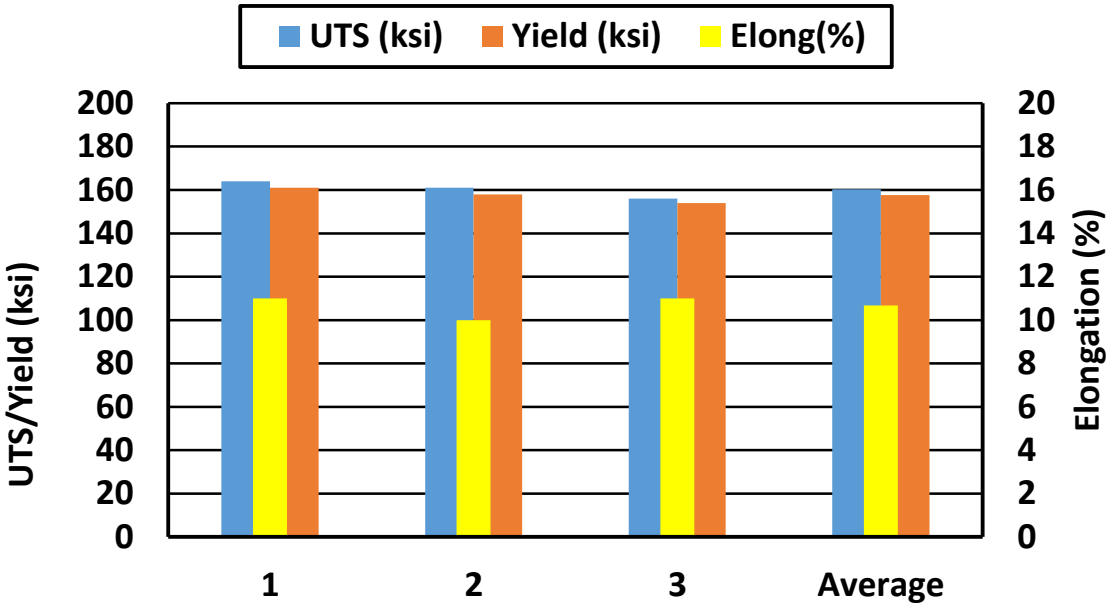

Figure 26. Sub-sized tensile (0.250") results for the LHW clad maraging deposit from Company B.

Figure 27. Image of sub-sized tensile bars (0.250") from the LHW clad maraging deposit from Company B.

The Charpy V-notch and unnotched impact results are shown in Figure 28. The average Charpy toughness was 28 J (21 ft-lbs), and unnotched average was 46 J (34 ft-lbs). There is relatively little spread in individual test results for the Charpy V-notch samples, ranging from 22 to 35 J (16 to 26 ft-lbs); however there is more spread in the unnotched samples, ranging from 9 to 64 J (7 to 47 ft-lbs). It would be expected to see more spread in unnotched samples, since the crack initiation is more difficult in some samples than others depending on surface finish and contained inclusions, whereas Charpy V-notch specimen have the notch stress concentrator to somewhat normalize the variance from crack initiation.

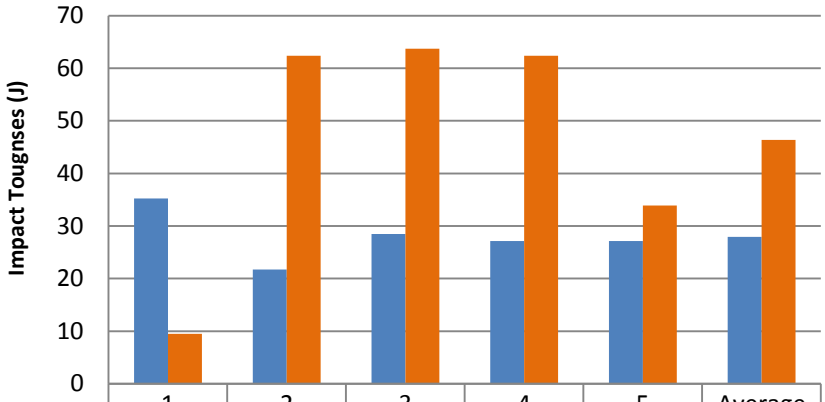

	1	2	3	4	5	Average
Maraging Charpy V-Notch (70°F)	35	22	28	27	27	28
Maraging Unnotched (70°F)	9	62	64	62	34	46

Figure 28. Full-sized Charpy V-notch and sub-sized unnotched impact specimen results for the LHW clad maraging steel deposit from Company B.

3.2.3. Discussion

The hardness of the maraging deposit (50-55 HRC) was over hardened compared to the as-received tempered base metal (45 HRC). The HAZ experienced a decrease in hardness compared to the unaffected base metal with a minimum at 36 HRC; the base metal in this test maintained its original temper after deposition (45 HRC).

The x-ray showed a cluster of large indications in the top right corner of the cladded block, while the remainder of the block had few scattered, round indications throughout the deposit. Combined with the consistency seen in the tensile bars (0.250") and impact specimens, the structural integrity of the cladding appears to be very good overall, despite the localized inclusions.

The mechanical properties of the laser hot wire cladded maraging steel from Company B are very competitive with other processes. The Charpy V-notch average (28 J) was very good compared to the base metal results tested on the Company A block (14 J), and the individual results showed a reasonably small amount of scatter. The unnotched specimens had one low toughness specimen (9 J) but overall strong impact toughness. The sub-sized tensile results (Figure 26) show good strength and elongation for the three specimens, attributed to the low density of voids and impurities. All three specimens exhibited ductile cup-cone fracture (average 11% elongation) and acceptably high tensile (160 ksi) and yield (158 ksi) strength compared to other processes.

3.3. GMAW - Company C

3.3.1. Description of the method and parameters

The experiments conducted at Company C were conducted on H-13 grade base plates machined to 6.12”x4.50”x0.75”. The base plates were in the tempered (46.5 HRC) state.

The cladding procedure was done using the GMAW process with 1.2mm diameter (0.045”) maraging steel wire fed at 2.1 cm/sec (50 ipm) or 10.3 g/min. The GMAW power source was operated using an AC waveform at 300 A and 12.6 volts (3.78 kW) at a travel speed of 762 mm/min (30 ipm). The resulting single pass bead was 6.5 mm toe-to-toe and 2.2 mm high.

The deposition program was written to first deposit a single pass around the outside of the block, and then the rest was filled in using the 0-90° deposition pattern.

3.3.2. Experimental Results

The deposition of maraging steel at Company C took 1 hours and 53 minutes total. Each pass took 5 seconds, and each layer took 3 minutes and 30 seconds. In total, 22 layers were deposited on the substrate to reach the required deposition height of 6.4 cm (2.5”).

Block	Total Time
0-90° Maraging	1:53

Figure 29. Deposition time for GMAW at Company C.

Optical microscopy was conducted on the deposit and base metal-deposit interface. Inspection of the deposited layers as shown in Figure 30 and Figure 31 indicated the prevalence of epitaxial growth with dendritic morphology as the primary microstructure. The interdendritic spacing is measured to be 14 µm.

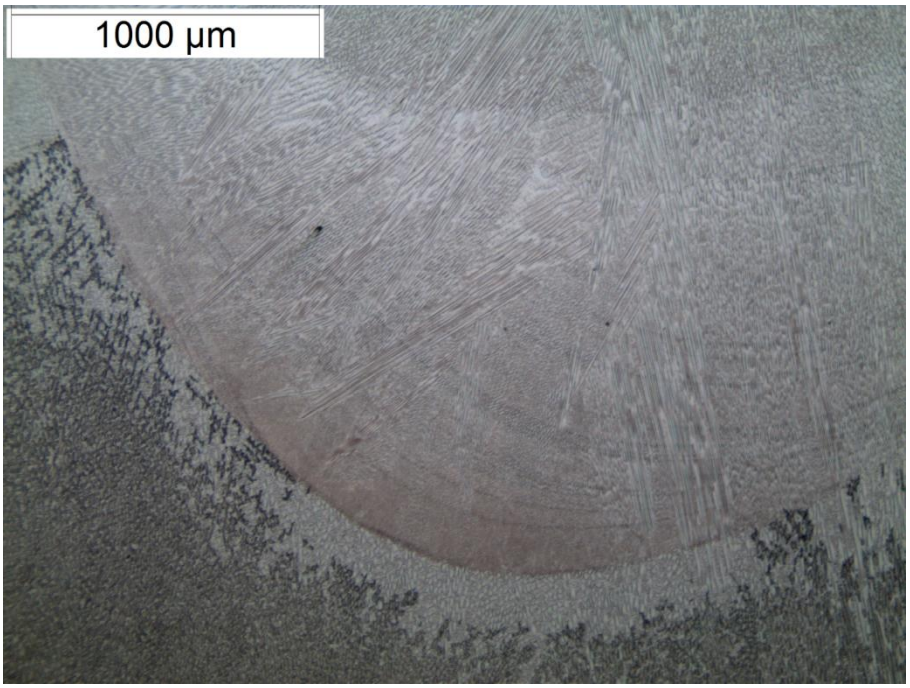

Figure 30. Optical micrograph of GMAW maraging deposit from Company C, taken along the deposit-base metal interface.

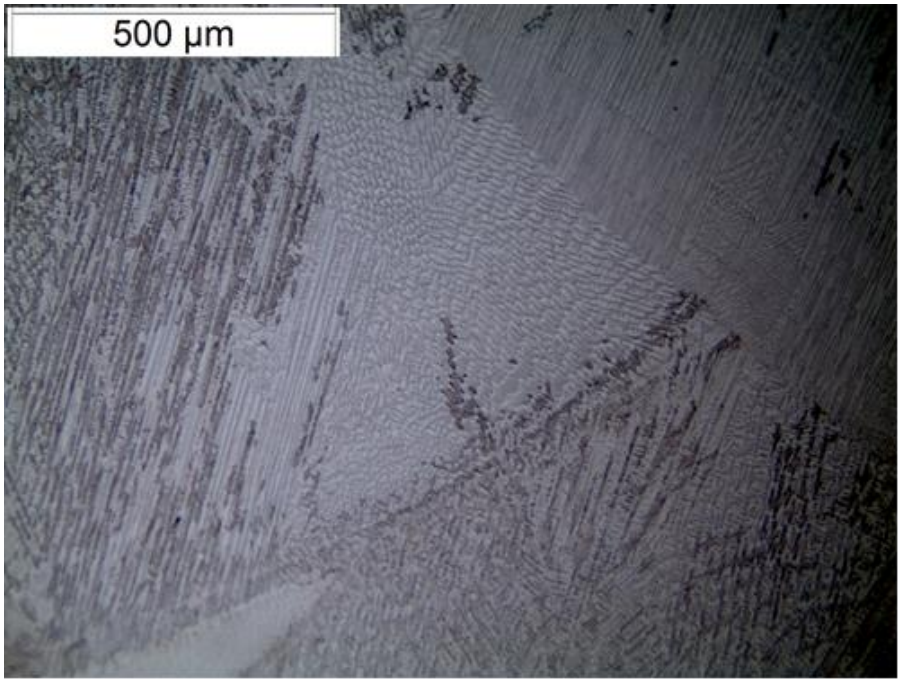

Figure 31. Optical micrograph of GMAW maraging deposit from Company C.

As shown in Figure 32, there is a heat affected zone (HAZ) in the base metal. The total measured HAZ extends approximately 1.6 mm into the base metal from the fusion line. Microhardness measurements taken across the interface on the maraging deposit (Figure 33) show an increase in hardness (up to 52 HRC) in the HAZ near the fusion line, followed by softer base metal (41 HRC) before returning toward the as-tempered hardness (45 HRC). The deposited maraging steel had lower hardness than the as-received base metal (35-40 HRC).

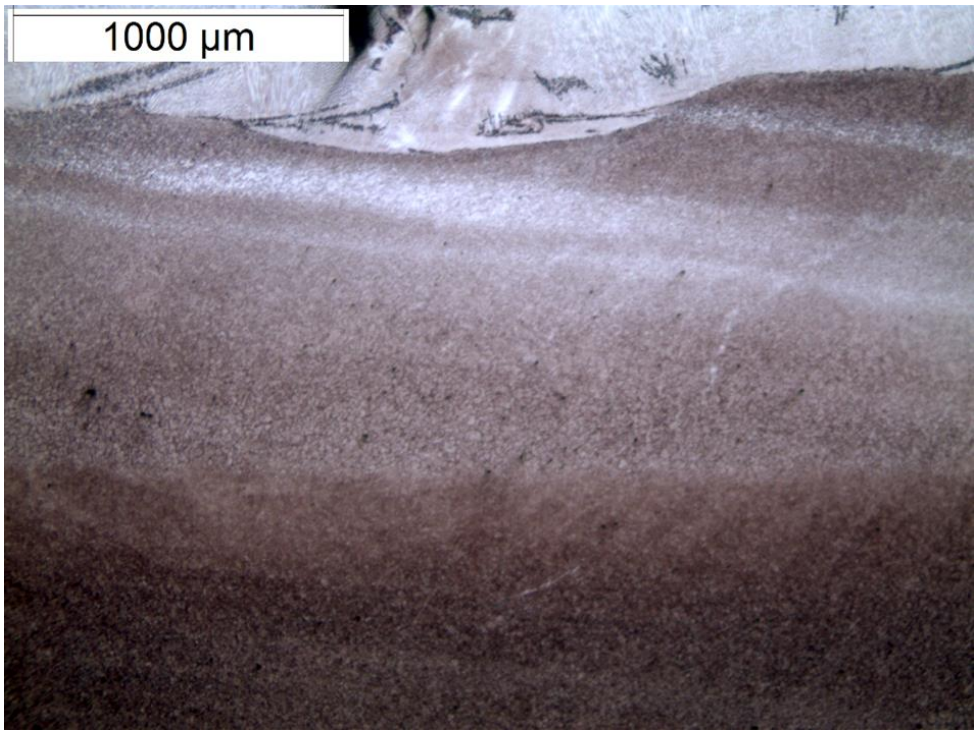

Figure 32. Optical micrograph of HAZ from the GMAW maraging deposit from Company C.

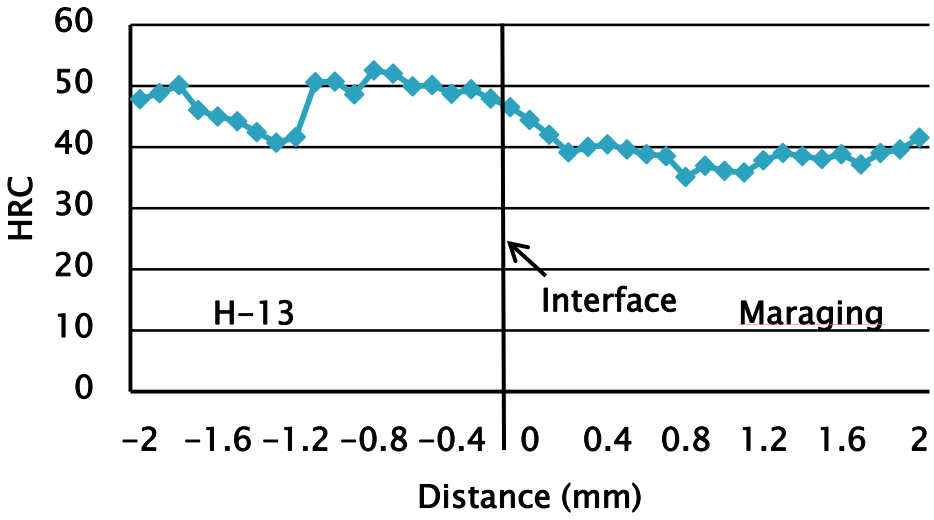

Figure 33. Microhardness measurements spanning the interface between the GMAW maraging deposit and H13 base metal from Company C.

The x-ray image in Figure 34 shows large indications throughout the deposit. The indications appear to be low density and spherical, which are indicative of voids. Additionally, the voids appear to align along each layer and at the toes of each pass.

The tensile results in Figure 35 show relatively weak tensile strength (122 ksi average); additionally, two of the three specimens have no measureable 0.2% offset yield strength and low elongation (0.8% average). The tensile specimens are shown in Figure 36, and all three exhibited brittle fracture.

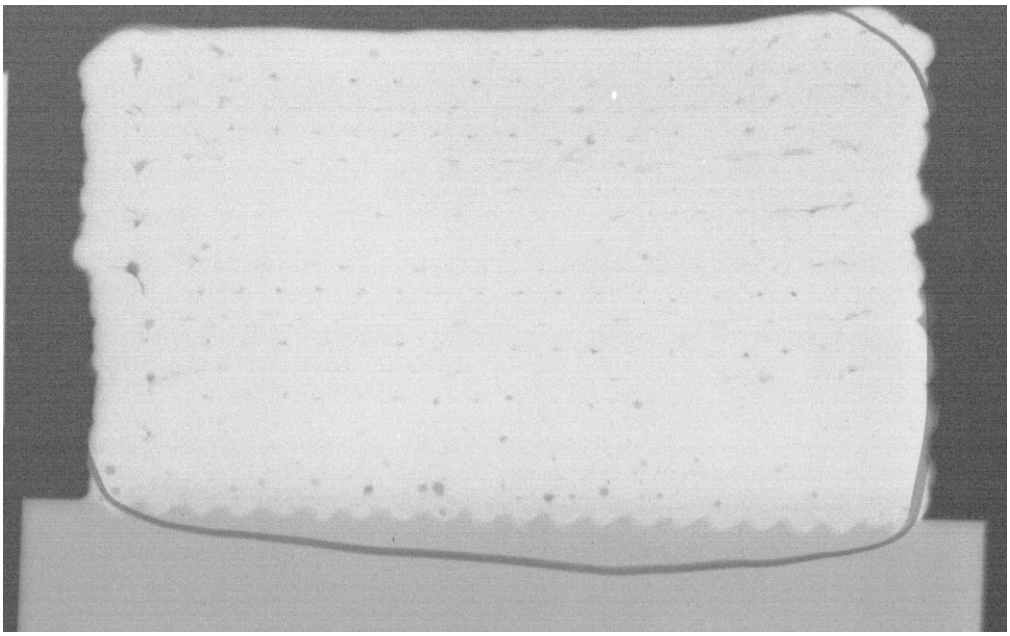

Figure 34. X-ray image of a section of the GMAW-cladded maraging block from Company C.

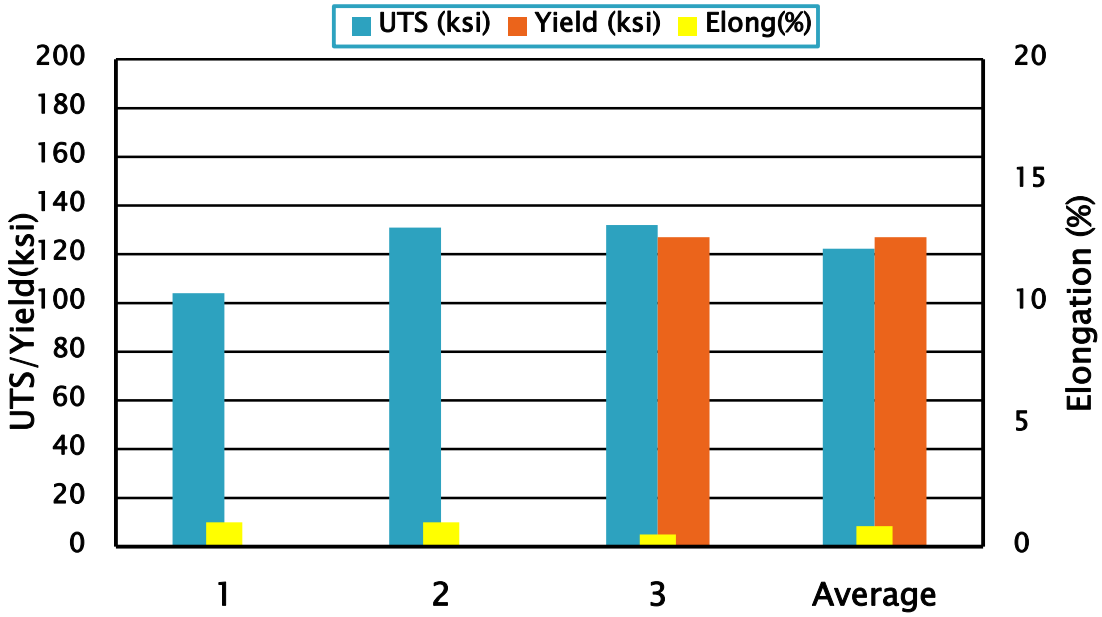

Figure 35. Sub-sized tensile (0.250") properties of the GMAW maraging deposit from Company C.

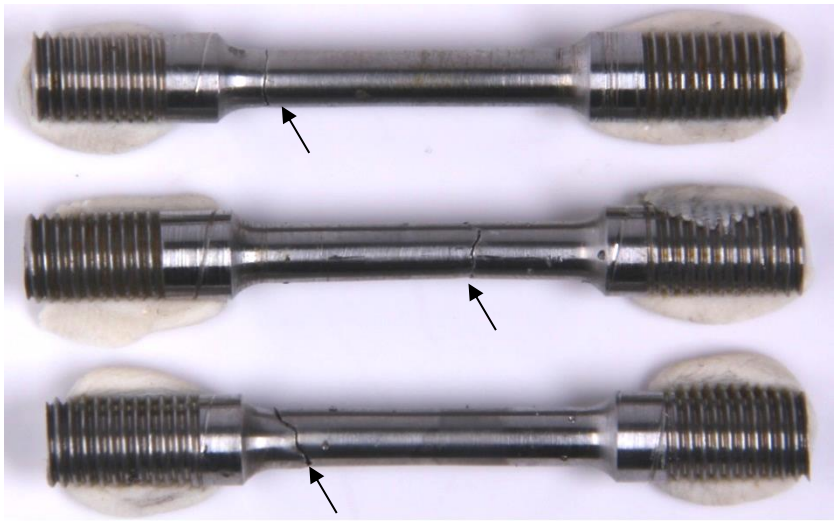

Figure 36. Image of the sub-sized tensile specimens from the GMAW maraging deposit from Company C. The fracture locations are indicated with arrows.

The Charpy and unnotched impact results are shown in Figure 37. The average Charpy V-notch toughness was 55 J (41 kJ), and unnotched average was 60 J (44 ft-lbs). There is somewhat significant spread in individual test results but no exceptionally low specimens, ranging from 37 to 68 J (27 to 50 ft-lbs) for the Charpy tests, and 45 to 73 J (33 to 54 ft-lbs) for the unnotched samples.

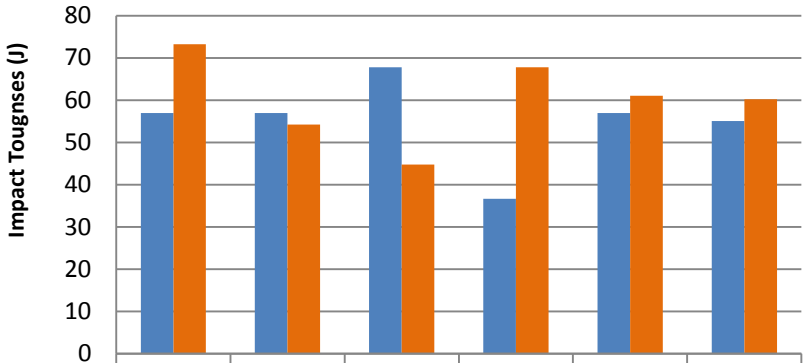

	1	2	3	4	5	Average
Maraging Charpy V-Notch (70°F)	57	57	68	37	57	55
Maraging Unnotched (70°F)	73	54	45	68	61	60

Figure 37. Full sized Charpy V-notch and subsized unnotched impact results for the GMAW maraging steel deposit from Company C.

3.3.3. Discussion

The deposition of the GMAW cladded block at Company C took one hour and fifty-three minutes total, excluding the break for the evening. Each pass took 5 seconds, with each 2.2 mm layer taking 3 minutes and 30 seconds.

The hardness of the maraging deposit (35-40 HRC) was softer than the as-received tempered base metal (45 HRC). The HAZ experienced an initial increase in hardness (up to 52 HRC) in the HAZ near the fusion line, followed by softer base metal (41 HRC)

before returning toward the as-tempered hardness (45 HRC). The x-ray showed an extremely large number of indications throughout the block.

The Charpy V-notch average (55 J) was very good compared to the base metal results tested on the Company A block (14 J); despite the individual results showing a fair amount of scatter there were no exceptionally low values. Likewise, the unnotched samples had good toughness and lower scatter. The good toughness is a counterintuitive results given the results from the x-ray, as the voids in the sample would cause samples that include them to have very low values. This deleterious effect on mechanical properties was seen in the tensile specimens which had extremely brittle fracture (0.8% elongation) and low tensile strength (122 ksi).

3.4. Electron Beam with Wire – Company D

3.4.1. Description of the method and parameters

The experiment conducted at Company D utilized H13 base plates machined to 6.12”x4.50”x0.75”. The base plates were in the tempered (46.5 HRC) condition.

The cladding procedure was done with 1.2 mm (0.045”) maraging steel wire fed at 11.6 cm/sec (275 ipm). The electron beam was operated at 7.0 kW and the resulting single pass bead was 0.5 mm toe-to-toe and 1.5 mm high. The molten pool is protected from the atmospheric contamination by ultra-low vacuum in the chamber, required for the electron beam operation. The deposition program was written using the 0-0° deposition pattern in the longitudinal direction.

One thermocouple was placed on the plate and two were placed on the fixture, as shown in Figure 38, to record the temperatures during deposition.

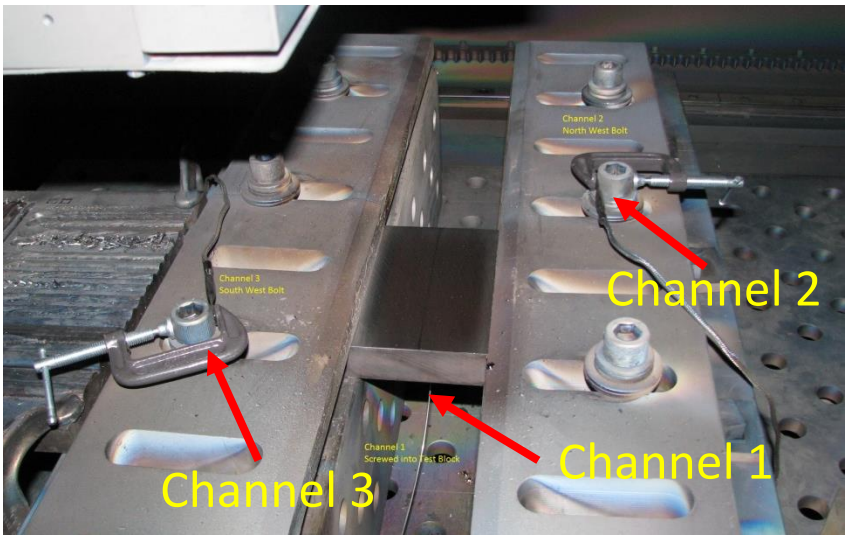

Figure 38. Photograph of the clamped test block in the electron beam chamber at Company D.

3.4.2. Experimental Results

The deposition of maraging steel at Company D took 7 hours and 20 minutes total. Each pass took 16 seconds, and each layer took 4 minutes. The layers were deposited one layers are a time, and allowed to cool for 10 minutes between layers to mitigate runaway interpass temperature. In total, 30 layers were deposited on the substrate to reach the required deposition height of 6.4 cm (2.5”). Since the electron beam chamber is evacuated to ultra-low vacuum during operation, cooling is controlled by conduction through the clamping, with limited radiative losses.

Block	Total Time
0-90° Maraging	7:18

Table 4. Deposition time for electron beam cladding at Company D.

Optical microscopy was also conducted on the deposit and base metal-deposit interface. Inspection of the deposited layers as shown in Figure 39 and Figure 40 indicated the prevalence of epitaxial growth with cellular and dendritic morphology.

As shown in Figure 41, there is a heat affected zone (HAZ) in the base metal. The total measured HAZ from the micrograph extends approximately 0.25 mm into the base metal from the fusion line. However, microhardness measurements taken across the interface on the maraging deposit show a slight decrease in hardness in the HAZ near the fusion line, and an overall softer base metal than the original as-tempered steel (35 HRC, compared to 45 HRC in the as-received state). This is due to the dependence on conductive cooling through the base plate in the vacuum chamber, which caused the plate to sustain an average temperature of 590°C (1100°F) for over five hours during the deposition procedure (see Figure 43 for temperature profile and Figure 38 for thermocouple locations on the fixture). As such, the entire base plate is heat-affected.

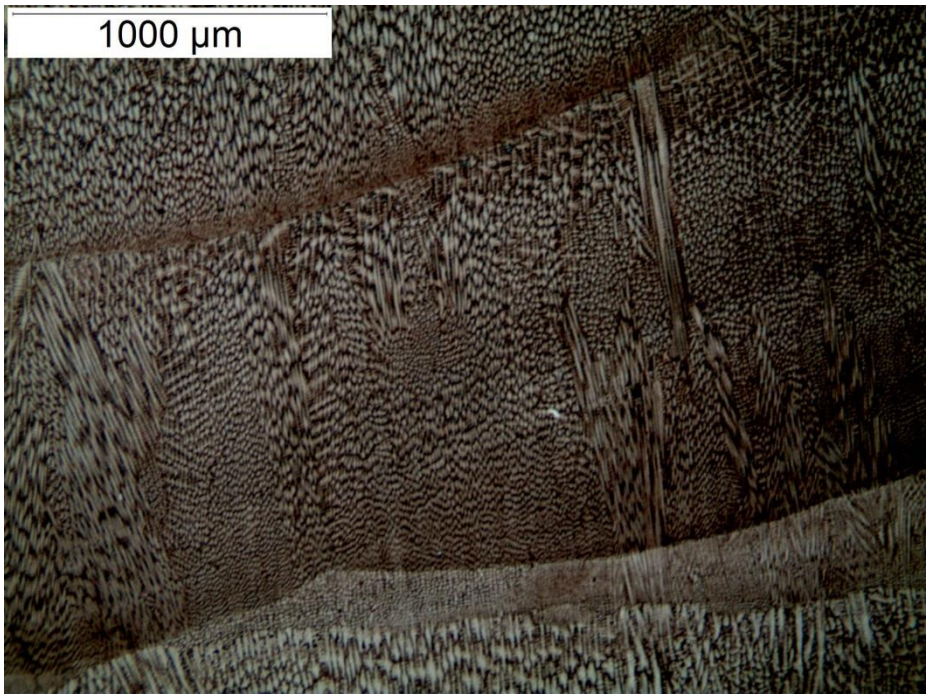

Figure 39. Micrograph of electron beam cladded maraging deposit from Company D.

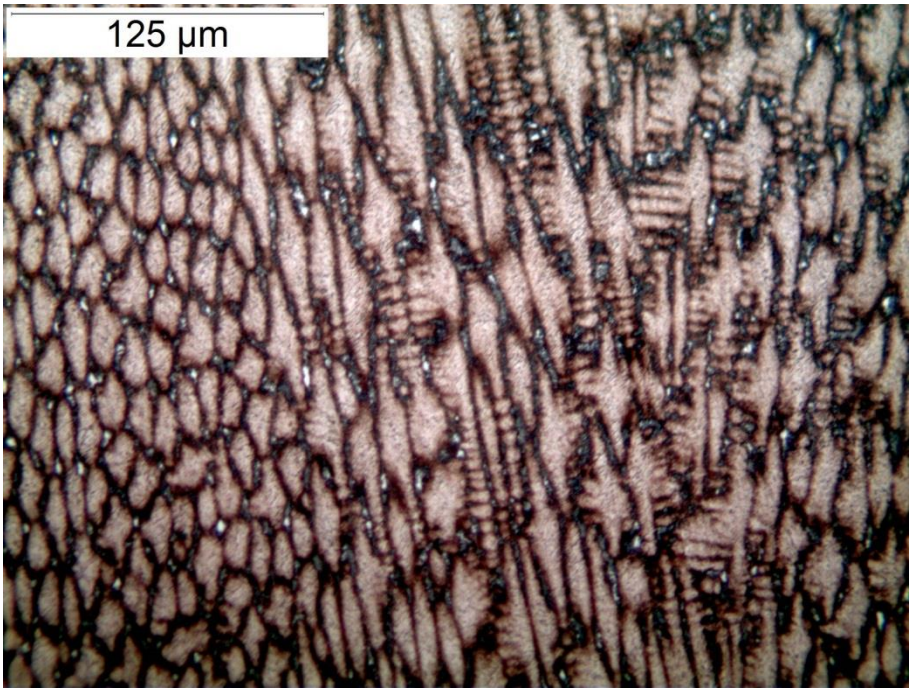

Figure 40. Optical micrograph of electron beam cladded maraging deposit from Company D.

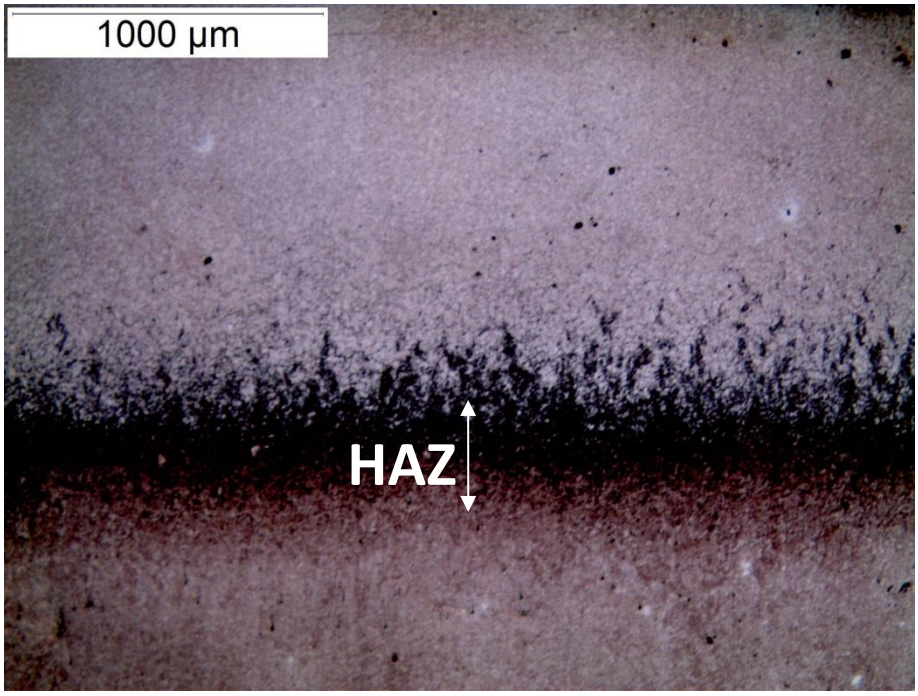

Figure 41. Optical micrograph of the fusion line and HAZ in the electron beam cladded maraging deposit from Company D.

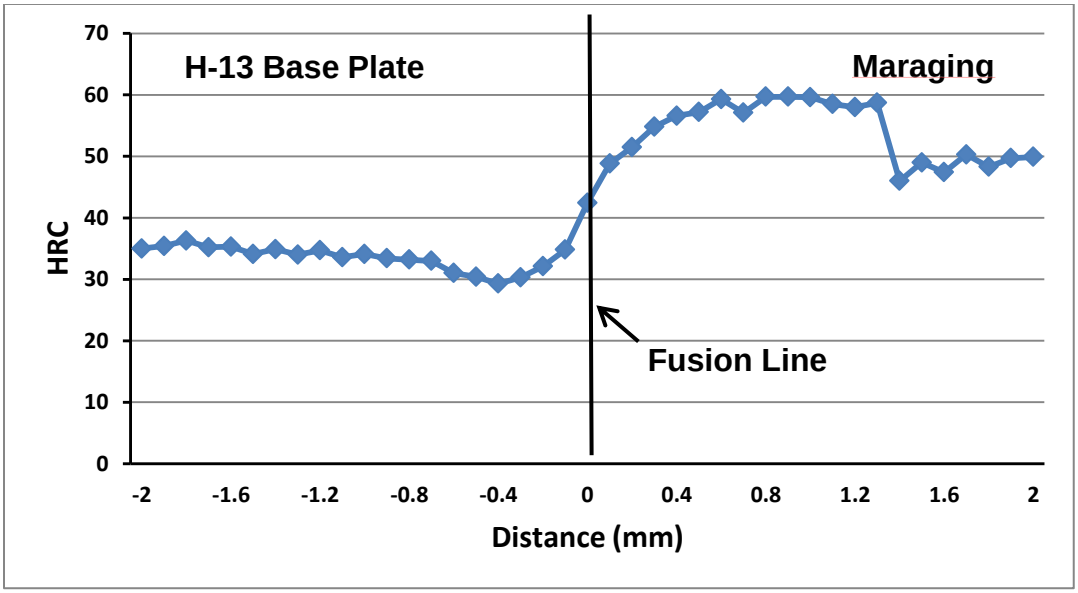

Figure 42. Microhardness measurements spanning the fusion line and heat affected zone for the electron beam cladded maraging deposit at Company D.

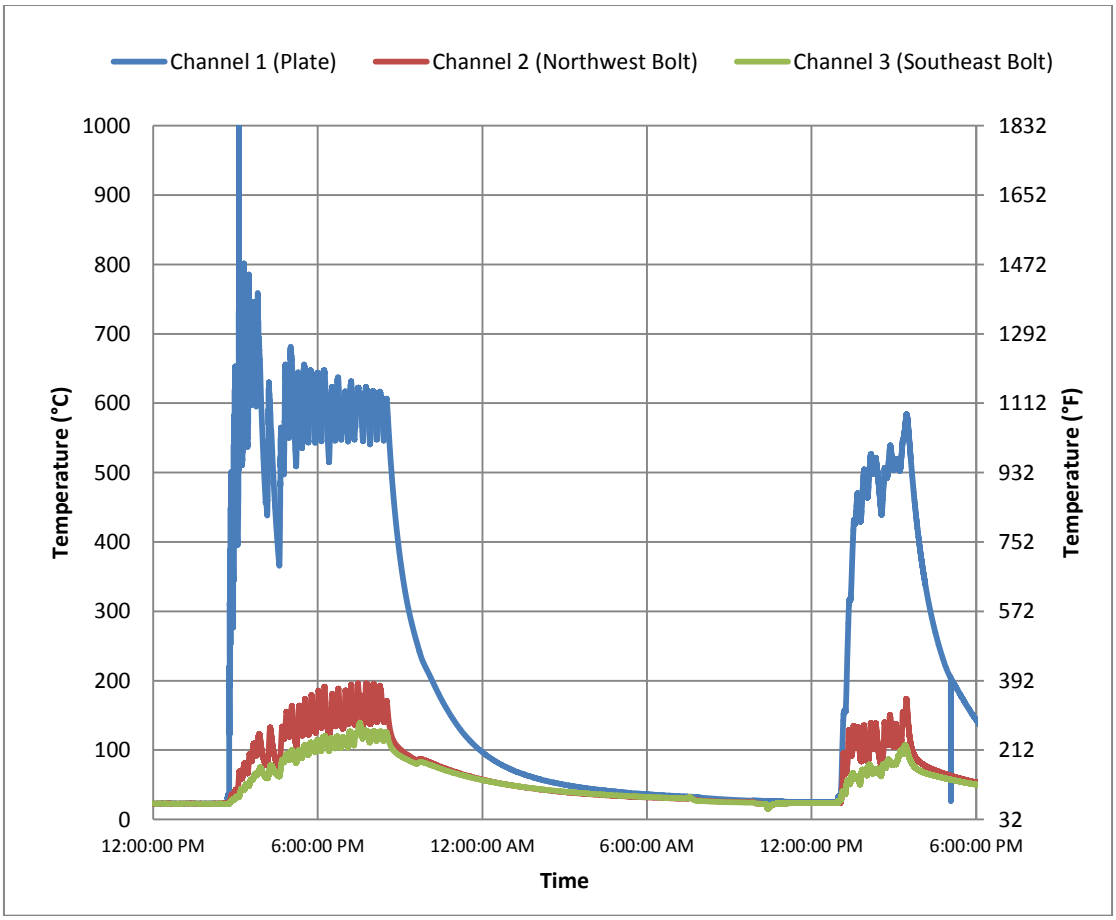

Figure 43. Temperature profile for the base plate and two bolts on the fixture for the duration of the EBF3 deposition at Company D.

An x-ray image of a section from the cladded block is shown in Figure 44. There are significant indications through the width of the block for the bottom third of the plate. This appears the line up with the deposits from the first day, while the deposits from second day appears to have much fewer indications, despite no changes in deposition parameters.

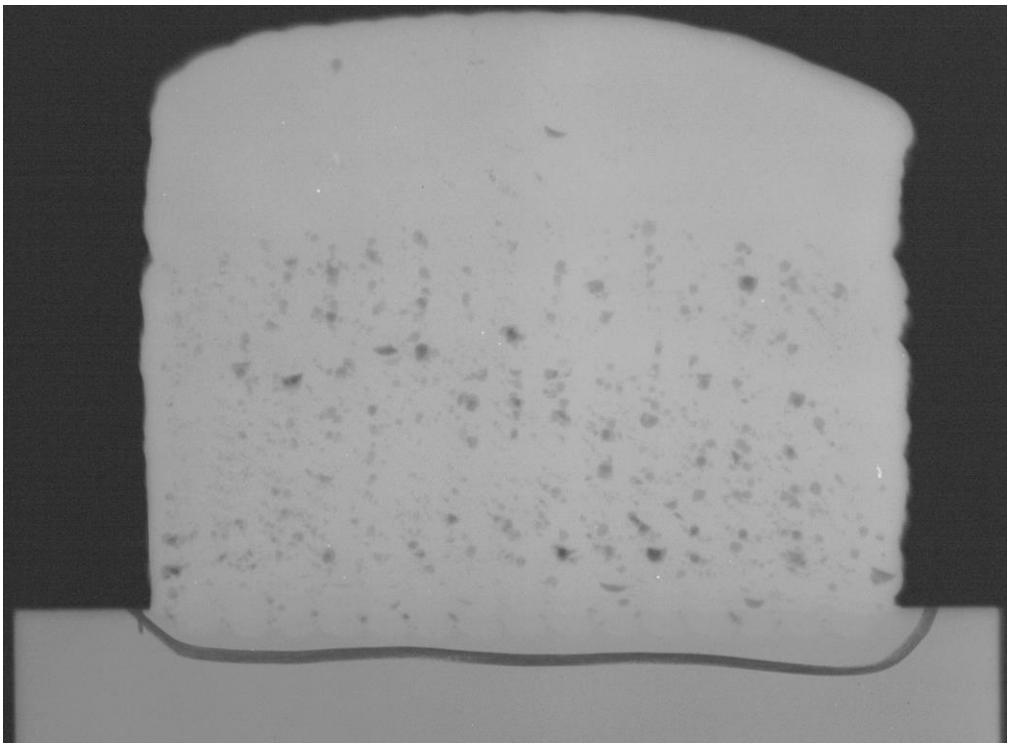

Figure 44. X-ray image of the electron beam cladded maraging deposit from Company D. Significant indications are shown throughout the sample.

The Charpy and unnotched impact results are shown in Figure 45. The average Charpy toughness was 12 J (8.6 kJ), and unnotched average was 18 J (13 ft-lbs). There is significant spread in individual test results, ranging from 7 to 27 J (5 to 20 ft-lbs) for the Charpy tests, and 5 to 33 J (4 to 24 ft-lbs) for the unnotched samples.

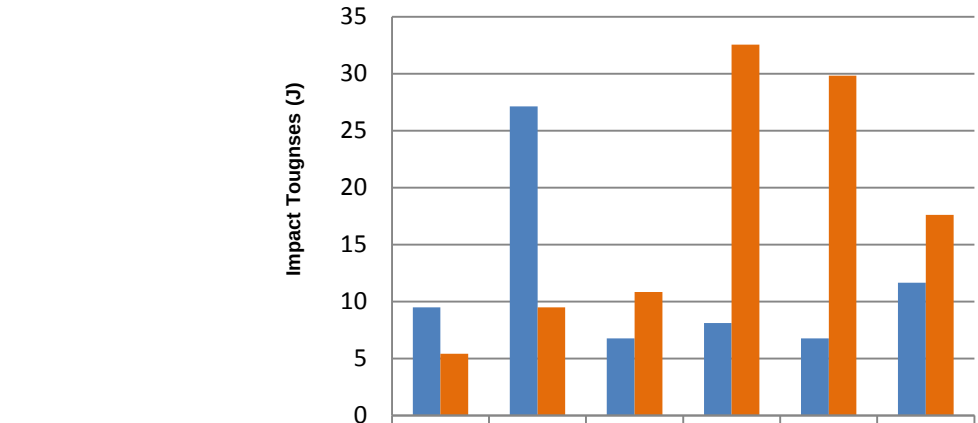

	1	2	3	4	5	Avg
Maraging Charpy V-Notch (70°F)	9	27	7	8	7	12
Maraging Unnotched (70°F)	5	9	11	33	30	18

Figure 45. Charpy impact toughness for the 0-0° electron beam cladded maraging deposit from Company D tested at +70°F.

Three sub-sized (0.250”) tensile bars were taken from the cladded block, and the results are reported in Figure 46. Samples 1 and 3 both experienced extremely brittle fracture (less than 0.5% elongation) with low tensile strength (100 and 70 ksi, respectively) and immeasurable yield strength. An image of the tensile specimens is shown in Figure 47; the brittle fractures occurred near the radius for both samples. Sample 2 exhibited ductile cup-cone fracture (9.5% elongation) and higher tensile (157 ksi) and yield (127 ksi) strength.

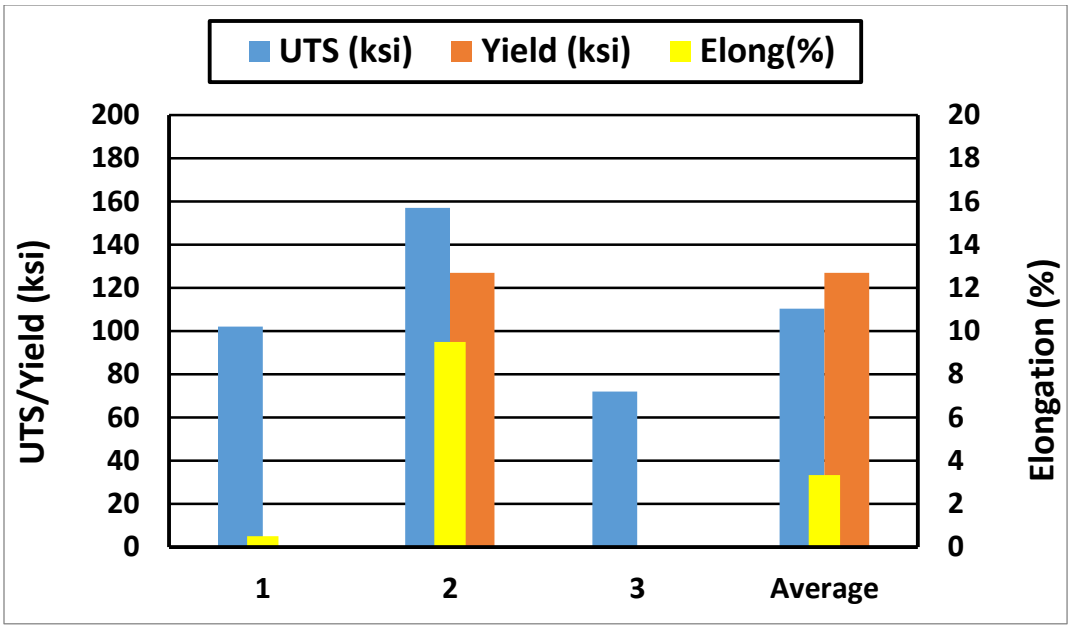

Figure 46. Sub-sized tensile (0.250") results for the 0-0° electron beam cladded maraging steel from Company D.

Figure 47. Image of the tested tensile specimens from the electron beam cladded maraging steel from Company D.

3.4.3. Discussion

The deposition of the electron beam cladded block at Company D spanned two days and took 7 hours and twenty minutes total, excluding the break for the evening. Each

pass took 16 seconds, with each 1.5 mm layer taking 4 minutes. The layers were deposited one at a time. Since the electron beam chamber is evacuated to low vacuum during operation, cooling is controlled solely by conduction through the clamping; as a result, each layer was allowed to cool for 10 minutes between deposits to attempt to mitigate runaway interpass temperatures.

The hardness of the maraging deposit (50-60 HRC) was overhardened compared to the as-received tempered base metal (45 HRC). The HAZ experienced an decrease in hardness compared to the unaffected base metal, with a minimum at 30 HRC, but the base metal in this test was also softened to 35 HRC which is attributed to the base plate being held at an average temperature of 590°C (1100°F) for five hours over the first day of the deposition, which is above the temper softening temperature for H13.

The x-ray showed an extremely large number of indications throughout the bottom three-quarters of the block. The break where the indications steeply drop off appears to be at the break between layers when the cladding was stopped for the evening break. This decrease in porosity on day two may be due to the greater available thermal mass as a result of the previous day's deposited layers, which were allowed to cool overnight; this mass acted as a heat sink, reducing the interpass temperature. The porosity may be due to thermally induced fusion defects or degassing from the wire, though this is unlikely.

The Charpy V-notch average (12 J) was acceptable compared to the base metal results tested on the Company A block (14 J), but the individual results showed a large amount of scatter. Likewise, the unnotched samples had a large individual result scatter

as well. This is explained with the results from the x-ray, as the voids in the sample would cause samples that include them to have very low values, but not all samples would have a pore contained in the fracture path.

The tensile results in Figure 46 also show poor strength and elongation results for two of the three samples, attributed to the porosity. The sample that exhibited ductile cup-cone fracture (at 9.5% elongation) had acceptably high tensile (157 ksi) but lower yield (127 ksi) strength than other processes.

3.5. DMD with Powder – Company E

3.5.1. Description of the method and parameters

The experiments conducted at Company E were conducted on H-13 grade base plates machined to 6.12”x4.50”x0.75”. The base plates were in the tempered (46.5 HRC) state.

The cladding procedure was done with both grade H13 and Maraging powdered steels, provided by Carpenter Powder Products fed at 7.5 g/min. The CO_2 laser was operated at 1.6-1.8kW at a travel speed of 800mm/min (32in/min). The resulting single pass bead was 1.5mm toe-to-toe and 0.7mm high. Subsequent passes had a 1mm step-over.

The deposition program was written to first deposit a single pass around the outside of the block, and then the rest was filled in using the 0-90° deposition pattern, switching between longitudinal and transverse patterns between each layer. Between each layer deposition, the surface of the previous layer was cleaned of oxides.

3.5.2. Experimental Results

With a travel speed of 32 in/min, it took between 6 minutes and 30 seconds and 6 minutes and 40 seconds to deposit each layer. Each entire block took 59 layers to reach 1.5" total height, and was deposited in approximately 8 hours total with 6 hr and 50 min of laser run time.

Block	Total Time
0-90° H13 Tempered Base Plate	7:30
0-90° Maraging Tempered Base Plate	7:52

Table 5. Total deposition times for the two DMD blocks from Company E.

After cladding, the base plates were analyzed in a coordinate measuring machine (CMM) in order to determine the residual distortion for each process. Using the resulting coordinates, surface and centerline maps were used to compare the magnitude of distortion as shown in Figure 48 and Figure 49.

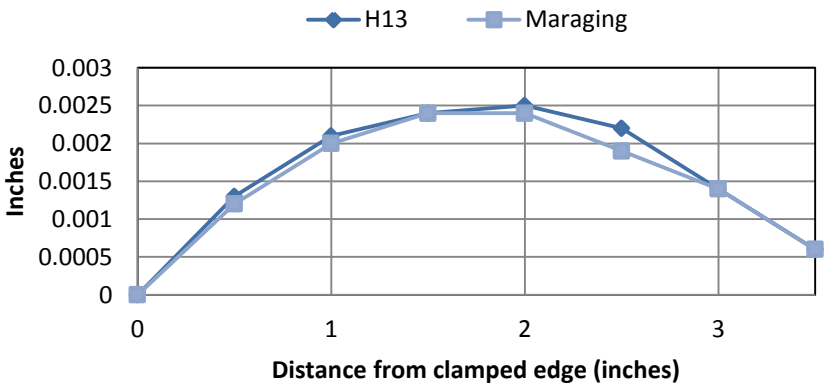

Figure 48. Centerline plots for each plate showing two-dimensional residual distortion.

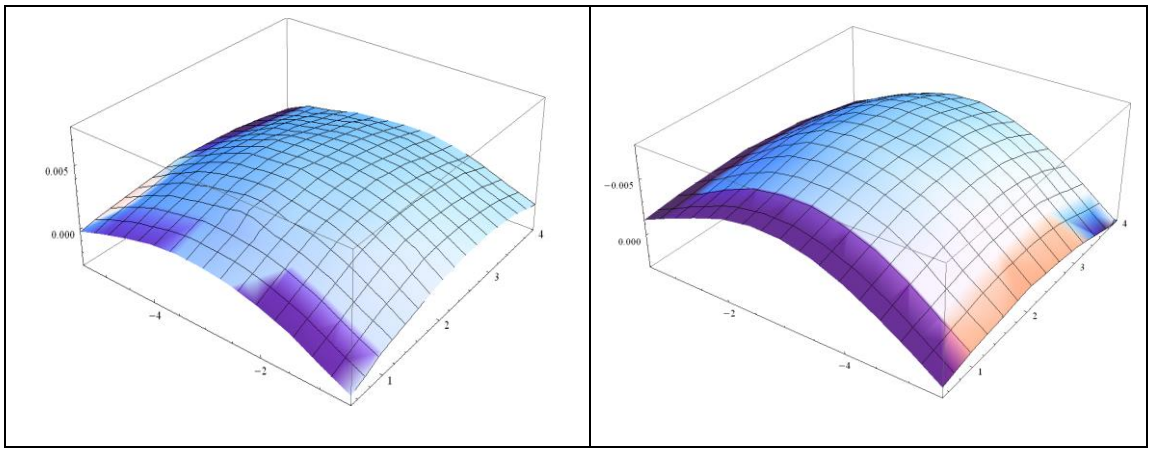

Figure 49. Surface plots for the Company E plates showing three-dimensional residual distortion in the H13 (left) and maraging (right) deposits.

Optical microscopy was also conducted on the base metal-deposit interface. As shown in Figure 50, there is a distinct heat affected zone in the base metal for both the H13 and maraging deposits. The total measured HAZ extends approximately 0.6mm into the base metal from the fusion line. Microhardness measurements taken across the interface on the maraging deposit show an increase in hardness in the HAZ near the fusion line. Inspection of the deposited layers as shown in Figure 7 indicated a cellular and dendritic microstructure.

SEM imaging of the H13 (Figure 53) and maraging (Figure 54) deposits further indicate the presence of a martensitic structure. Additionally, Figure 54 shows a pore near the interface between the base plate and the deposit. Additional fractograpy of the Charpy sample in Figure 55 shows a region of the sample with a high density of pores.

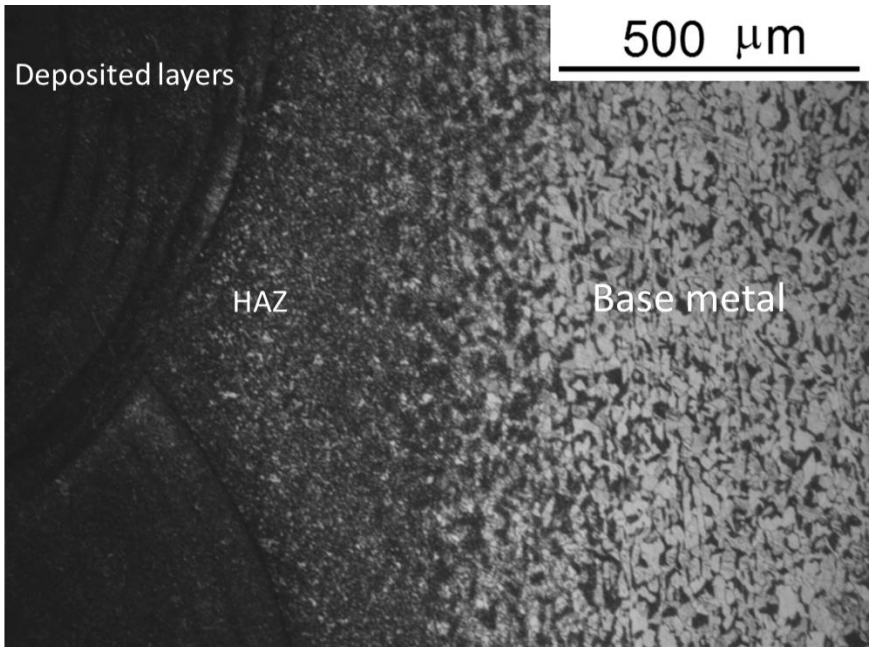

Figure 50. Optical micrograph of 0.5 mm HAZ from Company E H13 deposit on tempered H13 base plate.

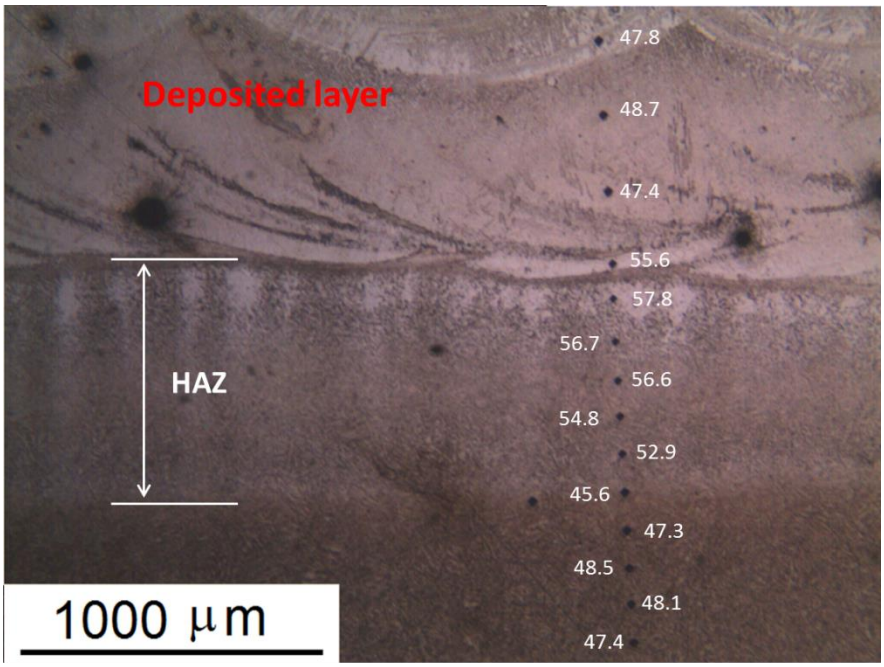

Figure 51. Micrograph of the fusion line between the maraging deposit and H13 base metal from the DMD deposit at Company E.

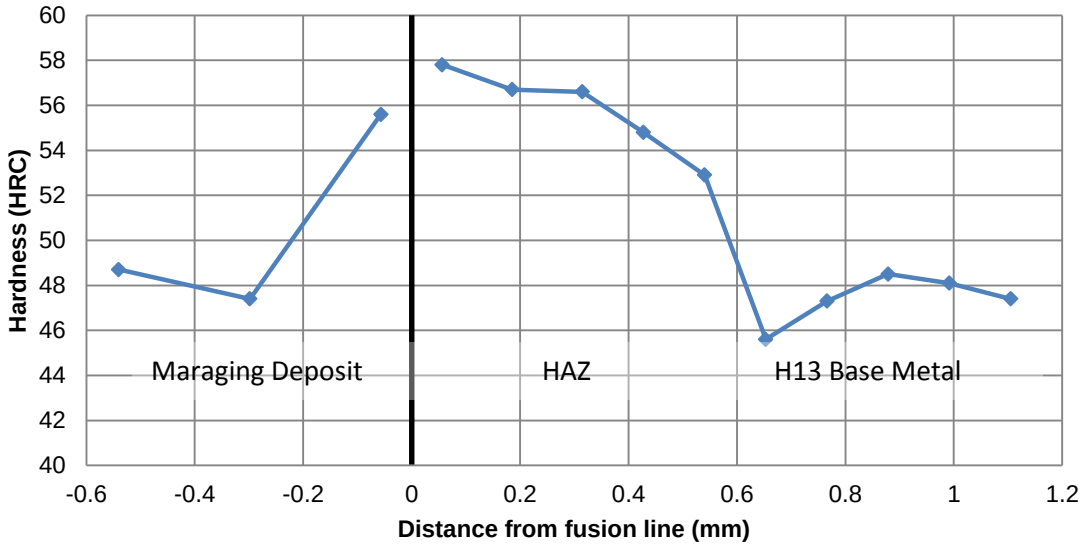

Figure 52. Hardness spanning the interface between the maraging deposit and H13 base metal from the DMD deposit at Company E.

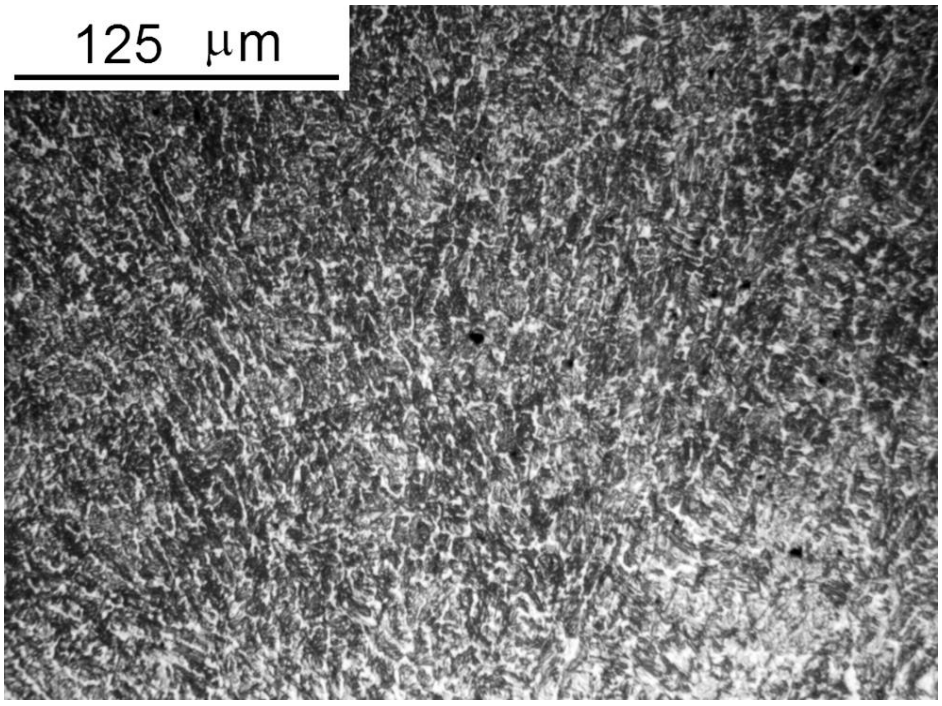

Figure 53. SEM image of Company E H13 deposit showing lath martensitic microstructure.

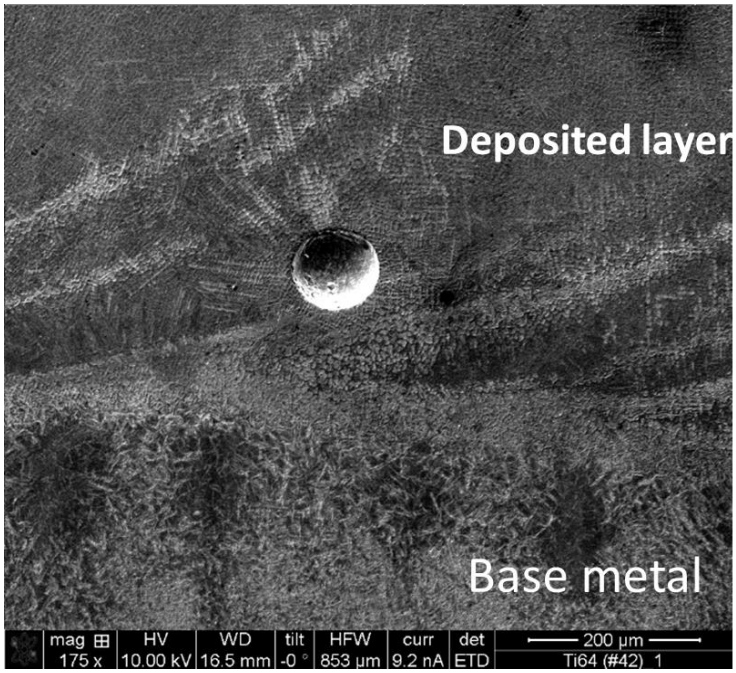

Figure 54. SEM image of Company E maraging deposit showing lath martensitic microstructure. Porosity can be seen in the center of the image.

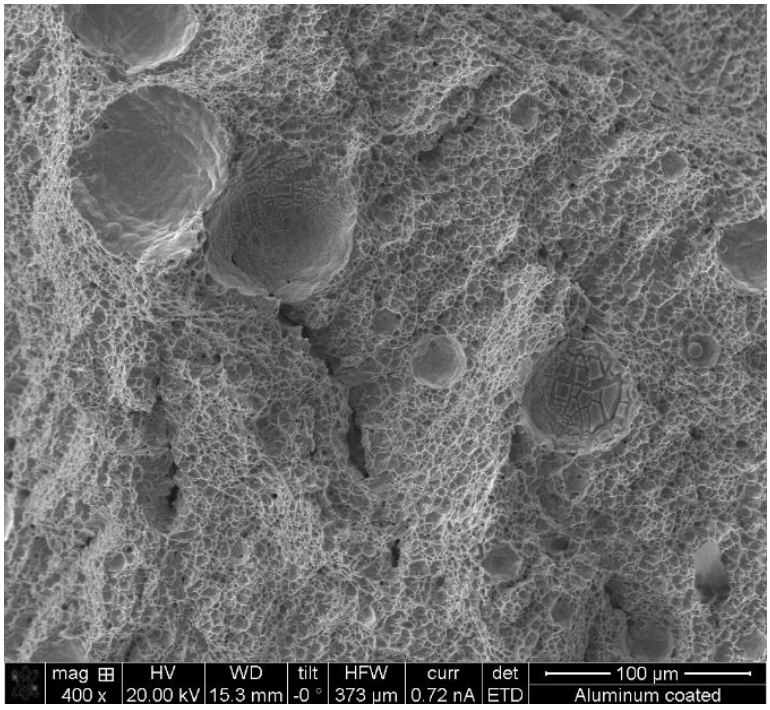

Figure 55. SEM image of Company E Charpy sample. Porosity can be seen throughout the surface.

The Charpy results are shown in Figure 56. The maraging deposit had an average toughness of 22 J (16 ft-lbs), and the H13 was 6 J (4 ft-lbs). In the tempered H13 base plate from Company A the average was 13 J (10 ft-lbs), almost half the toughness from the maraging deposit. The amount of spread in individual test results was lower for the deposit than the base plate, which shows promise for consistent results.

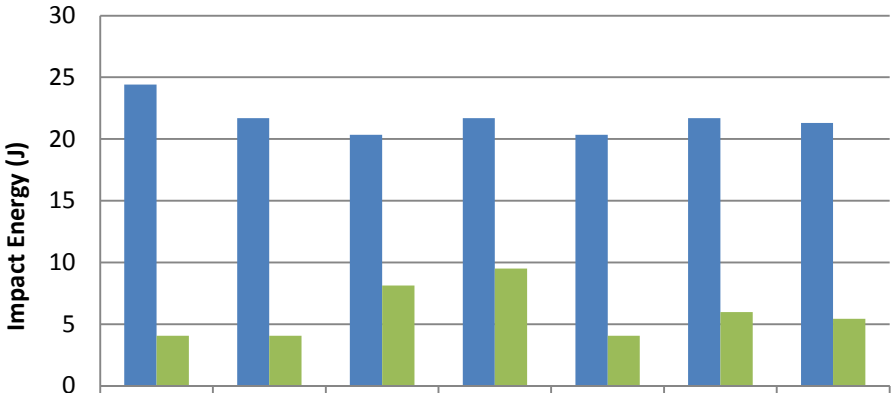

	1	2	3	4	5	Average	Olympic Average
CVN Maraging Deposit (70 F)	24	22	20	22	20	22	21
CVN H13 Deposit (70 F)	4	4	8	9	4	6	5

Figure 56. Comparison of hardness in the base plate, H13, and maraging deposits.

3.5.3. Discussion

The deposition of the Company E blocks took between 7.5 and 8 hours total, with 6 hours and 50 minutes of laser run time. Each pass took 8 seconds, with each 0.7mm layer taking 6 minutes and thirty seconds. The relatively low deposition rate of powder-based deposition processes increases the time required compared to the wire-based processes.

The distortion was very minimal for this geometry. Both plates deflected no more than 0.005", less than 1% of the plate dimensions. This is an encouraging result, as distortion is an analogous test to residual stress which can cause cracking and failure. The maximum distortion in the plate was near the geometric center, and was 0.0030" for the H13 and 0.0024" in the maraging plate. Other geometries may be more susceptible to distortion and residual stress than our test geometry, and distortion and residual stresses should continue to be a consideration and key design factor.

The hardness of the maraging deposit matched the tempered base metal very well, at 46-48 HRC. The HAZ experienced an increase in hardness compared to the unaffected base metal, nearing 58 HRC at its peak. This amount of over hardening may make it susceptible to cracking in service.

The Charpy V-notch results were drastically different between the H13 and maraging deposits. The 22 J (16 ft-lbs) achieved by the maraging was the higher than that of the base plate's 13 J (10 ft-lbs) and much higher than the H13's 6 J (4 ft-lbs). The narrow scattering for each deposit are a good sign of reliable testing and values. However, fractograpy of the maraging sample, shown in Figure 55, indicated a high density of porosity in some regions.

3.6. DMD with Powder – Company F

3.6.1. Description of the method and parameters

The experiments conducted at Company F were conducted on H-13 grade base plates machined to 6.12”x4.50”x0.75”. The base plate was in the tempered (46.5 HRC) state.

The cladding procedure was done with powdered maraging steel, provided by Carpenter Powder Products fed at 11 g/min. The molten bead pool was shielded using commercially pure argon gas, which was also fed through the powder feed head. The CO_2 laser was operated at 3 kW at a travel speed of 800 mm/min (32 in/min). The resulting single pass bead was 7.2mm toe-to-toe and 1mm high. The deposition was made using the 0-90° deposition pattern, switching between longitudinal and transverse patterns between each layer.

3.6.2. Experimental Results

The deposition of maraging steel at Company F took 7 hours and 18 minutes total. Each pass took 15 seconds, and each layer took 4 minutes. The layers were deposited six layers are a time, and after the sixth layer the block was allowed to air cool for 45 minutes to mitigate runaway interpass temperature.

Block	Total Time
0-90° Maraging	7:18

Table 6. Total deposition time for the DMD block from Company F.

The cross-sectional optical micrographs shown in Figure 57 and Figure 58 feature bi-directional bead length tracks. The black spots are artifacts of the etching and polishing process. The microstructure shows cellular, dendritic morphology and epitaxial growth. Intercellular spacing is approximately 15 µm.

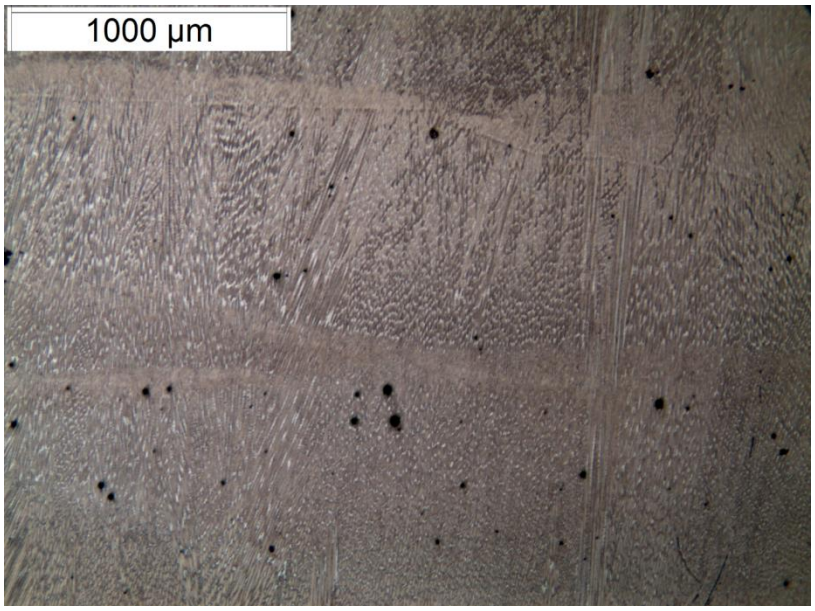

Figure 57. Microstructure of DMD maraging deposit from Company F.

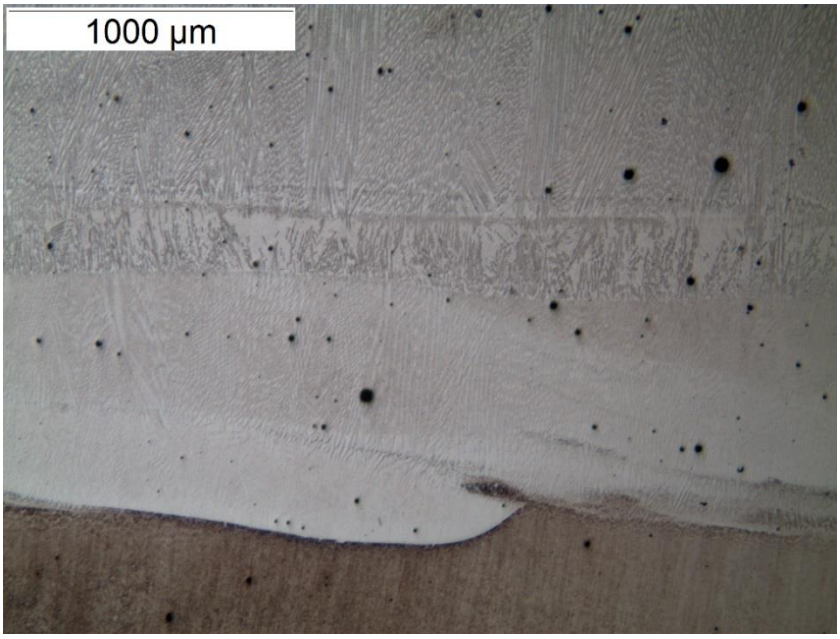

Figure 58. Microstructure of the interface between the H13 base metal and DMD maraging deposit from Company F.

The heat-affected zone, shown in Figure 59 extends 1.8mm into the base metal. The microhardness measurements taken across the interface show that the HAZ experienced an increase in hardness near the fusion line when compared to the unaffected base metal.

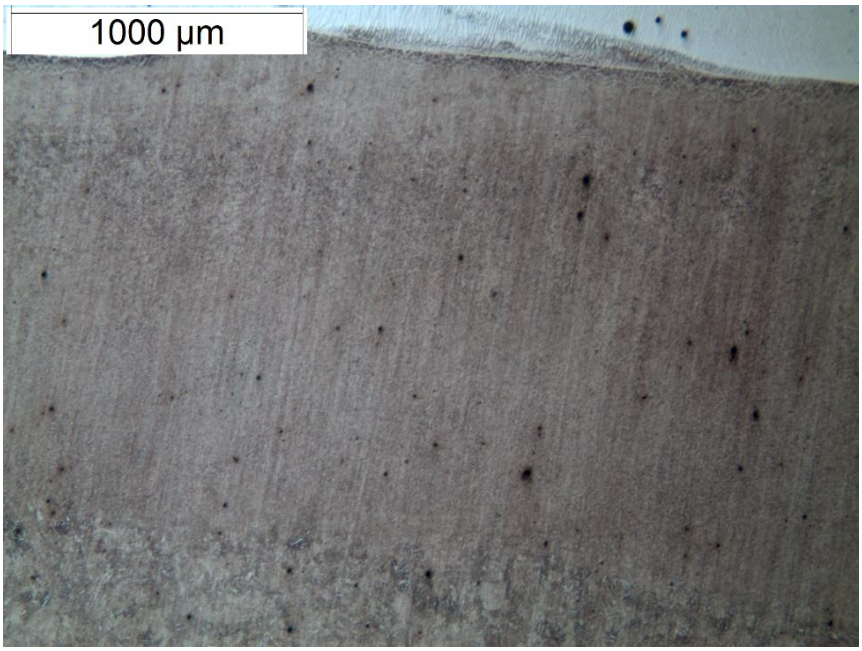

Figure 59. HAZ microstructure in the DMD maraging deposit from Company F.

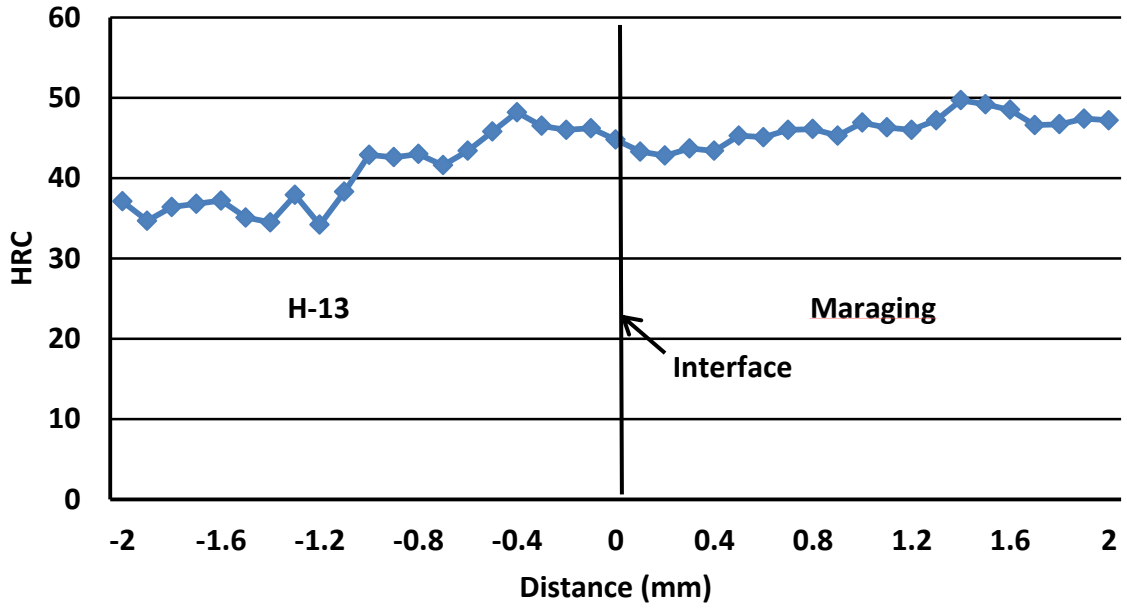

Figure 60. Microhardness measurements spanning the interface between the maraging deposit and H13 base metal from Company F.

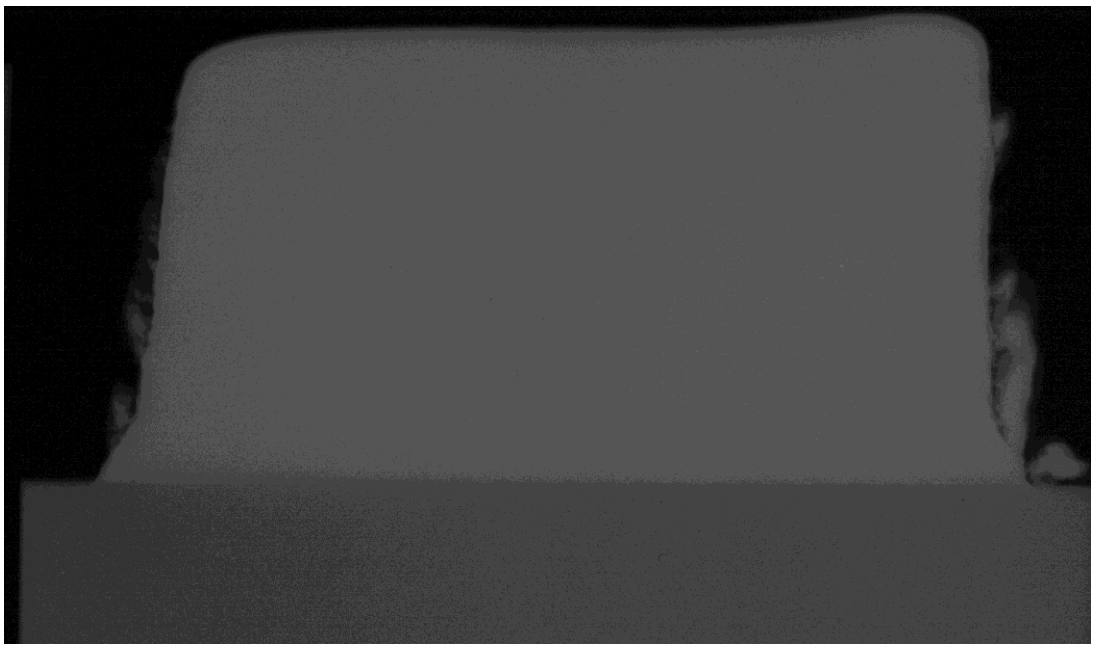

Figure 61. X-ray of a section of the maraging deposit from Company F, showing no relevant indications.

An x-ray of the maraging deposit, shown in Figure 61, shows no relevant indications of porosity, inclusions, or lack of fusion in the deposit, which was also supported by the microscopy. The indications on the side of the block are the result of irregularities in the deposit surface, visible in Figure 62.

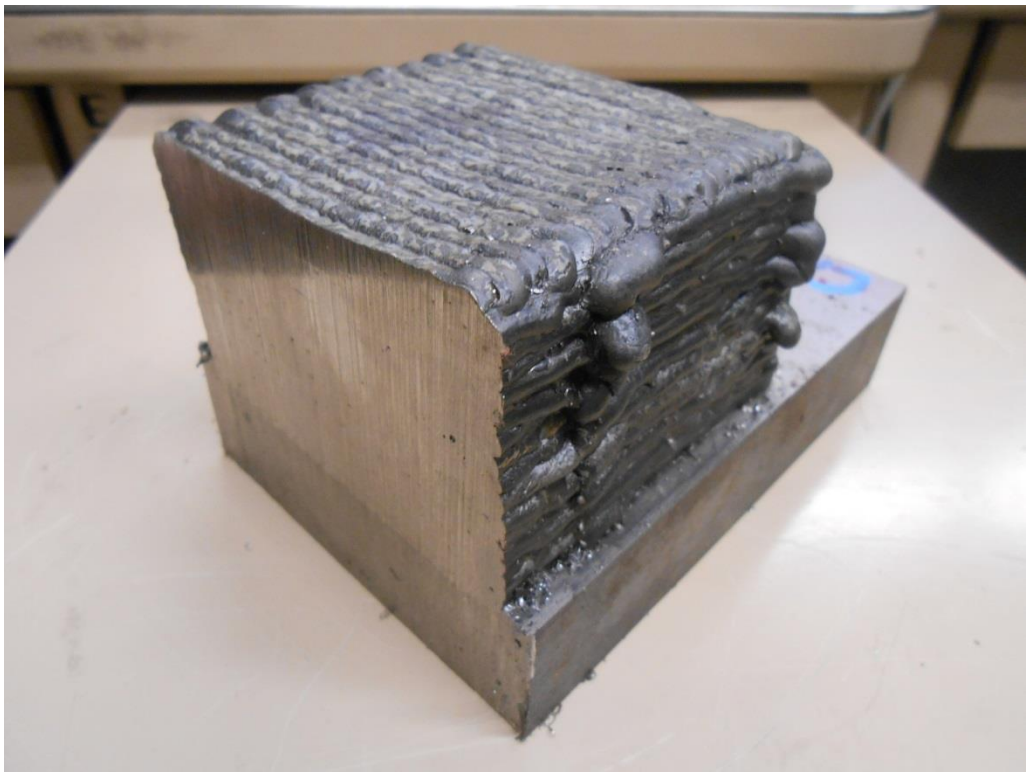

Figure 62. Image of the DMD block from Company F.

The maraging block was sectioned for three sub-sized tensile bars and five Charpy v-notch and unnotched impact specimens. The tensile results in Figure 63 show consistently good yield strength (1048 MPa, 152 ksi average) and ultimate tensile strength (1172 MPa, 170 ksi average), but lower elongation (9% average). All three tensile specimens broke near the midpoint of the bar and showed cup-cone type fracture.

The full-sized Charpy impact specimens were broken at 21°C (70°F) and ranged from 14 J (10 ft-lbs) to 24 J (18 ft-lbs), with an average of 19 J (14 ft-lbs). The half-sized unnotched impact specimens were also tested at 21°C (70°F) and ranged from 31 J (23 ft-lbs) to 61 J (45 ft-lbs), with an average of 54 J (40 ft-lbs). The individual and average results for both tests are shown in Figure 64.

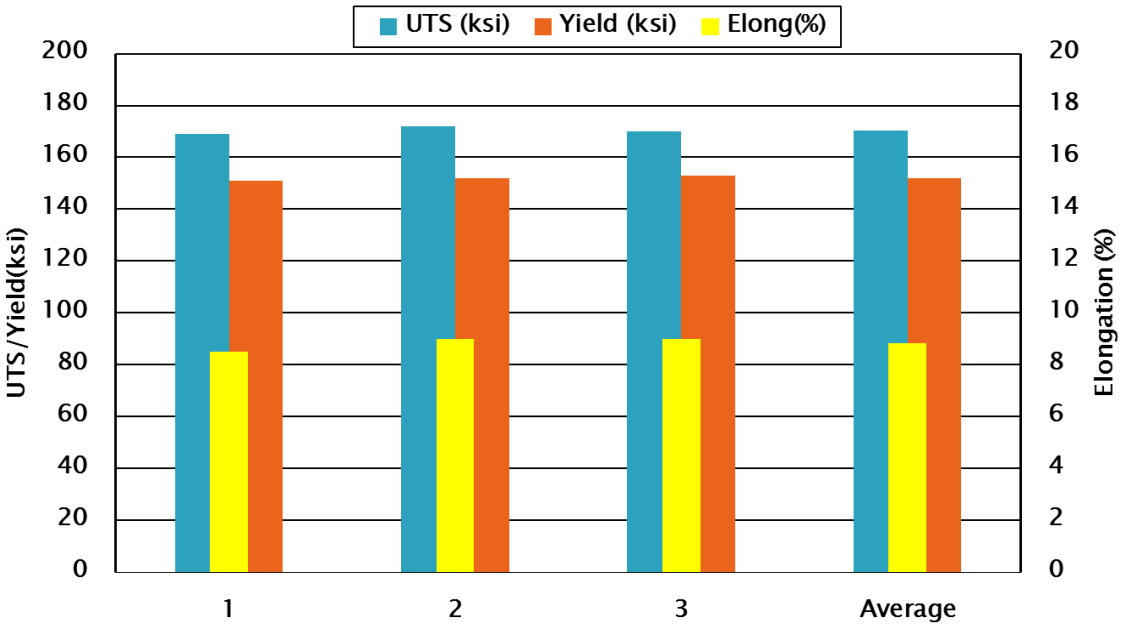

Figure 63. Sub-sized tensile (0.250") properties from the maraging deposit from Company F.

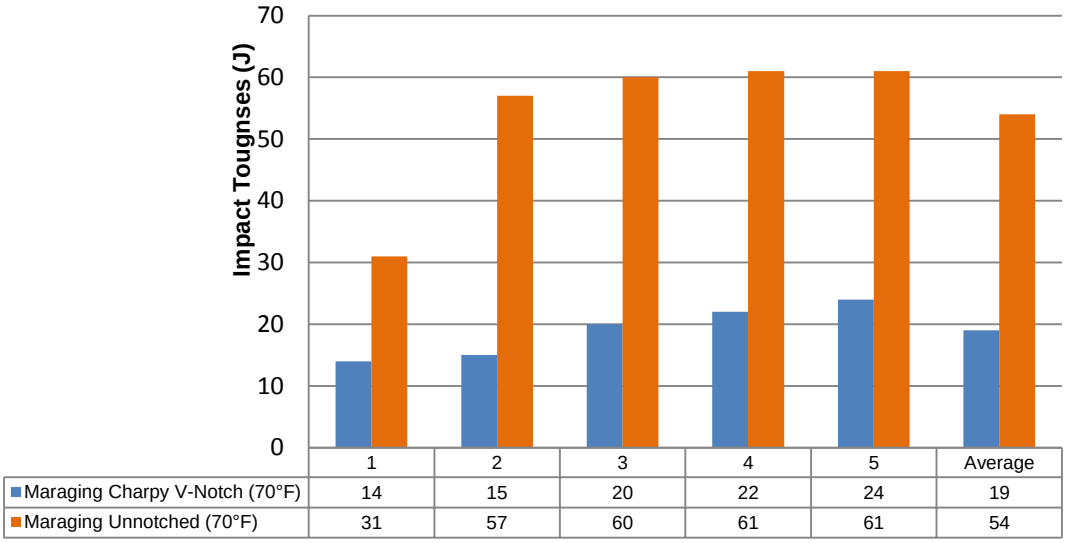

	1	2	3	4	5	Average
Maraging Charpy V-Notch (70°F)	14	15	20	22	24	19
Maraging Unnotched (70°F)	31	57	60	61	61	54

Figure 64. Charpy and unnotched impact toughness for the maraging deposit from Company F.

3.6.3. Discussion

The deposition of the blocks at Company F took between 7 and 7.5 hours total, with 2 hours and 48 minutes of laser run time. Each pass took 15 seconds, with each 1 mm layer taking 4 minutes. The relatively small bead size of powder-based deposition processes increases the time required compared to the wire-based processes.

The hardness of the maraging deposit matched the tempered base metal well, at 43-49 HRC. The HAZ experienced an increase in hardness compared to the unaffected base metal, peaking at 48 HRC, but the base metal in this test was a softer temper (35 HRC) so the hardened HAZ matched the deposit hardness well.

The Charpy V-notch average (19 J) was acceptable compared to the base metal results tested on the Company A block (14 J). The unnotched samples were consistently reported between 55 and 60 J, with the exception of Sample 1 at 30 J. The narrow

scattering for the Charpy and unnotched impact samples is a good sign of reliable deposition with few deleterious inclusions or porosity. The x-ray results and consistency among tensile specimens and their cup-cone type fracture also supports this.

3.7. Laser Engineered Net Shape® – Company G Laboratory

3.7.1. Description of the method and parameters

The experiments conducted at Company G Laboratory were conducted on H13 base plates machined to 6.12”x4.50”x0.75”. The base plates were in the tempered (46.5 HRC) state.

The cladding procedure was done with maraging powdered steel from Carpenter Powder Products fed at 5.1 g/min. The IPG Ytterbium Fiber Laser was operated at 1064 nm and 950 W with a 2mm spot size.

The deposition program was written to fill using the 0-90° deposition pattern, switching between longitudinal and transverse patterns between each layer. The step-over between passes was 0.040” and each layer was 0.020” high.

3.7.2. Experimental Results

The deposition of maraging steel at Company G required 16 hours and 54 minutes of laser run time, and the entire process took 21 hours and 11 minutes.

Block	Total Time
0-90° Maraging	21:11

Table 7. Deposition times for LENS® at Company G.

The cross-sectional optical micrographs shown in Figure 65 and Figure 67 feature bi-directional bead length tracks (into and across the cross-sectional plane) and spherical porosity (black spots) ranging from 15 to 120 µm. Closer inspection of the microstructure in Figure 66 and Figure 68 show cellular, dendritic morphology and epitaxial growth. Intercellular spacing is measured to be approximately 7.5 µm.

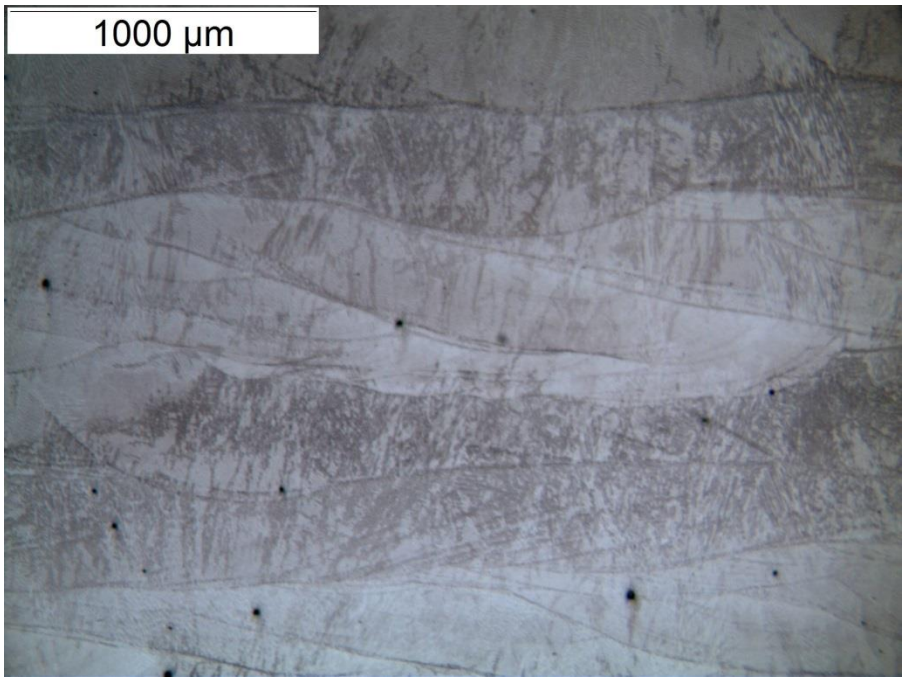

Figure 65. Microstructure of the LENS® maraging deposition from Company G Labs showing bi-direction passes across and into the cross-sectional plane.

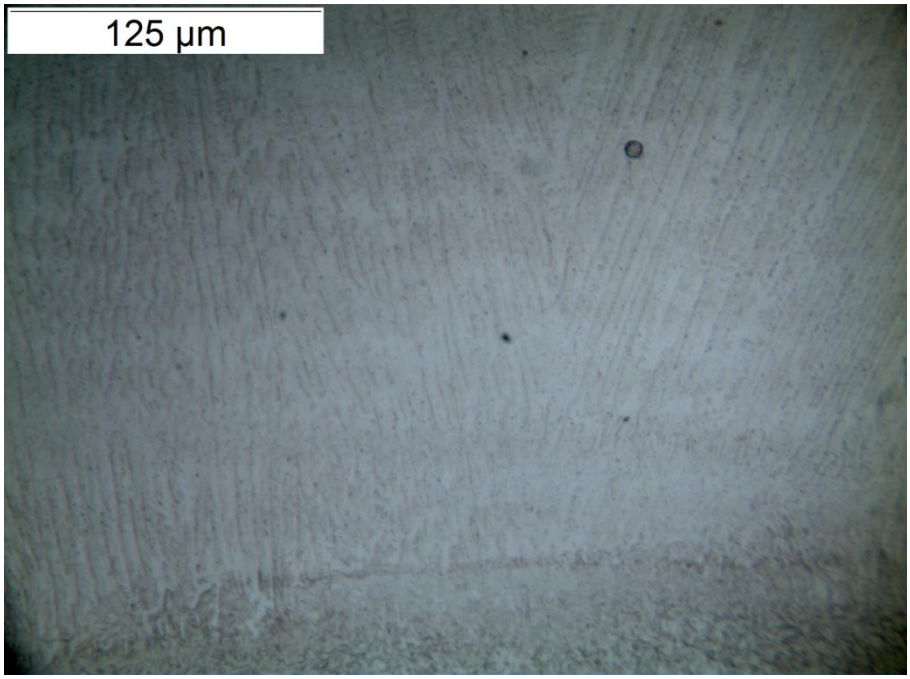

Figure 66. Microstructure of the LENS® maraging deposition from Company G Labs.

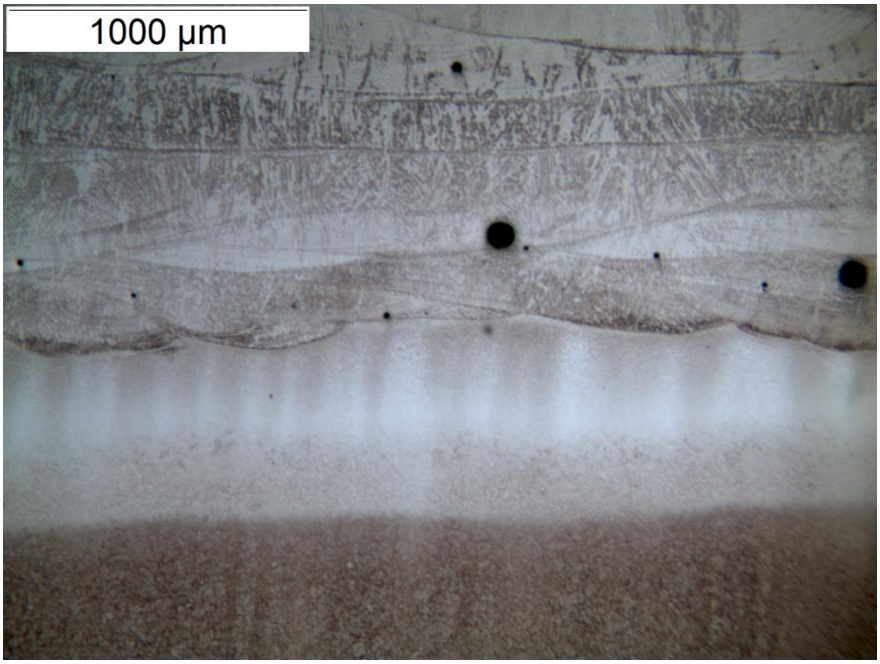

Figure 67. Micrograph of the interface between the LENS® maraging deposit and H13 base metal from Company G.

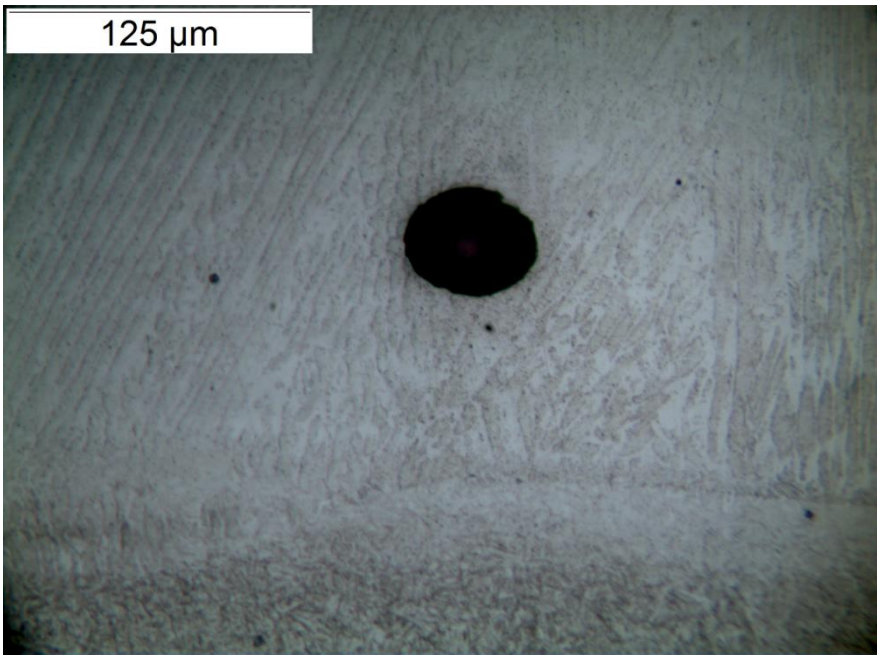

Figure 68. Micrograph of an instance of porosity near the fusion line in the LENS® deposit from Company G.

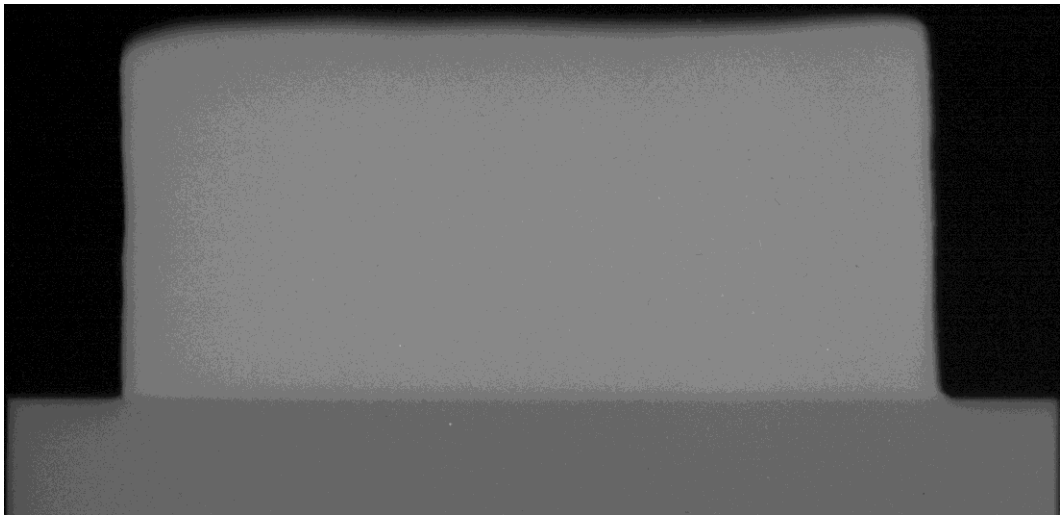

Figure 69. X-ray of the LENS® maraging deposition from Company G.

An x-ray of a section of the LENS® deposit is shown in Figure 69; there are no clear, relevant indications at the resolution of the x-ray sensitive film. It is also interesting to

note the sharp lines at the edges of the block in the x-ray, highlighting the process' fine dimensional control.

The heat-affected zone is captured in Figure 70 extending 0.6 mm into the base metal. Microhardness measurements were taken across the interface indicating that the HAZ experienced an increase in hardness near the fusion line (peaking at 58 HRC), followed by a shorter region of temper softening (lowest value at 40 HRC) before returning to the hardness of the unaffected base metal.

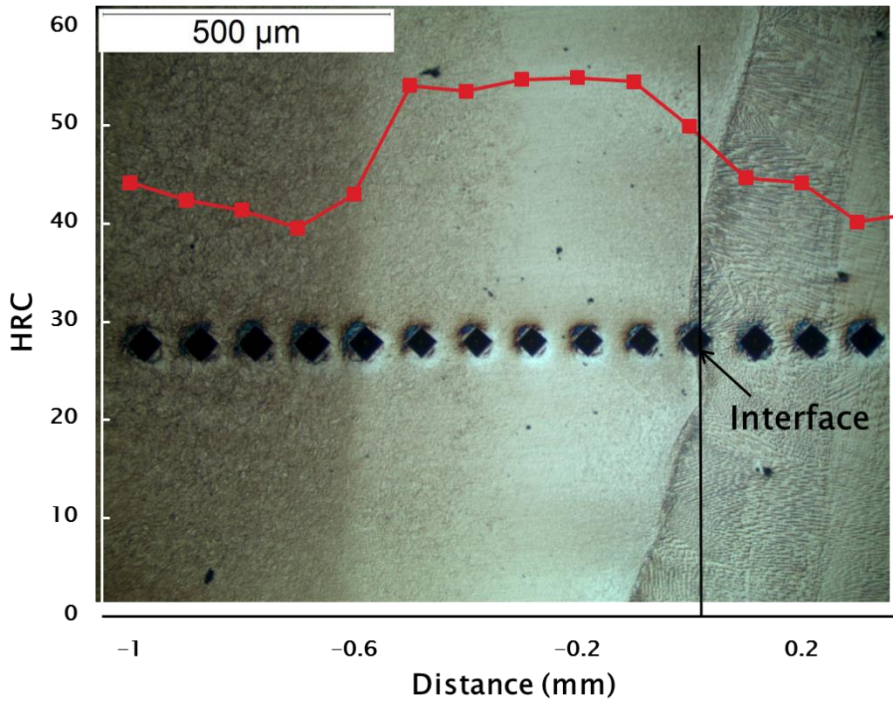

Figure 70. Microhardness measurements spanning the base metal (left), HAZ (center), and deposit (right) for LENS® maraging steel deposit at Company G.

The maraging block was sectioned for three sub-sized (0.250") tensile bars as well as five of both Charpy v-notch and unnotched impact specimens. The tensile results in

Figure 71 have inconsistent results. The yield strength (154 ksi average) and ultimate tensile strength (162 ksi average) are high, but low elongation (7.7% average). Specimens 2 and 3 had consistent tensile properties, though they broke off-center; however, the consistency of those specimens is broken by the brittle behavior of specimen 1 (1% elongation) which broke near the radius.

The full-sized Charpy impact specimens were broken at 21°C (70°F) and ranged from 20 J (15 ft-lbs) to 30 J (22 ft-lbs), with an average of 25 J (19 ft-lbs). The half-sized unnotched impact specimens were also tested at 21°C (70°F) and ranged from 45 J (33 ft-lbs) to 61 J (45 ft-lbs), with an average of 54 J (40 ft-lbs). The individual and average results for both tests are shown in Figure 73.

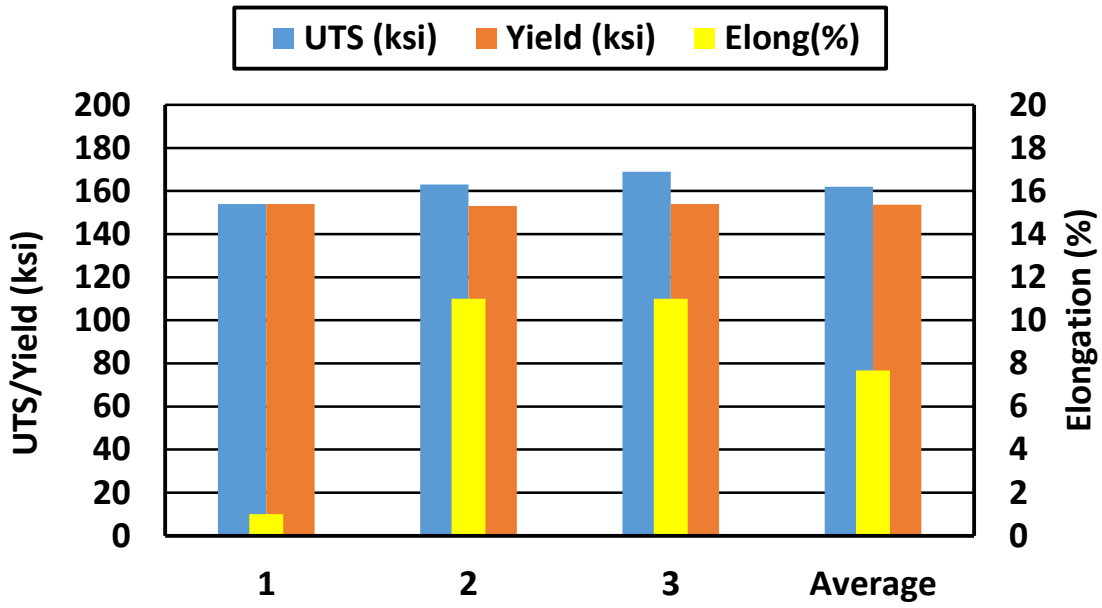

Figure 71. Sub-sized tensile (0.250") properties from the LENS® maraging deposit from Company G.

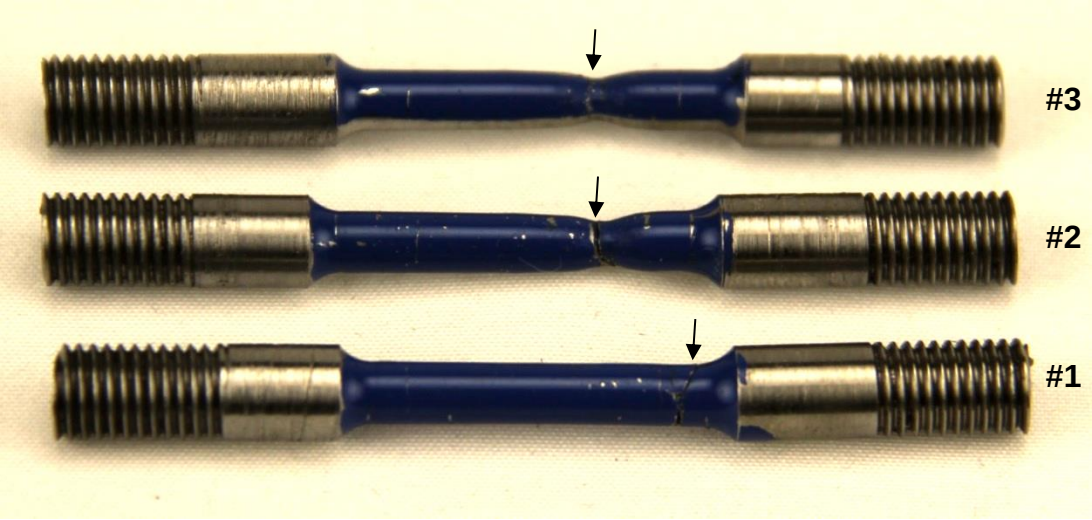

Figure 72. Sub-sized tensile specimen taken from the LENS® deposited maraging steel at Company G.

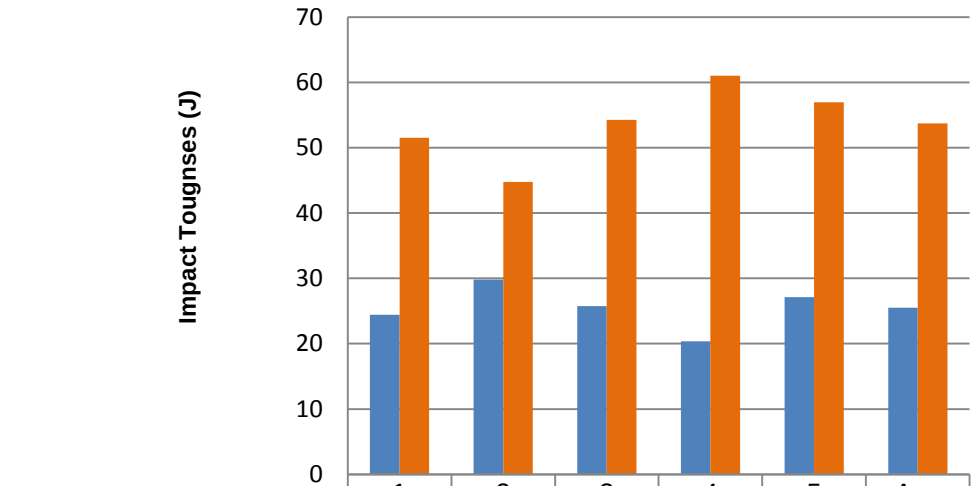

	1	2	3	4	5	Avg
Maraging Charpy V-Notch (70°F)	24	30	26	20	27	25
Maraging Unnotched (70°F)	52	45	54	61	57	54

Figure 73. Impact toughness for full-sized Charpy V-notch and half-sized unnotched impact specimens taken from the LENS® maraging deposit from Company G and tested at +70°F.

3.7.3. Discussion

The deposition of the LENS® -cladded blocks at Company G took 21 hours to complete, with nearly 17 hours of laser run time, which is the longest of the tested processes. The LENS and other blown powder processes are limited to much lower deposition rates than the wire processes, which can deposit upwards of 10 pounds per hour.

The hardness of the maraging deposit slightly under matched the as-received base metal at 40-44 HRC. The HAZ experienced an increase in hardness compared to the unaffected base metal, peaking at 55 HRC, then temper softening for a shorter region before reaching the unaffected base metal. The hardening in the HAZ (up to 55 HRC) may increase crack susceptibility in use.

The Charpy V-notch average (25 J) was good compared to the base metal results tested on the Company A block (14 J). The unnotched samples were varying between 45 and 61 J. The variance in Charpy and unnotched impact samples, along with the brittle fracture in tensile specimen 1 show signs of deleterious defects in the deposit. This is supported by the micrographs which show significant porosity despite a clean x-ray. The absence of indications in the x-rays, despite observations of pores in the cross-sections, may indicate that the observed voids were actually a result of pull-out of unmelted powder in the deposit. Despite the brittle fracture of specimen 1, the strength of the tensile specimens was good for all three samples.

Chapter 5: Summary, Comparisons, and Conclusions

5.1. Deposit Structure

The weld deposit for all of the deposition processes showed similar microstructures, but varied in feature size. Typical of most weld metals, the microstructure in the depositions were combined dendritic and cellular. Additionally, the deposits showed heat affected zones of different sizes and tempers, with an overall average HAZ length of 0.9mm. The largest measured heat affected zone (based on microstructure and microhardness) was from the DMD process at Company F at 1.8mm, while the smallest was the LHW process at Company B at 0.4mm. Most of the deposits maintained their original temper of 44-46 HRC in the unaffected base metal, but the higher interpass of the EBF3/Company D deposit caused base metal softening to 30 HRC due to the vacuum chamber (required for electron beam operation, but eliminating convective cooling) which resulted in an average interpass temperature of 590°C (1100°F) for five hours over the first day of the deposition, which is above the temper softening temperature for H13.

Process	Location	Length of HAZ (mm)
Laser Hot Wire	Company A	1.2
Laser Hot Wire	Company B	0.4
GMAW	Company C	1.6
Electron Beam	Company D	All
DMD	Company E	0.6
DMD	Company F	1.8
LENS®	Company G	0.5

Table 8. Comparison of heat affected zone length extending into the H13 base metal. The electron beam deposition had a significant softening effect on the entire base plate.

A summary of each process' deposition time is provided in Table 9. The results of a process were averaged if more than one vendor provided samples or multiple samples from a single vendor. Though the upside of the repair process is very high compared to the machining of a new die, customers in the die casting industry are still price-sensitive to these costs. Overhead and labor for general machining costs can be fifty dollars per hour, or more, so the reductions in deposition time when using the GMAW process could mean a cost reduction of nearly a thousand dollars for this test geometry, assuming equal material costs for the wire and powder. When balancing the reduced deposition time with mechanical properties and deposit quality, in many cases it may be beneficial to move towards the other more mechanically sound processes, and for small geometries the differences in deposition time will also be lower.

Process	Avg Total Time (hr:min)
Laser Hot Wire	5:00
GMAW	1:53
Electron Beam	7:20
DMD	7:40
LENS®	21:00

Table 9. Process comparison of average deposition time for the test geometry

Fractograpy of some of the samples had indications of porosity and inclusions. The x-ray images shown in Figure 74 highlight the indications in a cross section of each block. There were no relevant indications at the resolution of the x-ray film for the LENS® /Company G or DMD/Company F deposits, while the LHW deposit from Company A had small, scattered round indications near the deposit edges which are interpreted as porosity and the LHW deposit from Company B had a cluster of oblong,

irregular low density indications which are interpreted as trapped oxide inclusions which weren't properly removed between layer deposits. The EBF3/Company D and GMAW/Company C deposits both had significant scattered, low-density round indications, interpreted as porosity.

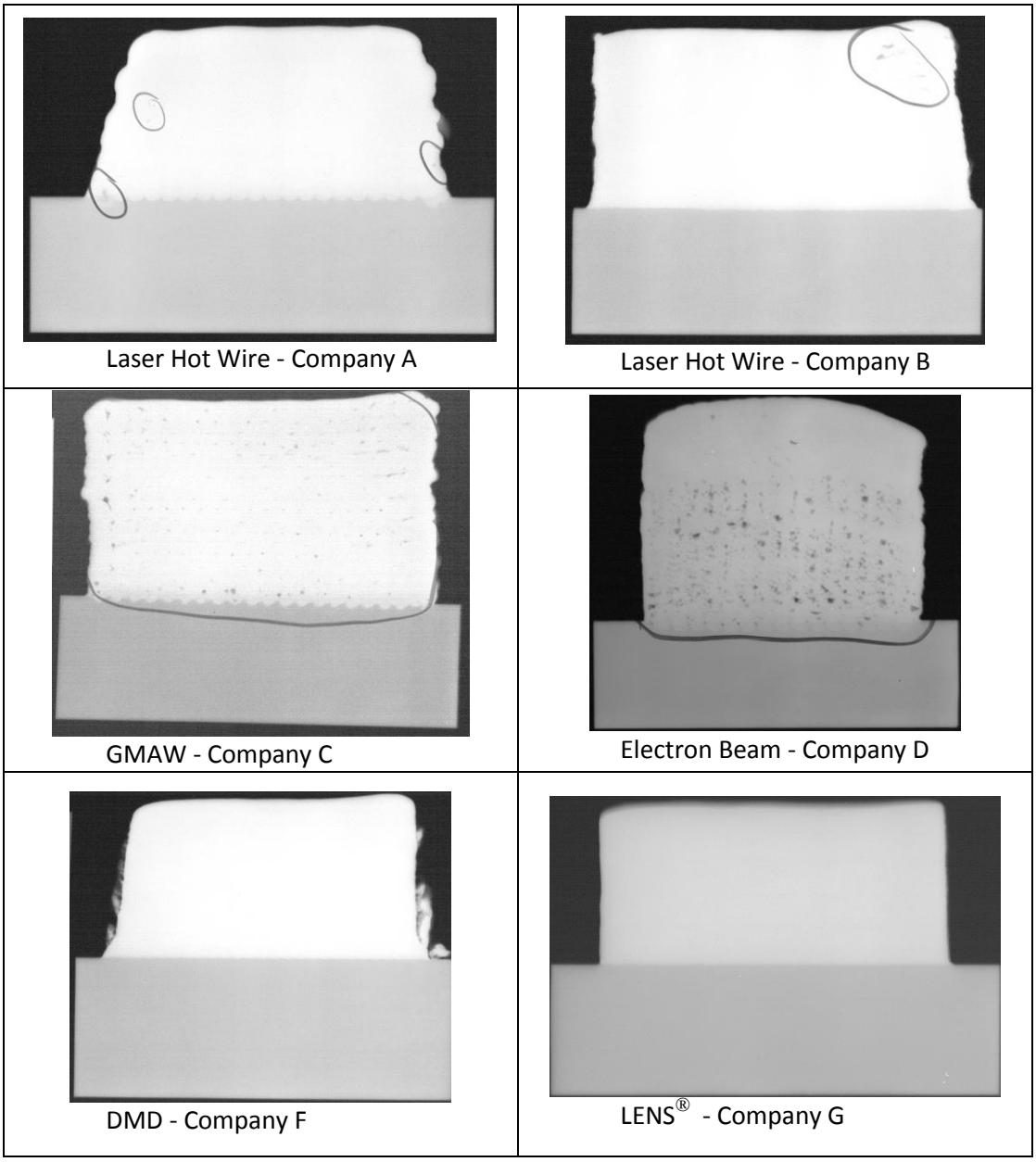

Figure 74. X-ray images of depositions. Areas where indications are located are circled.

There were signs of unmelted particles in the deposit for the LENS deposition, since the x-ray did not show indications of density variation but the cross-sectioning and microscopy did find spherical voids. This is a known issue with powder-based additive manufacturing techniques that is typically able to be overcome through operability studies. The porosity seen in the EBF3 deposit is not atypical for the process, and may be due to nitrogen or oxygen coming out of solution in the melt pool as a result of the low vacuum pressure, or from surface lubricants or arc stabilizers on the wire that are typical of GMAW wires, but not optimized for non-arcing processes. There are wires available for orbital TIG applications commercially which do not have these surface lubricants, but the selection is considerably lower than in GMAW.

It is also interesting to note the deposition profile for each block in the x-ray images. The LENS® deposit was able to build very steep walls with a relatively fine surface roughness, while some of the other blocks had rougher edges or relied on tapered sides for stability during deposition. However, for the application of these processes to die casting tooling repair the die surface will almost invariably require machining after deposition to attain the surface tolerances required, so the dimensional resolution may not be as much of a benefit for most of repairs.

5.1.1. Distortion

After cladding, the base plates from Company A and Company E were analyzed in a coordinate measuring machine (CMM) in order to determine the residual distortion for

each process. Using the resulting coordinates, surface and centerline maps were used to compare the magnitude of distortion shown in Figure 75.

The data collected from the CMM showed that there was very little residual distortion in the plates after deposition. The most extreme case of distortion was 0.06" out-of-plane at its maximum, which is two orders of magnitude lower than the dimensions of the plate when depositing H13 on the annealed H13 base plate. When the same wire was used on the tempered H13 plate, which is the condition most dies are in, the distortion dropped to 0.01" at its maximum. These are promising results that the repair process will not result in considerable distortion or residual stresses resulting from the constraint of the deposit. This will still be an active area of research as additional processes are analyzed, however, as some geometries will be more susceptible to distortion and could have negative effects from even small amounts of residual stresses, such as these.

The differences in distortion between the H13 and maraging deposits on annealed plates in Figure 75 highlights the effect of the pattern on residual stresses. On the tempered plates, it can be seen that the deposit composition (H13 vs maraging) does not have a pronounced effect on distortion. On the annealed plates, however, the H13 was deposited in the 0°-0° pattern, while the maraging was deposited in a 0°-90° pattern. The distortion was measurably reduced in the maraging sample as a result, so the 0°-90° deposition pattern is preferred to minimize the distortion. Additionally, it may improve mechanical properties by introducing variance to break up any weak planes that could align between layers deposited in the same direction, such as stacking of lack-of-fusion defects running along the length of the bead.

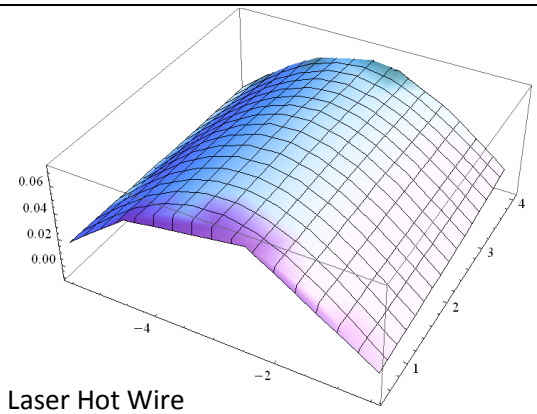

Laser Hot Wire
15 HRC Base Plate
H13 Deposit, 0-0 Pattern

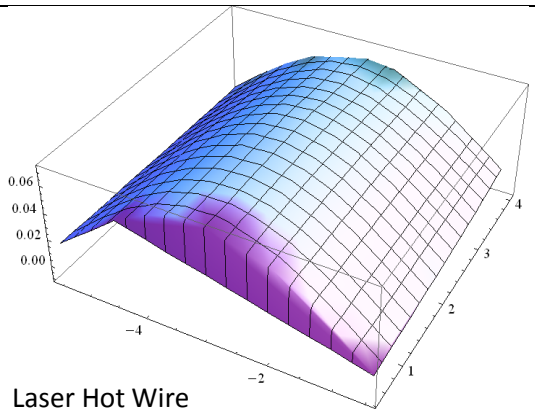

Laser Hot Wire
15 HRC Base Plate
Maraging Deposit, 0-90 Pattern

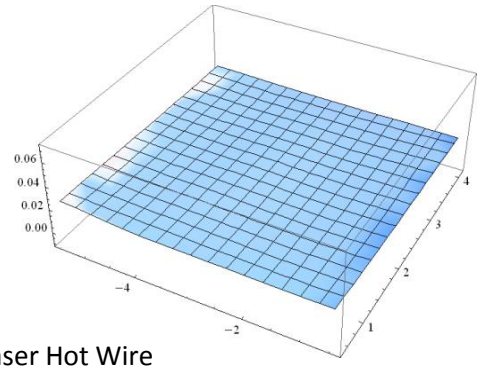

Laser Hot Wire
45 HRC Base Plate
Maraging Deposit, 0-90 Pattern

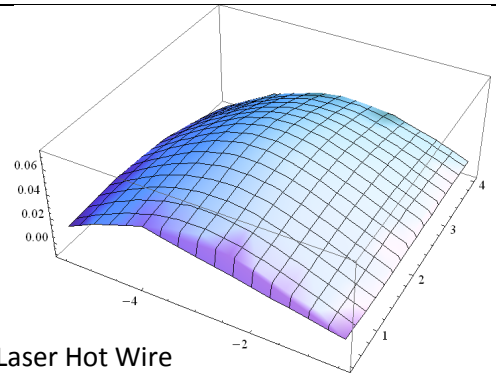

Laser Hot Wire
45 HRC Base Plate
H13 Deposit, 0-90 Pattern

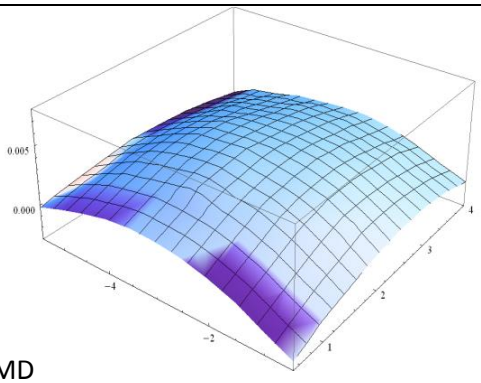

DMD
45 HRC Base Plate
H13 Deposit, 0-90 Pattern

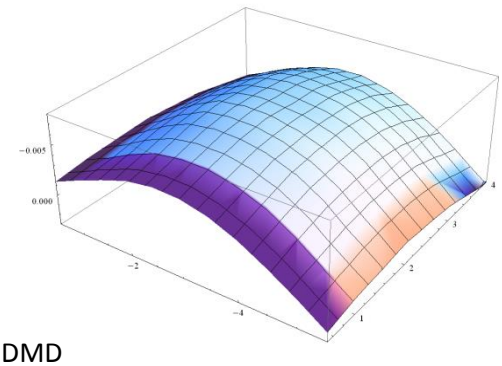

DMD
45 HRC Base Plate
H13 Deposit, 0-90 Pattern

Figure 75. 3-D surface plots from four LHW deposits from Company A and two DMD deposits from Company E.

5.2. Mechanical Properties

5.2.1. Tensile Tests

The tensile tests were conducted on sub-sized tensile bars per ASTM A370-12a. The results, taken from the average of three tests, are presented in Figure 76.

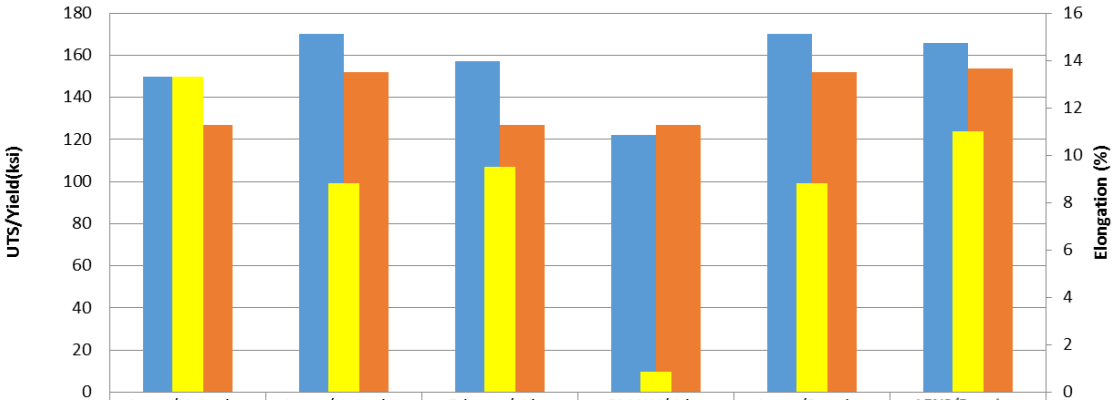

	Laser/Hot-wire Company A	Laser/Hot-wire Company B	E-beam/Wire Company C	GMAW/Wire Company D	Laser/Powder Company F	LENS/Powder Company G
UTS (ksi)	150	170.0	157	122	170	166.0
Yield (ksi)	127	152.0	127	127	152	153.5
Elong(%)	13.3	8.8	9.5	0.88	8.8	11

Figure 76. Average tensile properties for deposition processes.

The obvious outlier is the GMAW process, which had significantly lower elongation and tensile strength than the other processes. This decrease in strength is attributed to the porosity present in the deposition (seen in the x-ray in Figure 74). The test shown for the electron beam deposit is the single test with reasonable elongation (excluding the two with brittle fractures) since their fracture is attributed to the defects seen in the x-ray, so presumably this same is more representative of the mechanical properties if the deposit was sound. For the other processes, the ultimate tensile strength typically between 1034-1172 MPa (150-170 ksi) and the yield strength was between 876-1062 MPa (127-154 ksi). The elongations of the tensile bars at rupture were between 8-14%.

5.2.2. Impact Toughness

Specimens for impact toughness at room temperature were machined for both full-sized Charpy v-notch and sub-sized unnotched testing; the results are presented in Figure 77.

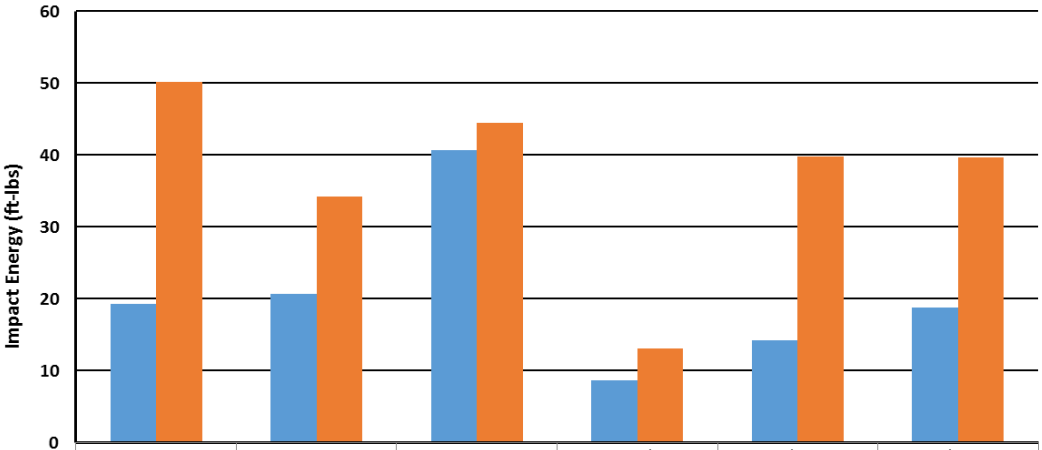

	Laser hot wire Company A	Laser hot wire Company B	GMAW Company C	E-beam/Wire Company D	Laser/Powder Company F	LENS/Powder Company G
Charpy V-notch	19.2	20.6	40.6	8.6	14.2	18.8
Unnotched	50.2	34.2	44.4	13	39.8	39.6

Figure 77. Average impact energy for both Charpy v-notch and unnotched specimens from each deposition process.

The v-notch samples for the two laser hot-wire and the LENS® deposition all had impact toughness in the range of 25.5-28.0 Joules (18.8-20.6 ft-lbs), roughly comparable to that of wrought Maraging 250 (Lang, 1971). The unnotched samples of the Company B laser hot-wire deposit and the LENS® deposit were also fairly consistent, at 46.4 J (34.2 ft-lbs) and 40.1 J (29.6 ft-lbs), respectively, while the samples from Company A were outstanding at 68 J (50.2 ft-lbs).

Two of the deposits had lower impact toughness: the electron-beam deposit from Company D (CVN 11.7 J (8.6 ft-lbs); unnotched 17.6 J (13.0 ft-lbs)) and the laser/powder from Company F (CVN 19.3 J (14.2 ft-lbs); unnotched 54.0 J (39.8 ft-lbs)). The porosity

seen in the x-ray of the electron-beam deposition had a deleterious effect on the deposit's v-notched and unnotched impact toughness. The laser/powder deposit from Company F, however, had a lower CVN toughness, but fairly typical unnotched toughness compared to the other processes.

The most outstanding CVN impact toughness samples were from the GMAW/Wire process from Company C. The CVN impact energy was 40.6 ft-lbs, compared to the next highest of 20.6 from Company B. The unnotched samples from the same block were also good, but were typical of the other processes as well. It was unexpected to see such good toughness from a block with as much porosity as this block showed in the x-ray, but the x-ray specimen was taken from the center of the block and the CVN samples were cut towards the end; it is possible that porosity was most prevalent in the center of the block and by taking the toughness specimen further to one side we had less included porosity in the samples.

In general, the toughness that should be expected from an additively manufactured maraging 250 structure is typically near 27 J (20 ft-lbs) for a full-size CVN specimen, and 54 J (40 ft-lbs) for an unnotched, sub-size specimen.

5.3. Conclusions

Based on the depositions conducted in this study, there are many acceptable deposition processes for additive tool repair and repurposing.

For evaluating the deposit for structural integrity, it appears that the biggest factor is macroscopic voids and/or inclusions. The x –ray images showed that many of the

deposition processes had some amount of indications present, ranging from small, scattered voids in laser to large widespread voids in electron beam. There are many existing non-destructive test methods for evaluation of welds in service, such as ultrasonic and x-ray testing, which may or may not be applicable to die repair overlays, depending on the scale and geometry of the die. However, since the surface of the deposit will be machined away to the final geometry, it would be recommended to use this process as an opportunity to inspect each surface for porosity during and after machining.

The CMM conducted on blocks post-deposition showed very little distortion in the base material, even on an annealed H13 base plate. This is promising, since distortion in these experiments could have indicated the presence of residual stresses in the deposit which could increase the likelihood of cracking, especially during the thermal cycling of die casting.

From the mechanical testing, it appears that additively manufacturing maraging structures have sufficient hardness, toughness, and strength for use in die cast tooling repair and repurposing. The hardness of the deposit generally matched the hardness of tempered H13, which is the workhorse of the industry currently, while having higher strength, provided by the martensitic microstructure of maraging steels. These properties have been used conventionally as indicators of good resistance to die failure mechanisms such as heat checking and erosion. The as-deposited maraging steel properties appear to result from self-temper resulting from subsequent passes on top of the tested region of the block. In practice, this result indicates that it would be a best practice to deposit enough

additional layers above the final surface to temper the region of the deposit that is level with the die surface in order to get this tempered martensite structure. Similar practice is already used in welding when hardness of the weld is critical; in these cases, a temper pass is often made by welding additional passes on top of a filled joint, which are then machined away to expose the tempered final surface.

Figure 78 shows a spider chart with relative strengths of each deposition process in this study for five categories: deposit density, elongation, yield strength, tensile strength, and Charpy v-notched toughness (farther out is better). The GMAW deposit had confounding results, with good strength and toughness but had poor elongation and a large number of x-ray indications. The electron-beam deposit had good strength and elongation, but had the most porous deposit, worst notched and unnotched impact toughness, and also softened the base H13 to 30 HRC as a result of heat dispersion through the base plate during deposition due to the vacuum chamber. The most consistent are the laser hot wire, DMD, and LENS® processes.

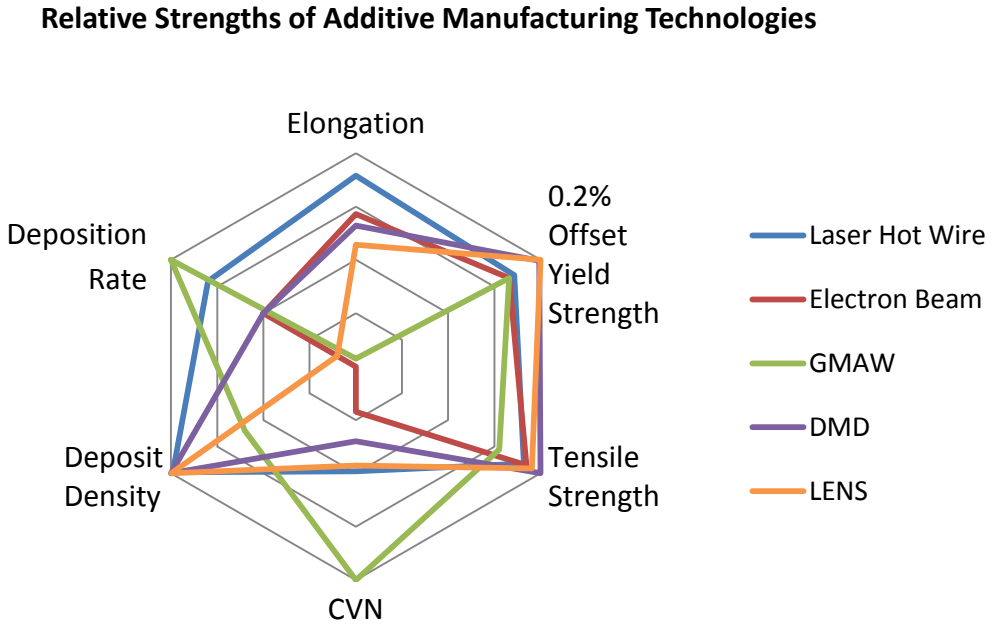

Figure 78. Spider chart showing the relative strengths for each additive manufacturing process based on the results of this study.

Chapter 6: Future Work

The present work provides a proof-of-concept for the use of additive manufacturing processes for the repair and repurposing of die casting tooling; however, the benefits of additive manufacturing for die casting may also be realized by other traditional manufacturing industries, such as forging. Much like the early days of welding, extensive, industry-wide research is needed to determine the limits of each process' operating ranges as well as the development and adoption of specifications for testing. The continuation of this research will hopefully lead to the development of these specifications.

Testing procedures for cladding and overlay applications have also never gained as much traction as other welding processes, largely due to the inability to reliably test and compare results on the dimensional scale of overlays. Testing procedures to better characterize microscale toughness and strength in single-passes from additive manufacturing (similar to cladding) would be a good step towards understanding of process variables on a finer scale that bulk deposits.

Concurrent to the present work on mechanical and microstructural properties, there is ongoing work on developing models for additive manufacturing to predict the distortion and microstructure, with the goal of reducing the cost and time associated with process development. Additionally, production die casting tooling was repaired using a number of processes and their life in service is been recorded. So far the dies have performed

well, and in some cases have lasted longer between repairs than their pre-repair service life. While these results are promising for the use of maraging in the repair of tooling, additional materials should be investigated to provide a wider range of options that can be tailored to individual applications. Development of wires for additive manufacturing to optimize their consistency and deposit cleanliness, similar to the powders and polymers developed for their respective additive manufacturing processes which have greatly increased market availability over recent years.

References

1. M. P. Groover, *Fundamentals of modern manufacturing: materials, processes, and systems* (5th ed.), 2013, Hoboken, NJ: John Wiley & Sons, Inc.

2. Pace Industries. "Die Casting 101." Accessed on August 7, 2014. http://www.paceind.com/die-casting-101/about_alloys

3. NADCA Product Specification Standard for Die Castings, NADCA Publication No. 402, 2012.

4. Y. Zhu, D. Schwam, J.F. Wallace, S. Birceanu, "Evaluation of soldering, washout, and thermal fatigue resistance of advanced metal materials for aluminum die-casting dies," Materials Science and Engineering A 379 (2004) Pp 420-431.

5. G. Roberts, G. Krauss, R. Kennedy, *Tool Steels* (5^{th} ed), 1998, Materials Park, OH: ASM International.

6. Z.W. Chen, M.Z. Jahedi, "Die erosion and its effect on soldering formation in high pressure die casting of aluminium alloys." Materials and Design. 20 (1999) Pp 303–309.

7. S. Gopal, A. Lakare, R. Shivpuri, "Die Casting: Aluminum. Alloy and Die Steel Interactions." Die Casting Engineer, May/June 2000, Pp 70–81.

8. D. Mellouli, N. Haddar, A. Köster, H.F. Ayedi, "Hardness effect on thermal fatigue damage of hot-work tool steel," Engineering and Failure Analysis 45 (2014), Pp 85-95

9. D. Klobčar, J. Tušek, B. Taljat, "Thermal fatigue of materials for die-casting tooling," Materials Science and Engineering A. 472 (2008) Pp 198-207.

10. S. Gulizia, M.Z. Jahedi, E.D. Doyle, "Performance evaluation of PVD coatings for high pressure die casting." Surface Coating Technologies. 140 (2001) Pp 200–205.

11. B. Gehricke, "Development, properties and characteristics of a new maraging 200 steel for die casting dies," Proceeding of the conference on the die casting technology in harmony with the environment, Cleveland, USA, 1993, pp.209-217.

12. V. Sutter, R.J. Dybas, *ASM Handbook*, Vol 6, "Welding, Brazing, and Soldering," 1993, Pp 1103-1107

13. M. Stanford, K. Kibble, M. Lindop, D. Mynors, and C. Durnall, "An investigation into fully melting a maraging steel using direct metal laser sintering (DMLS)," Steel Research Inst. 79, Special Edition Metal Forming Conference, Vol. 2, (2008) Pp 847-852.

14. M. Hall, C. J. Slunder, "The Metallurgy, Behavior, and Application of the 18-Percent Nickel Maraging Steels," NASA Technology Utilization Survey, 1968.

15. R. F. Decker, J. T. Eash, and A. J. Goldman, "Eighteen Percent Nickel Maraging Steel," Trans. ASM, 55 (1962) Pp 58-76.

16. E. P. Sadowski, "12% Ni Maraging Steel," Metals Eng. Quart, 5, (1965) Pp 56-64

17. S. Floreen, and R. F. Decker, "Heat Treatment of 18% Nickel Maraging Steel," Trans ASM, 55, (1962) Pp 518-530.

18. F. H. Lang, N. Kenyon, "Welding of Maraging Steels," WRC Bulletin 159. (1971)

19. J. Baker, and P. R. Swann, "The Hardening Mechanism in Maraging Steels," Trans ASM, 57, (1964) Pp 1008-1011.

20. J. Nadzam. *GMAW Welding Guide*. Lincoln Electric. March 1995.

21. P.K. Ghosh, L. Dorn, S. Kulkarni, F. Hofmann, "Arc characteristics of behavior of metal transfer in pusled current GMA welding of stainless steel," Journal of Materials Processing Technology 209, 2009, Pp 1262-1274.

22. D. Ding, Z. Pan, D. Cuiuri, H. Li, "A multi-bead overlapping model for robotic wire and arc additive manufacturing," Robotics and Computer-Integrated Manufacturing 31, 2015, Pp 101-110.

23. Y. Cao, S. Zhu, X. Liang, W. Wang, "Overlapping model of beads and curve fitting of bead section for rapid manufacturing by robotic MAG welding process," Robotics and Computer-Integrated Manufacturing 27, 2011, Pp 641-645.

24. J. Norrish, D. Cuiuri, "The controlled short circuit GMAW process: A tutorial," Journal of Manufacturing Processes 16, 2014, Pp 86-92.

25. P.M. Sequeira Almeida, S. Williams, "Innovative Process Model of Ti-6Al-4V Additive Layer Manufacturing Using Cold Metal Transfer," 21st International Solid Freeform Fabrication Symposium, Austin, TX, August 9-11, 2010.

26. B. Steen "Arc Augmented Laser Processing of Materials" *Journal of Applied Physics*, 1981

27. T.P Diebold, and C.E. Albright, "Laser-GTA Welding of Aluminum Alloy 5052,"*Welding Journal*, Volume 63(6), 1984.

28. R.P. Walduck, and J. Biffin, "Plasma arc augmented laser welding." *Welding Research Aboard*, 1995.

29. P. Denney, "Hybrid-laser arc welding – has its time finally arrived?" 2011, The Lincoln Electric Company, Cleveland, OH.

30. S. H. Mok, H.M. Sui, J. Folkes, I. Pashby, "Deposition of Ti-6-Al-4V using a high power diode laser and wire, Part I: Investigation on the process characteristics." *Surface & Coating Technology* 202 (2008) pp 3933-3939.

31. W.U.H. Syed, L. Li, "Effects of wire feeding direction and location in multiple layer diode laser direct metal deposition." *Applied Surface Science* 248 (2005). Pp 518-524.

32. F. Wang, J. Mei, H. Jiang, X. Wu, "Laser Fabrication of Ti6Al4V/TiC composites using simultaneous powder and wire feed." *Materials Science and Engineering A* 445-446 (2007) Pp 461-466

33. S. Peters, P. Denney, M. Latessa, M. Radke, "Power Supplies for Hot Wire Cladding," LIA Laser Additive Manufacturing 2012 Workshop. March 1, 2012.

34. D.M. Keicher, et. al. "Free Form Fabrication Using the Laser Engineered Net Shaping (LENS™) Process," 1996 World Congress on Powder Metallurgy and Particulate Materials, Washington, DC, 16-21 Jun, 1996.

35. J. Mazumder, et. al. "The Direct Metal Deposition of H13 Tool Steel for 3-D Components," JOM, Volume 49(5), May 1997.

36. Optomec "LENS® ™ 850-R Datasheet" Accessed August 4, 2014. http://www.optomec.com/wp-content/uploads/2014/04/LENS® _850-R_datasheet.pdf

37. DM3D. Accessed August 10, 2014. http://www.dm3dtech.com/index.php?option=com_content&view=article&id=182&Itemid=455

38. ASTM F2792-12a, "Standard Terminology for Additive Manufacturing Technologies," ASTM International, West Conshohocken, PA, 2012.

39. M.L. Griffith, et. al., "Understanding thermal behavior in the LENS process," Materials and Design, Volume 20 (2-3), 1999, Pp 107-113.

40. B Vamsi Krish, A. Bandyopadhyay, “Surface modification of AISI 410 stainless steel using laser engineered net shaping (LENS™),” Materials and Design, Volume 30 (5), May 2009, Pp 1490-1496.

41. X. Lin, H. Yang, J. Chen, W. Huang, “Microstructure evolution of 316L stainless steel during laser rapid forming,” Acta Metallurgica Sinica, Volume 42 (4), April 2006, Pp 361-368.

42. P. Ganesh, et. al., “Studies on pitting corrosion and sensitization in laser rapid manufactured specimens of type 316L stainless steel,” Materials and Design, Volume 39, 2012, Pp 509-521.

43. M. Alimardani, V. Fallah, M. Iravani-Tabrizipour, A. Khajepour, “Surface finish in laser solid freeform fabrication of an AISI 303L stainless steel thin wall,” Journal of Materials Processing Technology, Volume 212 (1), January 2012, Pp 113-119.

44. S. Bhattacharya, et. al., “Microstructural evolution and mechanical, and corrosion property evaluation of Cu-30Ni alloy formed by Direct Metal Deposition process,” Journal of Alloys and Compounds, Volume 509 (22), June 2011, Pp 6364-6373

45. K. Mahmood, A.J. Pinkerton, “Direct laser deposition with different types of 316L steel particle: a comparative study of final part properties.” Proceedings of the Institution of Mechanical Engineers, Part B: Journal of Engineering Manufacture, April 2013, Volume 227 (4), Pp 520-531.

46. V.R. Dave, J.E. Matz, T.W. Eager, “Electron Beam Solid Freeform Fabrication of Metal Parts,” Proceedings of 6th SFF Symposium, 1995, Pp 64-71.

47. K.M.B. Taminger, R.A. Hafley, “Characterization of 2219 Aluminum Produced by Electron Beam Freeform Fabrication,” Proceedings of 13th SFF Symposium, 2002, Pp 482-489.

48. C.A. Brice, et. al., “Rapid Prototyping and Freeform Fabrication via Electron Beam Welding Deposition,” Proceeding of Welding Conference, 2002.

49. H. Schultz. *Electron beam welding*. Abington publishing, Cambridge, 1993.

50. J. Norrish. *Advanced welding process-Technology and process control*. Woodhead Publishing Limited, Abington, Cambridge, England, 2006.

51. R. Colaço , R. Vilar “Stabilization of retained austenite in laser Surface melted tool steels.” Materials Science and Engineering A, Volume 385 (2004) Pp 123–127.